Institut für Theoretische Physik

Fakultät Mathematik und Naturwissenschaften

Technische Universität Dresden

Physical Aspects of Min Oscillations in *Escherichia Coli*

Dissertation

zur Erlangung des akademischen Grades

Doktor der Naturwissenschaften

(Dr. rer. nat.)

vorgelegt von

Giovanni Meacci

Max-Planck-Institut für
Physik komplexer Systeme

Dresden, 2006

ai miei genitori Anna e Bruno

Abstract

The subject of this thesis is the generation of spatial temporal structures in living cells. Specifically, we studied the Min-system in the bacterium *Escherichia coli*. It consists of the MinC, the MinD, and the MinE proteins, which play an important role in the correct selection of the cell division site. The Min-proteins oscillate between the two cell poles and thereby prevent division at these locations. In this way, *E. coli* divides at the center, producing two daughter cells of equal size, providing them with the complete genetic patrimony.

Our goal is to perform a quantitative study, both theoretical and experimental, in order to reveal the mechanism underlying the Min-oscillations.

Experimentally, we characterize the Min-system, measuring the temporal period of the oscillations as a function of the cell length, the time-averaged protein distributions, and the *in vivo* Min-protein mobility by means of different fluorescence microscopy techniques.

Theoretically, we discuss a deterministic description based on the exchange of Min-proteins between the cytoplasm and the cytoplasmic membrane and on the aggregation current induced by the interaction between membrane-bound proteins. Oscillatory solutions appear via a dynamic instability of the homogenous protein distributions. Moreover, we perform stochastic simulations based on a microscopic description, whereby the probability for each event is calculated according to the corresponding probability in the master equation. Starting from this microscopic description, we derive Langevin equations for the fluctuating protein densities which correspond to the deterministic equations in the limit of vanishing noise. Stochastic simulations justify this deterministic model, showing that oscillations are resistant to the perturbations induced by the stochastic reactions and diffusion. Predictions and assumptions of our theoretical model are compatible with our experimental findings.

Altogether, these results enable us to propose further experiments in order to quantitatively compare the different models proposed so far and to test our model with even higher precision. They also point to the necessity of performing such an analysis through single cell measurements.

Acknowledgments

My gratitude goes first of all to Karsten Kruse for the complete freedom that allowed me to follow my interests, points of view, and changes in points of view, keeping at the same time, with his comments, insights and precise criticisms my work in the "right" direction. He joined his passion and enthusiasm for the study of living systems with his generosity for a special kind of living beings called "students" and with the serenity he conveys to those who work with him.

To Markus Bär who trusted a student at first almost unable to speak English or German, giving him the opportunity to come to the MPIPKS, and for the many valuable discussions and suggestions.

I would like to take advantage of this occasion to thank my master degree thesis advisor Antonio Politi for the instructive and stimulating discussions we had in Florence and during his stays in Dresden and for theaching me what a simulation is all about.

I thank Hughes Chatè for his strong encouragement which has almost convinced me that what I am doing is something not as useless as I thought and for his expert advice about science and Italian and French wines.

Frank Jülicher for the pleasant atmosphere and highly formative environment of the biological department at PKS, perfect for graduate studies, and together with Professor Petra Schwille and Dr. Martin Howard who accepted to be a part of the thesis committee.

I am also grateful to Joe Howard and Petra Schwille for their hospitality and for the pleasant work atmosphere I found in their respective Labs, and all of the people there for their kindness.

Alessandro Torcini, for letting me know about the possibility of doing my PhD at the MPIPKS and for his advice concerning German food and language.

Elisabeth Fischer for her important contribution to the analysis of the experimental data and for the many stimulating questions and valuable discussions and suggestions.

...; das tägliche Streben entspringt keinem Vorsatz oder Programm, sondern einem unmittelbaren Befürfnis[1].

Albert Einstein

[1]"...; daily research, doesn't arise from a project or a program, but from an immediate demand". *Motive des Forschens*, Ansprache gehalten am 26 April 1918, in der *Deutschen Physikalischen Gesellschaft* zu Max Plancks sechzigstem Geburstag [1]

iv

Contents

Chapter 1

Introduction

A famous remark by the biologist Françqis Jacob asserts: "the dream of every cell is to become two cells" [2][1]. Fulfilling that dream requires a long list of molecular building blocks, spatial regulatory mechanisms, and the energy necessary to carry out the cell division process. The subject of this thesis concerns one of the spatial regulatory mechanisms in the bacterium *Escherichia coli*.

Why does a cell need regulatory mechanisms for division? In most prokaryotic and eukaryotic species, cell division takes place through the formation of a cell wall (plant cells, yeast, and prokaryotic cells) or a contractile ring (animal cells), and the consequent creation of two daughter cells. After chromosome replication and segregation, correct placement of the division site is crucial for the transmission of genetic information from parental to progeny cells. To achieve this goal, both eukaryotic and prokaryotic cells have developed extremely reliable division site selection mechanisms[2].

Spatial and temporal oscillations of the Min-proteins[3] in *E. coli* provide one of these mechanisms that permit the bacterium to identify the proper location of the division site.

---

[1]Also quoted in [3] p. 20.

[2]For a review of spatial control of division-site placement in bacteria and eukaryotes see [4, 5]

[3]A remark about notations. A fully functional cell line, or strain, found in the wild is called a wild type (wt). If a mutant cell is found that is missing a particular function or showing a new characteristic, the gene carrying the mutation is named in relation to that function or characteristic. For example, a *min* gene is one encoding a protein required for correct placement of the division plane. A cell with such a defect (min^-) makes the division plane, but in about 50% of all divisions the cell wall grows close to one of the two poles giving rise to mini-cells. From here the prefix "min". Usually the first gene of this type to be identified is called *minA* (in italics), the second is called *minB*, and so on throughout the alphabet. When the protein encoded by the gene is identified, it is called MinA (capitalized and in Roman type).
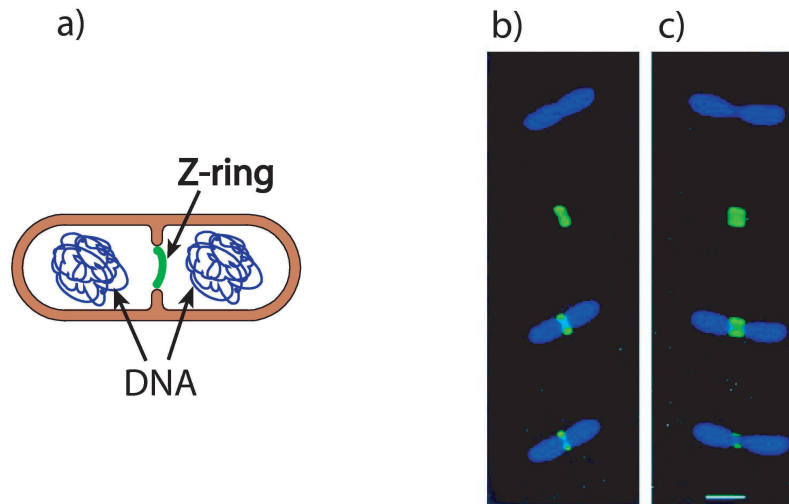
Figure 1.1: a) Schematic representation of *E. coli* during the division process. The division plane is determined by the location of the Z-ring, a structure built from FtsZ-filaments. A mechanism called "nucleoid occlusion" restricts the formation of the Z-ring to a region void of DNA. After duplication and segregation of the chromosome, three possible locations of ring formation remain: at the cell center and close to the two cell poles. The Min-system selects the center so that each daughter cell receives the complete genetic patrimony. b) and c) FtsZ-GFP (GFP stands for Green Fluorescence Protein, see chapter one) localizes to inter-nucleoid regions. Individual cells of JM109/pZG stained with 4,6-diamidino-2-phenylindole (DAPI; blue fluorescence), viewed for DAPI fluorescence only (top part), GFP fluorescence only (second part from top), and DAPI + GFP (lower two parts, composite images, with lowest part darkened to improve the visualization of the inter-nucleoid space). Bar $= 1\mu m$. b) and c) Taken from [6].

Like all prokaryotic cells, *E. coli* has no nucleus and, due to the spatial distribution of the chromosomes for the daughter cells to either side of the cell, precise spatially symmetric division is essential (see figure 1.1). In this study, we investigate possible mechanisms underlying the Min-oscillations by means of experiments, mathematical modeling, and numerical simulations.

Over the last fifteen years, the discovery of cytoskeletal[4] proteins in prokaryotic cells changed the old view of bacteria as simple containers of enzymes [9–11]. The absence of

---

[4]The cytoskeleton is a subcellular structure in the cytoplasm built from protein filaments. It gives the cell its shape, the capacity for direct movement, organizes the intracellular transport, and plays an important role during cell division [7,8]. Its components are actin filaments, microtubules, and intermediate filaments (IFs).

a cytoskeletal structure was once believed to be a decisive distinction between prokaryotes and eukaryotes. However, work in the past years has shown that bacteria actually possess a full complement of cytoskeletal proteins including actin, tubulin, and intermediate filament protein homologoues [9–19].

Elements of the division machinery in *E. coli* have been identified as a part of the bacterial cytoskeleton. FtsZ, the first protein to assemble at the future division site [20], is supposed to share a common ancestor with tubulin, the component of microtubules in eukaryotic cells. The two proteins have a modest homology of their sequences but a very similar three-dimensional structure [21]. MinD belongs to a large and functionally diverse family of ATPases proteins that have a conserved deviant Walker A motif and dimerize in an ATP-dependent manner [22–24]. These proteins have recently been suggested to be part of a new family of cytoskeletal proteins which are required for the spatial regulation of chromosome partitioning and cell division [25] and have no known direct counterpart in the cytoplasm of eukaryotes. In addition, proteins of the MreB family, present in a wide range of rod-shaped bacteria, including *E. coli*, are actin homologoues regulating the cell shape [26]. Finally, crescentin (CreS), an IF protein that localizes to *Caulobacter*'s inner curvature and regulates the cell shape, resembles IFs in animal cells [17].

Bacteria are simpler than eukaryotic cells and can in some cases be studied more easily. Their study can offer the opportunity to discover basic cellular mechanisms common to eukaryotic and prokaryotic cells, which have been preserved during evolution [9]. For instance, the Min-system was also found to determine the division site in plant cell chloroplasts [27], which are believed to have originated from photosynthetic bacteria. Homologoues of MinD, MinE and FtsZ proteins were identified in the nuclear genome of *Arabidopsis*. In particular, the importance of the MinD *Arabidopsis* homologue (AtMinD1) in plastid division was corroborated by the phenotype obtained when the AtMinD1 expression was altered [28]. Overexpression of AtMinD1 inhibits the chloroplast division as overexpression of MinD inhibits the growth of the Z-ring in *E. coli*. In addition, the reduction of AtMinD1 concentration gives rise to heterogeneity in chloroplast size, that is reminiscent of mini-cells formation in *E. coli*. This suggests a functional conservation between the *Arabidopsis* AtMinD1 and the *E. coli* MinD.

Moreover, proteins homologous to *E. coli* Min-proteins are present in many other bacteria [4], with cases of the conservation of the function between species. An example is shown by the ability of MinD (MinDNg) and MinE (MinENg) proteins from *Neisseria gonorrhoeae* to function as the usual Min-proteins when they are introduced into *E. coli*. MinD (MinDNg) and MinE (MinENg) also cause a division block when overexpressed in *Neisseria gonorrhoeae*, but it is not yet known whether the proteins oscillate within the cell. In *B. subtilis*, MinCD proteins prevent septation near the poles as they do in *E. coli*,

but remain in position at both poles without showing oscillations.

The study of bacteria is also important in its own right; in fact, bacteria are practically everywhere, and understanding how they work is useful in different fields from clinical treatment of infectious diseases to the production of energy.

Besides its biological relevance, the Min-system is an extraordinary example of how quantitative modeling may lead to new insight into the mechanism of self-organization in cells [29]. Because of the low number of Min-proteins, it is also an appropriate system to study stochastic effects in spatially extended systems. It is surprising that, despite the fluctuations in the number of involved molecules, most cellular events are precisely regulated, as is, in our case, the positioning of the division plane.

Other proteins not related to the cell division process show spatial-temporal patterns in bacteria. Examples are Par-B waves [30], and pole to pole oscillation of FrzS, a protein required for direct motility in *Myxoccocus xanthus* [31]. In general, oscillations occur in many biological conditions [32–36]. Spatiotemporal patterns appear spontaneously in a wide range of physical, chemical, and biological systems when they are driven sufficiently far from thermodynamic equilibrium. From a theoretical point of view they can be described in terms of a dynamic instability, a property of the system by which a spatially uniform state loses stability and passes into a non-uniform state, for example as a consequence of local fluctuations [37]. The first description of pattern formation in biological systems using this approach was introduced by Turing in 1952 [38].

In a broader context, our work may be seen as a paradigm of the physical approach to living systems. Traditionally, physics and biology developed different approaches for the study of inanimate and living systems. Galileo's study of motion is a prototypical example of the physics approach. He found mechanics neglecting friction, although friction is a crucial ingredient of everyday life. As a consequence, when a theoretical physicist tries to understand how a system like an *E. coli* cell works, he looks for universal laws, and his model should contain the minimum in possible ingredients, hopefully the key ingredients of the system. This means that, at the very least, the model must make predictions that can be experimentally tested. On the other hand, a biologist of the past century sought to understand the real *E. coli*, not a hypothetical one. His approach was much more descriptive. Understanding the system means to describe the system in all possible details[5], which makes quantitative predictions difficult.

---

[5]This is an oversimplification of the real situation. In fact, the desire to study biological problems using tools from other sciences has alway been present, and different approaches in the last century were used by biologists, such as the *holistic* one, where biological systems are described in their wholeness, or the *reductionistic* one, where the system is characterized in all single components. Interested readers are invited to consult the book of B.O. Kupper [39], or the historical account of E. Mayr [40]

In the last twenty years, the situation has drastically changed. Technological advances, for example in fluorescence microscopy techniques or microscopic manipulation of single molecules as DNA [41], have revolutionized our views of biological systems. This new situation opened the door to developing biology as a quantitative, predictive science. Theoretical physicists were attracted to this possibility and started to apply methods from the statistical physics of systems out of the thermodynamic equilibrium and non-linear dynamics to study biological systems. For a long time, only results for small deviations from the equilibrium were available in statistical physics [42]. Perhaps it is not by chance that new theoretical results have recently appeared in this field, in particular concerning fluctuation theorems and dynamical phase transition far from the equilibrium, just when technological advances allow for a comparison with experiments in living systems [43, 44]. Moreover, people from different fields and with different backgrounds as biologists, chemists, engineers, mathematicians, and physicists organized meetings and began to collaborate, looking for a new common approach to living systems. Due to the complexity of biological systems, finding general principles is a difficult task. Nevertheless, using the words of Uri Alon[6], we believe that biological system contain an inherent simplicity: "Although cells evolved to function and did not evolve to be comprehensible, simplifying principles make biological design understandable to us" [45].

We hope that by bringing the physics approach to biology new unexpected results and applications in biotechnology and medicine can be found. As Eric Siggia writes on his Lab Web Page "Nowadays, physics applied to cell biology is less reductionist than biochemistry. The challenge for the theorist is to deduce novel and quantitative conclusions from less than full chemical detail. The opportunities for doing so are when physics contributes to the experimental design rather than being added at the end to fit curves". This is the approach we followed in this thesis. In particular, we focus on the following issues: theoretical study of the Min-protein dynamics, by i) deterministic, and ii) stochastic descriptions; iii) experimental characterization of the Min-system and test of the predictions of our theoretical model by means of different fluorescence microscopy techniques.

The road map of this thesis is as follows[7]: The first chapter is devoted to experimental results. First the typical characteristics of the Min oscillations, observed by means of video-rate fluorescence microscopy, will be shown. Then, the measure of the values of Min-protein mobility, obtained by means of Fluorescence Correlation Spectroscopy (FCS). In the second chapter, a deterministic theoretical model is introduced, and predic-

---

[6]"Simplicity in Biology", course at the summer school on: "Physics of cellular objects", Cargèse 2006.
[7]For didactic reasons the order in which the different topics will be introduced does not follow the chronological order in which the work was carried out.

tions of the model are compared with the experimental findings of the first chapter. In the
third chapter, stochastic effects on the Min-system will be studied. Finally, the results and
possible future perspectives will be discussed.

Chapter 2

Experimental characterization of the Min-system

"With four parameters I can fit an elephant, and with five I can make him wiggle his trunk"

John von Neumann (as cited by Enrico Fermi)

Introduction

The Min-system has been characterized by intensive biochemical and genetic studies. In this introduction, the principal results of these studies will be reported, and the goal and the motivations of our experimental work, the results of which will be presented in the rest of the chapter, will be given.

Biochemistry and genetics of the Min-system. *E. coli* is a rod-shaped bacterium that lives in our intestine[1]. It is $2 - 6\mu$m length and $1 - 1.5\mu$m in diameter. The cell, which weighs only 1 picogram, is about 70% water. Some strains are flagellated and motile; others are non-flagellated and non-motile. The chromosome of *E. coli* consists of a single double-stranded chain of DNA about 700 times longer than the body of the cell. There are 4,639,221 base pairs specifying 4,288 genes, most of which encode proteins. The functions of only approximately 60% of these proteins are known. Their total number in each cell is on average $\sim 4 \times 10^6$. When *E. coli* grows, it first becomes longer and then divides in the middle. In a sense it is immortal[2] because the mother cell

---

[1] The following general information about *E. coli* are taken from "Motility Behavior of Bacteria" by Howard Berg in http://www.physicstoday.org/pt/jan00/berg.htlm.

[2] This statement may be too strong, see [46] about aging and death in *E. coli*

is replaced by two daughters essentially identical to the mother. The molecules of DNA in the members of a given set of descendants are identical except for mutations which occur spontaneously for a given gene at the rate of about 10^{-7} per generation.

When it is grown in a rich medium (such as salts plus a mixture of amino acids), and held at the temperature of the human intestine ($37\ ^\circ C$), *E. coli* can synthesize and replicate everything it needs to make a new copy of itself in about 20 minutes. The division plane is determined by the location of the Z-ring [47, 48]. This structure is built from FtsZ-filaments and forms on the inner bacterial membrane. The Z-ring recruits additional proteins, leading to the formation of a division machinery capable of carrying out cell division. In wt cells, the Z-ring assembles at mid-cell and is in residence for at least half the cell cycle before there is a visible invagination. During septation, the Z-ring contracts at the leading edge of the invagination. Using Fluorescence Recovery After Photobleaching[3] (FRAP) with FtsZ-GFP it was demonstrated that the Z-ring is a highly dynamic structure that undergoes remodeling [49], and more recently it was shown that its half-life is approximately $9s$ [50]. Finally, it was demonstrated by Fluorescence Resonance Energy Transfer (FRET) that protofilaments turn over with the same dynamics in vitro [51]. In turn, the position of the Z-ring is first of all determined by the distribution of the nuclear material inside the cell. A mechanism termed "nucleoid occlusion" restricts the formation of the ring to regions void of DNA [52–54]. So far this mechanism is poorly understood. After duplication and segregation of the chromosome[4], three possible locations of ring formation remain: at the cell center and close to the two cell poles. The selection of the center as the correct division site is achieved by the Min-system [57, 58]. The deletion of any of the Min proteins results in division septa forming close to one of the two cell poles in approximately 50% of all divisions. In these cases, DNA-free mini-cells are formed [59], which led to the name Min-system.

The Min-system consists of three proteins, MinC, MinD, and MinE, whose molecular weights are $25kD$, $30kD$, and $10kD$, respectively. Out of these, MinC induces the depolymerization of FtsZ-filaments and thus inhibits the formation of the Z-ring [60]. The distribution of MinC on the membrane changes periodically with time in such a way that in one half of the cycle, MinC accumulates at one pole while it accumulates at the opposite pole in the second half of the cycle [61, 62]. Formation of the Z-ring is thereby suppressed at the cell poles.

The oscillations of MinC require the presence of both, MinD and MinE, which themselves also oscillate [63, 64]. In fact, MinC binds to MinD and follows its dynamics [65].

---

[3]See appendix B for a short introduction to this technique

[4]Also the mechanism underlying chromosome segregation in bacteria is still elusive. Recent studies suggest that is a spontaneous process directly related to the cell length [55, 56].
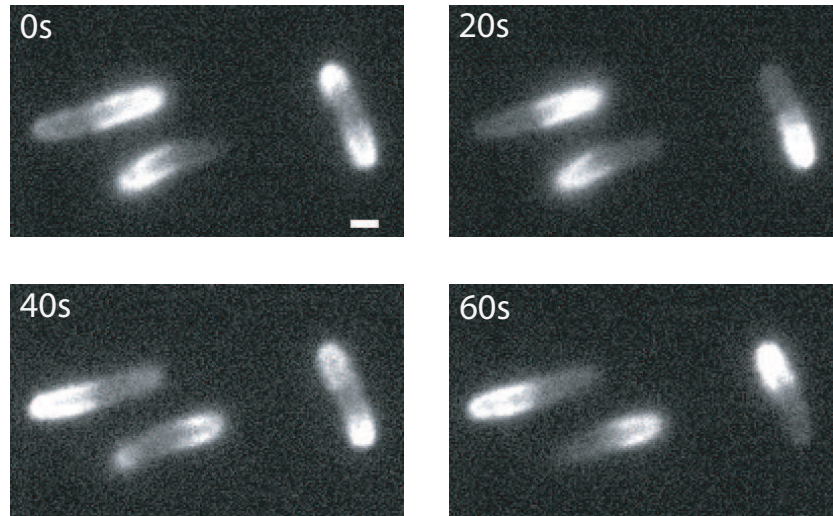
Figure 2.1: Oscillations of GFP-MinD in *E. coli*. Fluorescence images of GFP-MinD in three cell at subsequent time points separated by $20s$. Scale bar: 1μm.

Figure 2.1 shows an example of GFP-MinD protein oscillations. Remarkably, MinC is not necessary to generate oscillations, as MinD and MinE oscillate also in the absence of MinC [63]. *In vitro* experiments have shown that the ATPase MinD has a high affinity for the inner bacterial membrane when bound to ATP [66]. For concentrations of MinD exceeding a critical value, filamentous MinD aggregates are formed on phospholipid vesicles [66, 67]. The formation of MinD aggregates on vesicles leads to the formation of membrane tubes of a diameter of 50-100nm [66]. Around these tubes, MinD is wound in form of a helix with a pitch of about $6nm$, the linear extension of the MinD molecule. As for MinE, it associates with the membrane only in the presence of MinD. There it stimulates hydrolysis of the ATP bound to MinD, which eventually drives the protein off the membrane [66].

These *in vitro* results are compatible with the behavior of MinD and MinE *in vivo*. In MinD depleted cells, it was observed that MinE is dispersed in the cytosol, while MinD is homogeneously distributed on the cytoplasmic membrane if MinE is absent [63]. *In vivo*, the helices formed by MinD on the cytoplasmic membrane have a pitch of a few hundred nm [68]. The significance of the helical structures for the oscillation mechanism is still not understood. During the relocation of MinD from one cell half to the other, not all of the MinD seem to switch. We can speculate that the ones remaining might be used to reassemble the new helix in the next cycle. As MinE is recruited to the membrane by MinD, its arrangement follows the helical MinD pattern. Finally, the oscillatory behavior does not depend on the synthesis and degradation of the Min-proteins [63]. A schematic representation of the MinD/MinE oscillations is presented in figure 2.2.
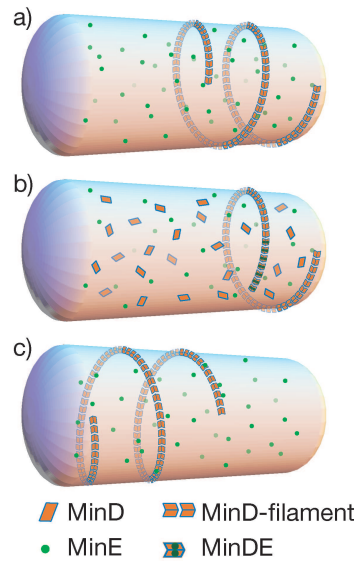
Figure 2.2: Schematic representation of MinD/MinE oscillations in *E. coli*. Three successive time instances are illustrated. MinD forms a membrane-bound helix in one half of the cell; MinE is associated with this structure, predominantly towards the center. (a) MinE stimulated detachment of MinDE from the membrane, setting free the cell center for division. (b) MinD and MinE diffuse in the cytosol, and, driven by the dynamical instability, MinD/MinE form a helix at the opposite end of the cell, (c) and the process repeats. Taken from [29].

Goal and motivation of our experimental work. Theoretical studies have provided strong evidence that the pole-to-pole oscillations are formed by the self-organization of MinD and MinE [29]. All mechanisms proposed so far rely essentially in one way or another on the formation of aggregates of membrane-bound MinD. Such aggregates were observed in vitro and in vivo [66, 68]. We will analyze in detail these mechanisms in chapter two. They can roughly be divided into two classes. In cooperative attachment models (CAM), MinD-aggregates are formed through collective effects during binding to the cytoplasmic membrane [69–75]. In aggregation current models (ACM), aggregates are formed after the proteins have bound to the membrane [76, 77]. In figure 2.3 a schematic representation of the two mechanisms is shown. CAM as well as ACM can capture the qualitative features of the Min-oscillations, and there is experimental evidence for both processes in *E. coli*. A study of MinD attachment to phospholipid vesicles in the presence of ATPγS, a non-hydrolyzable ATP analogue, suggests a two-step mechanism for the formation of aggregates of membrane-bound MinD first involving the binding of MinD to the membrane and subsequent aggregation [66]. In yeast two-hybrid assays MinD-MinD interactions were observed to be stronger if both proteins were
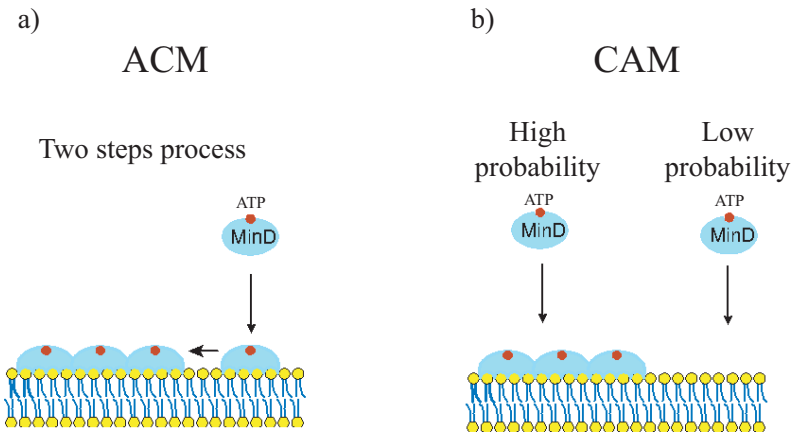
Figure 2.3: Schematic representation of (a) aggregation current model (ACM) and (b) cooperative attachment model (CAM).

membrane-bound than if at least one partner was cytosolic [78]. On the other hand, the concentration-dependence of MinD binding to phospholipid membranes deviates from Langumir isotherm [79, 80]. Furthermore, the amount of MinD binding to liposomes as a function of the MinD-concentration in the surrounding could be fitted by a Hill equation with a Hill coefficient of 2 [80].

In order to reveal whether either cooperative attachment or aggregation currents are dominant in *E. coli*, a quantitative comparison of the models with experiments is necessary. This requires to examine assumptions and specific predictions of the theoretical models, and to determine the model parameters by measurements.

To this end, in the first part of this chapter, fluorescence video-rate microscopy and Laser scanning Confocal Microscopy (LSCM) will be used to measure the space and time dependence of the protein distribution, the time-averaged protein distributions, and the temporal period of the oscillations as a function of the cell length. These observations will be compared with theoretical predictions in the second chapter. In the second part of this chapter, the results of measurements of the Min protein mobilities in vivo using Fluorescence Correlation Spectroscopy (FCS) will be shown. We have analyzed the data assuming that either aggregation currents or cooperative attachment is dominant and, thus, obtained key parameters of the various models.
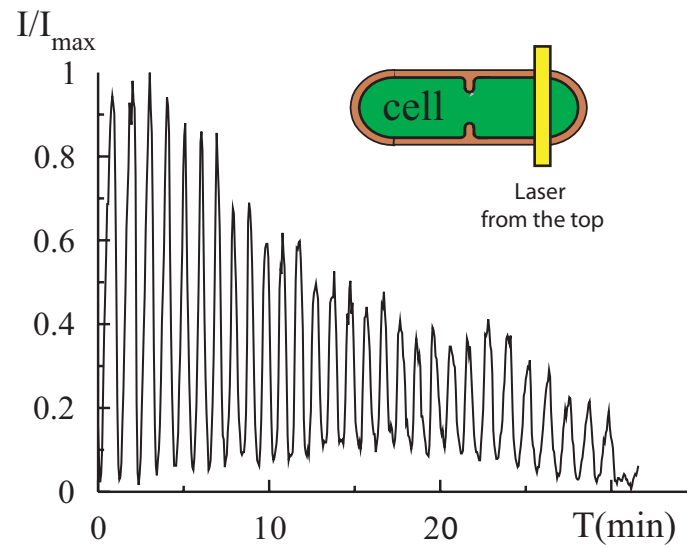
Figure 2.4: Fluorescence intensity I normalized by the maximum value I_{max} of GFP-MinD proteins in *E. coli* as a function of the time. The decay of the maxima values during the oscillation is due to photobleaching. A schematic representation of the cell is shown in the upper right side. The yellow area shows, form the top, the point from which the fluorescence intensity light was collected.
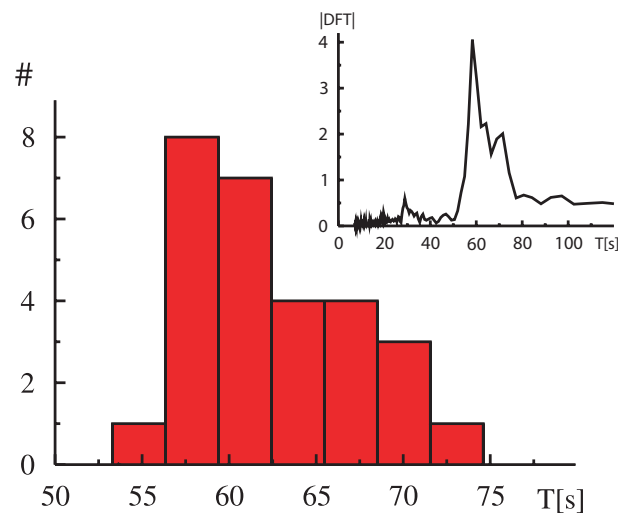
Figure 2.5: Histogram of oscillation period measured for GFP-MinD in a single *E. coli* cell from the fluorescence intensity signal in figure 2.4. The total time for the measurements was approximately half an hour. # is the number of periods measured. In the upper right side the discrete Fourier transform (DFT) of the fluorescence intensity signal in figure 2.4 is shown.

2.1 Min-oscillations

2.1.1 General aspects

To follow the temporal evolution of the Min protein concentration we used Min proteins tagged with GFP, a fluorescent protein cloned from the jellyfish *Aequorea victoria*. GFP has a β-barrel shape that contains an amino-acid triplet (Ser-Tyr-Gly) which undergoes a chemical rearrangement to form a fluorophore. When proteins fused to GFP are expressed in cells, they often retain the original protein function, and therefore can be used as a fluorescent tag to study protein localization. See appendix A for more information.

From a physical point of view, the two principal characteristics of the Min-oscillations are the temporal and spatial period. Concerning the temporal period, values of about one minute were found [61, 63]. These values agree with our measurements that range from $40s$ to $120s$, see figure 2.14. An example of a long record of GFP-MinD oscillations is shown in figure 2.4. Figure 2.5 shows the corresponding histogram of the period and its (discrete) Fourier transform (DFT). The peaks in the histogram and in the DFT are proof
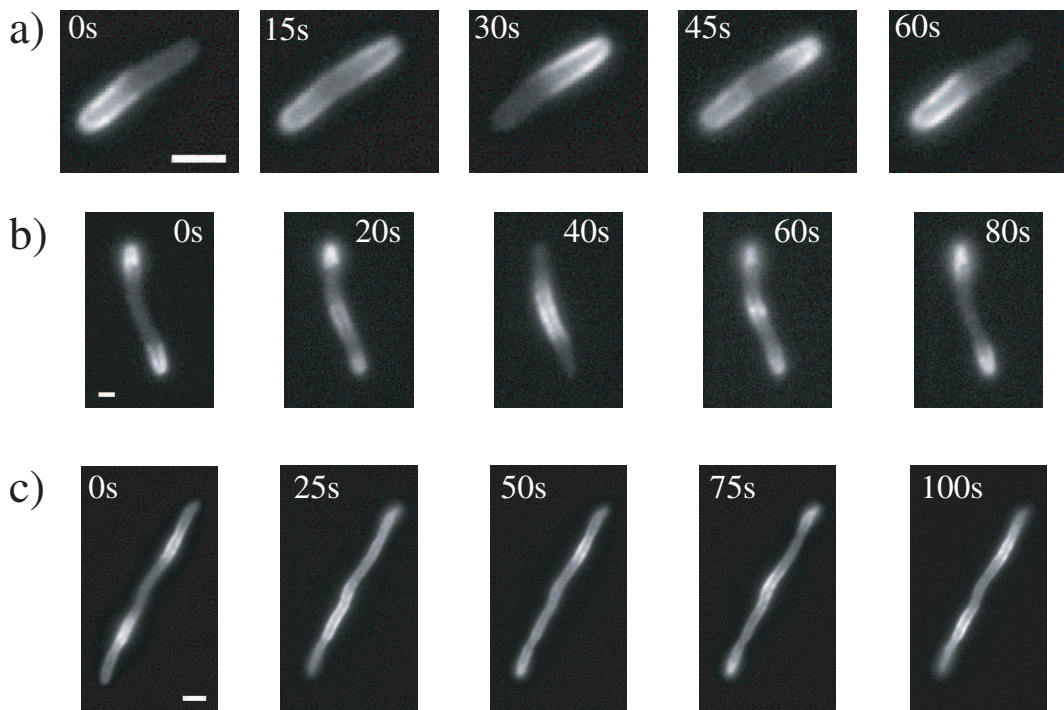
Figure 2.6: Sequences of fluorescence images of GFP-MinD in three different *E. coli* cells. Starting from the left, the images for each cell at subsequent time points are separated by (a) $15s$, (b) $20s$ (c) and $25s$, and show patterns with one, two and four stripes respectively. The cell lengths are approximately (a) 5μm, (b) 12μm, and (c) 20μm. Scale bar: 2μm.

that the spatio-temporal dynamics of the Min-proteins, really correspond to an oscillatory process. In bacteria of a length that exceeds a certain threshold, a striped oscillatory pattern appears, where the number of stripes increases with increasing cell length. This observation is indicative of an intrinsic spatial wave-length of the oscillations. Typical spatial wave-length values range from 1.5μm to 5μm. In figure 2.6, examples of three cells with one, two and four stripes respectively, are shown.

The spatial distribution of MinE is more complex than the one of MinD. The analysis of fluorescence images of MinE-GFP show clear accumulations of MinE as displayed in figure 2.7, termed MinE-rings [81]. It was shown, that the ring is not stationary, but oscillates [64]. More recently, using deconvolution techniques, MinE was found to be arranged in a helix with accumulation for the one stripe pattern case close to the cell center and, although weaker, at the cell poles [68]. It was suggested that the helical arrangement of MinE is induced by the helical arrangement of MinD and that the accumulation of MinE occurs at the ends of the MinD helix [68]. In cells mutant for MinE, oscillations were observed in the absence of a MinE-ring [82]. In that case, the temporal period is larger than in non-mutant cells. Still, this experiment clearly shows that the MinE-ring is not necessary for the oscillations.

We analyzed hundreds of videos, and the majority of them showed that MinD oscillatory pattern correspond to a standing wave, see figure 2.8. Nevertheless, in approximately ten cases we found traveling waves, i.e. protein translocation along the cell from the one side to the opposite side. Figure 2.9 shows an example of MinD travelling waves. Contrary to [74] we didn't observe switching between standing and traveling vawes.
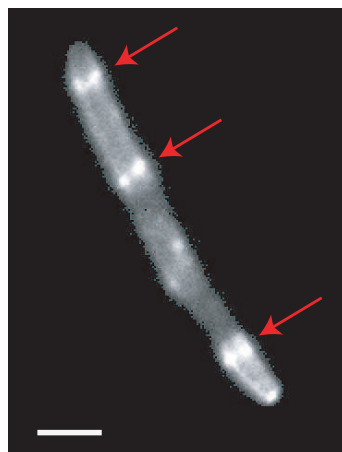
Figure 2.7: Fluorescence image of MinE-GFP. Three MinE rings (indicated by the arrows) are clearly visible. Other MinE structures are visible, they belong to a distorted rings at the end of the depolymerization process. Scale bar: 2μm.
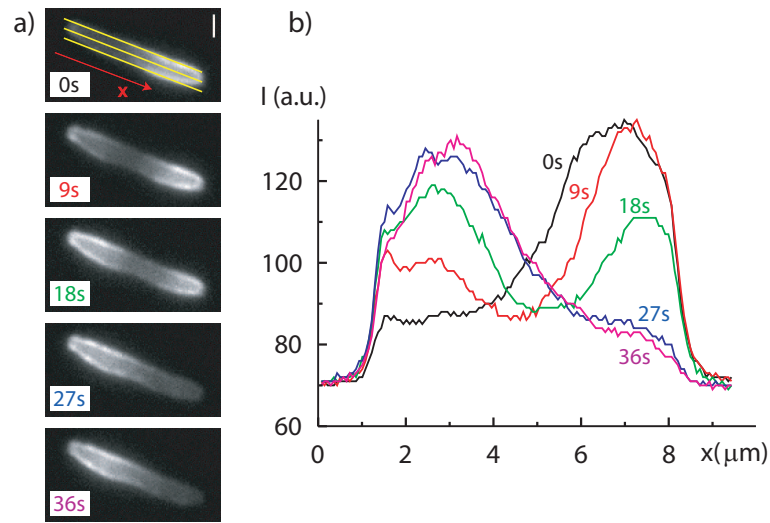
Figure 2.8: An example of a standing wave of GFP-MinD. a) Fluorescence images in a cell at subsequent time points separated by 9s. Scale bar: 1μm. The cell length is $\approx 6.6\mu$m. b) Fluorescence intensity I in arbitrary units obtained from a line scan of the fluorescence signals in a). Yellow lines in a) indicate the area considered for the line scan, and in each point of the x axis the intensity value was obtained by averaging the fluorescence signal in the transversal direction to these lines.
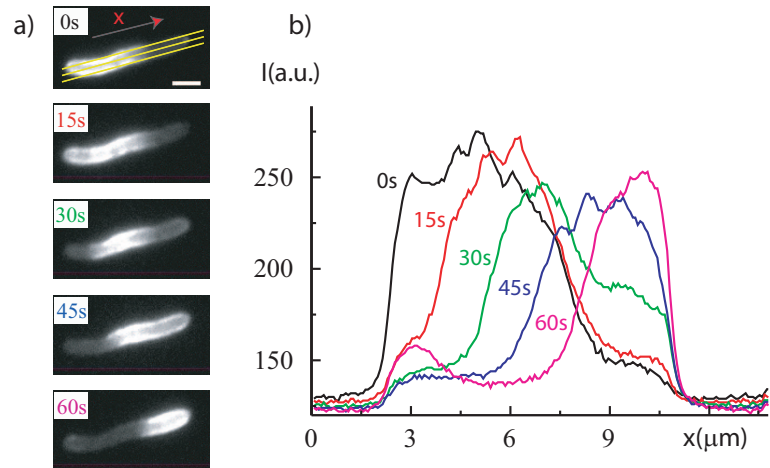
Figure 2.9: An example of a traveling wave of GFP-MinD. a) Fluorescence images in a cell at subsequent time points separated by 15s. Scale bar: 2μm. The cell length is $\approx 8.5\mu$m. b) Fluorescence intensity I in arbitrary units obtained from a line scan of the fluorescence signals in a). Yellow lines in a) indicate the area considered for the line scan, and in each point of the x axis the intensity value was obtained by averaging the fluorescence signal in the transversal direction to these lines.

2.1.2 Time-averaged distributions

Figure 2.10 shows the time-averaged MinD distribution. It has a pronounced minimum in the middle of the cell. This minimum suggests a possible mechanism for selecting the division site. The MinC proteins spend most of the time at the cell poles and therefore preclude the FtsZ ring from growing there, leaving the middle of the cell as the only possible division site. In figure 2.11 it is also shown how the minimum in the cell center is preserved during many oscillations. However, for other cells examined, the minimum of the time-averaged fluorescence intensity was much more shallow or even absent, see figure 2.12. On the one hand, this might reflect deviations in the total protein density in individual bacteria from the average total protein density in a bacterial colony. On the other hand, considering different cells of different lengths, we have found that, at least qualitatively, the value of the minimum decreases with the system length up to the point when the oscillation pattern acquires a new stripe, corresponding to a cell length of $\approx 2.5 - 3.5\mu$m, see, for instance, the red curve in figure 2.12. It would be interesting to verify this point in a single cell experiment. In longer cells the two maxima at the poles
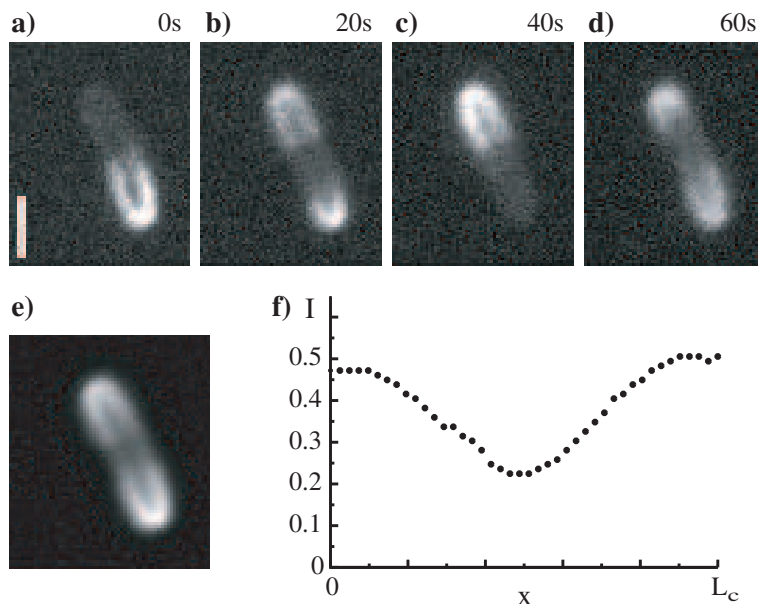
Figure 2.10: Oscillations of GFP-MinD in *E. coli*. a-d) Fluorescence images of GFP-MinD in a cell at subsequent time points separated by 20s. e) Time-average of all frames during one oscillation period. Two subsequent frames are separated by 1s. f) Fluorescence intensity I obtained from a line scan of the fluorescence signal in (e). The background signal was subtracted from the total signal which was then rescaled with the maximum intensity during the oscillation. The slight asymmetry is due to bleaching during the observation period. Scale bar: 1μm. The cell length is $L_c = 2.8\mu$m.
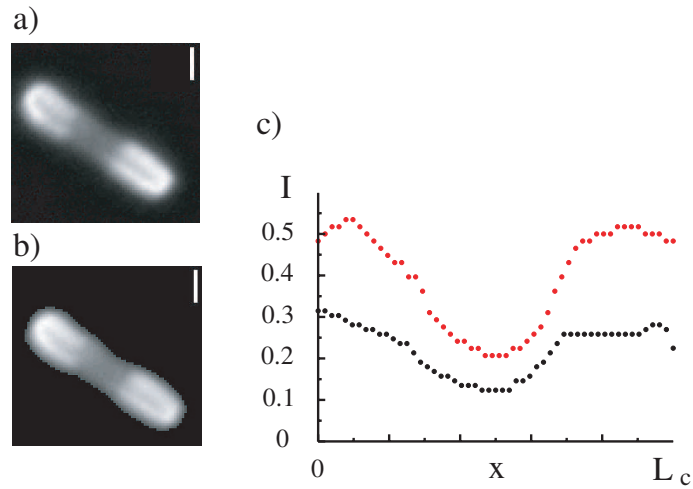
Figure 2.11: a) Time-average of all frames during one oscillation period. Two subsequent frames are separated by 2s. b) Time-average of all frames during ten oscillation period. c) Up (red) curve: time-average of all frames during one oscillation period obtained from a line scan of the fluorescence signal in (a). Down (black) curve: time-average of all frames during ten oscillation periods, obtained from a line scan of the fluorescence signal in (b). The background signal was subtracted from the total signal which was then rescaled with the maximum intensity during the oscillation. The slight asymmetry and likely also the decreasing of the intensity value at the poles are due to bleaching during the observation time. The cell length is $L_c = 5.2\mu$m.
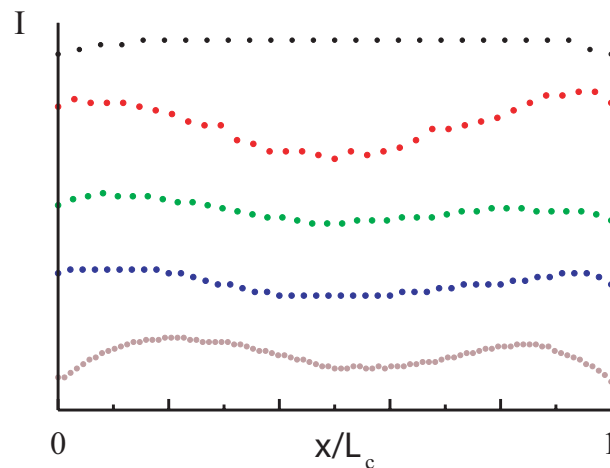
Figure 2.12: Time-average of all frames of fluorescence images GFP-MinD during one oscillation period for different cells. Starting from the top the cell length is 2.4μm, 2.6μm, 2.9μm, 3.4μm, 6.6μm, respectively for the black, red, green, blue, orange dots. In the vertical axis the fluorescence intensity is reported, with the same unity as in figure 2.10(f), but the curves are shifted, one with respect to the other, to avoid over-positions.
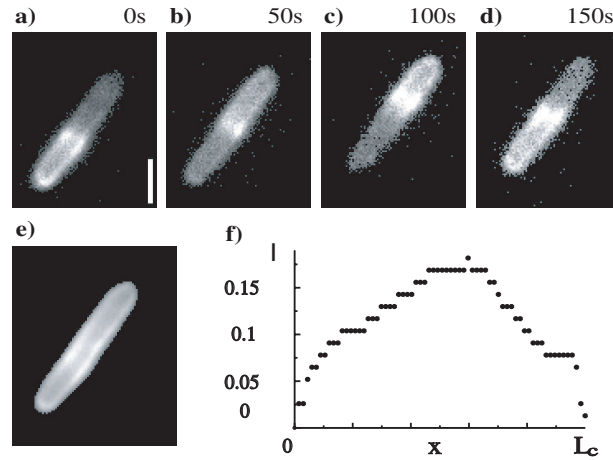
Figure 2.13: Oscillations of MinE-GFP in *E. coli*. a-d) Fluorescence images of MinE-GFP in a cell at subsequent time points separated by 50s. e) Time-average of all frames during one oscillation period. Two subsequent frames are separated by 2s. f) Fluorescence intensity I obtained from a line scan of the fluorescence signal in (e). The background signal was subtracted from the total signal which was then rescaled with the maximum intensity during the oscillation. The slight asymmetry is due to bleaching during the observation period. Scale bar: 2μm. The cell length is $L_c = 5\mu$m. The steps are due to the finite resolution of the fluorescence intensity detector.

move toward the middle. This might indicate a coupling between the cell length and the assembly of the Z-ring. Finally, in figure 2.13, the time-averaged MinE distribution is reported with a maximum in the center. This maximum reflects the presence of the MinE ring.

2.1.3   Oscillation period as a function of the cell length

We measured the temporal period of the oscillations in *E. coli* containing GFP-MinD as a function of the cell length, see figure 2.14. The periods fall in the range of 50s to 120s, even for bacteria of 15μm in length. Measurements were carried out with video-rate-microscopy. Because of photobleaching, this method allows for recording only a few periods in each single cell. Consequently, in figure 2.14, every point corresponds to a different cell. In order to minimize the error in the cell length, we considered only cells with their complete body in focus. The data indicate large variations in the oscillation period for cells of approximately the same length.

To investigate the origin of these variations, the oscillation in a single cell was recorded for approximately $30min$ with LSCM. In comparison to video-rates-microscopy, LSCM allows for measuring the oscillation period by collecting the fluorescent light from
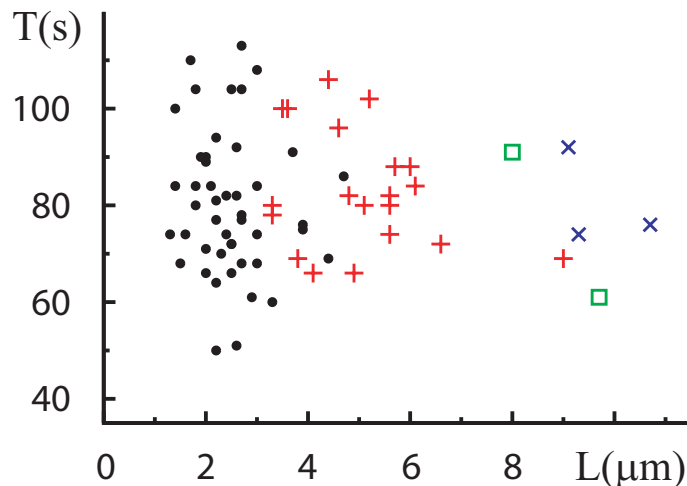
Figure 2.14: Oscillation period measured for GFP-MinD in *E. coli* as a function of the cell length. Black dots: oscillation pattern as in figure 2.6(top), red crosses: oscillation pattern as in figure 2.6(middle), green and blue dots: oscillation pattern with three and four stripes, respectively. Error bars are of about the size of the symbols.

a smaller volume of the cell. Together with the small power of the exciting laser this allows for significantly lower photobleaching. In this way, extensive recording of the oscillations of up to $45min$ is possible, see figure 2.4.

We considered the distribution for the values of the period for some cells, keeping the temperature constant at $22°C$. Under these conditions the cell grows very slowly. In figure 2.5, a typical histogram of the oscillation period is shown. The little asymmetry in the distribution and the secondary peak in the DFT may be an indication that the cell had grown a little, but here the important information is that the standard deviation (SD) of this distribution is smaller than the variation of the periods at approximately the same length in cell population, figure 2.14.

Therefore, fluctuations in the period of the single cell can only partially account for the spread in figure 2.14. The main contribution is likely to be due to different protein concentrations in different cells. In fact, experimental observations [63] indicate that the period increases with the MinD concentration and decreases with the MinE concentration; in addition we expect every cell to have a different protein concentration [83, 84].

We performed the same measurement at $37°C$, allowing for the growth by some μm in length within $30min$ as shown in figure 2.15(b). In figure 2.15(a) a measurement of the period as a function of time in a single cell at $37°C$ is shown. In order to reduce the effects of photobleaching, the measurement was stopped after $25min$ and restarted approximately $7min$ later, but at that point the signal was much noisier, and the error in the value for the oscillation period was higher. In addition, due to photobleaching, it
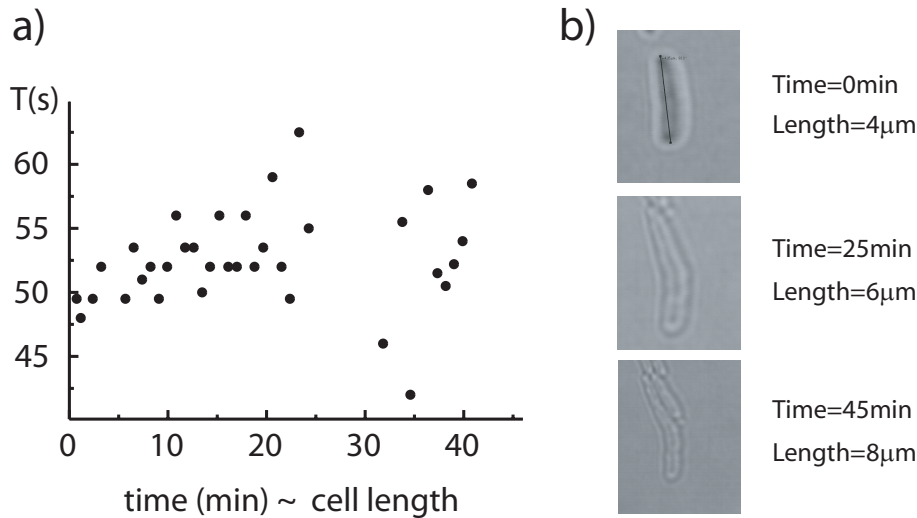
Figure 2.15: a) Oscillation period measured for GFP-MinD in a single *E. coli* cell. As error bars, not shown, we can consider the SD in figure 2.5 of approximately $10s$ in the first part up to $25s$ and a greater error in the second part. i) Bright field images of the same cell at different moments in time. Starting from the top the first image shows a dashed line corresponding to a cell length of 4μm.

was possible to check on the spatial pattern only at the beginning of the measurement and the cell length in the dark field at some moments in time. Therefore, we were not able to ascertain if the cell acquired a new stripe or not, and further measurements will be necessary.

2.2   Measurement of Min-protein mobility

The are several non invasive techniques based on fluorescence spectroscopy that can be used for measurements in living cells; for a general reviews see [85, 86]. Three of them were used for measurements of protein mobility in bacteria. Direct measurements of the displacement of individual proteins were employed to determine the mobility of membrane proteins in *Caulobacter crescentus* [87]. FRAP, where the fluorescent proteins present in a defined region are bleached and the recovery of the fluorescence is monitored, was used to measure the diffusion constants of cytoplasmic proteins [88]. The third method, FCS, exploits the fluctuations in the fluorescence intensity emanating from an illuminated region with respect to the mean signal in order to assess dynamic properties [89]. It was used to measure the dynamics of CheY involved in chemotaxis [90] and transcription activity at the RNA level [91, 92]. We have used FCS to measure the mobility of MinD and MinE tagged to GFP. As a control we also measured the mobility

Figure 2.16: The actual confocal FCS setup applied to Min proteins mobility measurements. See "Optical Setup" in appendix A for details.

of the Enhanced Green Fluorescent Protein (EGFP). The experimental setup is shown in figure 2.16. For a short introduction to FRAP and FCS see appendix B.

2.2.1 Quasi-steady states during oscillations

The analysis of fluorescence fluctuations requires a well-defined average state. Seemingly, this is not the case for the Min-system which oscillates with a period of approximatively $80s$. However, there are regions in the bacteria in which the fluorescence signal is quasi-stationary for approximatively 10s. In figure 2.17(b), we present the fluorescence intensity in a confocal volume positioned in one cell half. There are phases of high and low constant fluorescence as well as phases of strongly varying fluorescence. Respectively, these phases reflect the dwelling of MinD in one cell half for a large fraction of a half-period as well as the comparatively rapid transition to the opposite cell half. Figure 2.17 (c) displays the fluorescence intensity along the bacterial long axis for six different times separated by 2s. The intensity variations during this period are less then 5%. The fluorescence profiles in cross-sections perpendicular to the long axis also show only moderate fluctuations, figure 2.17(d) and (e). The form of the mean profiles in the low- and high-intensity regions differ significantly: while the profile in the low-intensity region is uni-modal, it is bi-modal in the high intensity region. This results from a low fraction of membrane-bound MinD in the low intensity region and a high fraction in the
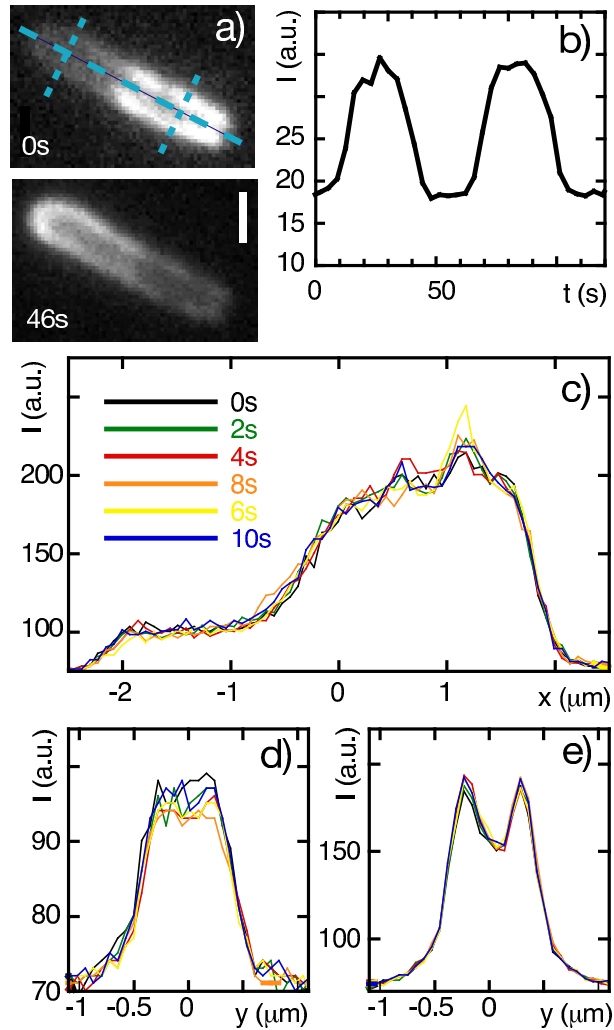
Figure 2.17: Quasi steady states. a) GFP-MinD fluorescence in *E. coli* at different phases of the oscillation cycle. Scale bar: 1μm. b) Fluorescence intensity in a confocal volume located in one cell-half as a function of time. Oscillations with a period of $60s$ are clearly seen. Around states of maximal and minimal intensity, time-intervals of roughly constant fluorescence intensity can be detected. c,d,e) Fluorescence intensity along the long axis (c) and the cross-sections (d, e) indicated in (a) for six different times separated by 2s each. The curves vary around a quasi-stationary mean profile. The differences in the cross-section profiles (d) and (e) reflect the different fractions of membrane-bound proteins in the low- and high-intensity phases in a cell half.

high-intensity region [63]. The fluorescence profiles for different times then indicate that the respective amounts of cytoplasmic and membrane-bound MinD are quasi-stationary within the 10s shown.

2.2.2 Diffusion constants and residence times

EGFP. We first measured the autocorrelation of the fluorescence fluctuations of EGFP in living *E. coli*, see appendix A "Materials and Methods". A typical autocorrelation curve is depicted in figure 2.18(a). From a fit of the correlation curve expected for a single diffusing species in two dimensions, equation (A.0.1) with $F = 1$, see appendix A, an apparent diffusion constant of $D_1 = 12.9 \pm 2.3\mu\mathrm{m}^2/s$ is obtained. There are two sources contributing to the error in the value of the diffusion constant. First, a systematic error results from uncertainties in determining the size of the detection volume. The size of the detection volume is needed for transforming the relaxation time that can be extracted from the correlation curve into a diffusion constant. The value of this error was estimated to be 15%. Secondly, the fit is of finite accuracy due to noise present in the experimental correlation curve (around 10%). For the curve in figure 2.18(a), the fit quality is reasonable with $\chi^2 = 1.6$. In view of the measurements on MinD and MinE, further models were used for analyzing the correlation curves. Fitting the data to the autocorrelation G_{diff} expected for two independent populations of diffusing particles, equation (A.0.1) where F is now a fit parameter, the fit quality was significantly improved, $\chi^2 = 1.1$. For the curve in figure 2.18(a), the apparent diffusion constant of the fast component is $D_1 = 17.7 \pm 3.6\mu\mathrm{m}^2/s$. Furthermore, we considered the case of the molecules switching between a mobile and an immobile state, G_{ex} equation (A.0.3) (appendix A). For the diffusion constant in the mobile state, we found $D = 14.8 \pm 2.8\mu\mathrm{m}^2/s$ with $\chi^2 = 1.1$. Previous reports suggest deviations from normal diffusion of EGFP in vivo or crowded in vitro environments [93–97]. The mean-square displacement of a diffusing particle in three dimensions in a continuous and isotropic medium is usually given by $\langle r^2(t)\rangle = 6Dt$. The derivation of this expression is based on the Fick's law, which is an established phenomenological law for diffusion in isotropic fluids. On the other hand, in a crowded and complex media as in the cytoplasm there is no physical reason why the Fick's law should apply and one might expect the mean-square displacement to obey a power law $\langle r^2(t)\rangle = 6\Gamma t^\alpha$, where the transport coefficient Γ, is a constant that does not depend on time. Microscopically the origin of the anomalous diffusion can be understood with the following simple argument. If $\langle r^2(t)\rangle >>$ or $<<$ of a characteristic (square) length scale ξ^2 corresponding to the obstacles or the different constituents of the medium where the protein diffuse, we are expecting normal diffusion, but when $\langle r^2(t)\rangle \approx \xi^2$, diffusion can
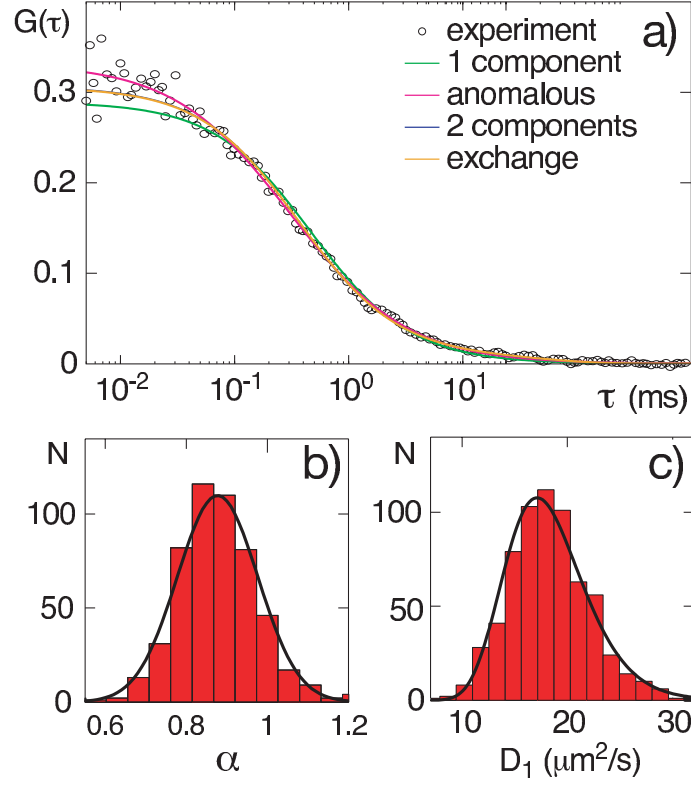
Figure 2.18: Diffusion coefficients of EGFP in *E. coli* measured by Fluorescence Correlation Spectroscopy. a) Typical autocorrelation $G(\tau)$ for EGFP (black circles) and non-linear least square fits of correlation curves expected for different processes. Green: diffusion, equation (A.0.1) with $F = 1$, gives $D = 12.9 \pm 2.3 \frac{\mu m^2}{s}$ with $\chi^2 = 1.6$. Pink: anomalous diffusion, equation (A.0.2), yields $\alpha = 0.83 \pm 0.01$ and $\Gamma = 4.7 \pm 0.75 \frac{\mu m^\alpha}{s}$ with $\chi^2 = 1.1$. Blue (the blue curve is hidden behind the yellow curve): two independent diffusing populations, equation (A.0.1), yields $D_1 = 17.7 \pm 3.6 \frac{\mu m^2}{s}$, $D_2 = 0.3 \pm 0.2 \frac{\mu m^2}{s}$, and $F = 0.96 \pm 0.01$ with $\chi^2 = 1.1$. Yellow: exchange between a diffusing and an immobile state, equation (A.0.3), yields $D = 14.8 \pm 2.8 \frac{\mu m^2}{s}$, $\tau_1 = 2.3 \pm 1.0$s, and $F = 0.97 \pm 0.004$ with $\chi^2 = 1.1$ No significant autofluorescence of cells was detected, but there was a non-correlated background of 8 kHz from the medium. b) Histogram of anomalous exponents obtained from 1021 measurements. Solid line: normal distribution with mean $\alpha = 0.88$ and variance $\sigma_\alpha^2 = 0.09$ c) Histogram of diffusion coefficients obtained from fitting G_{diff} to the same curves as in (b). Solid line: log-normal distribution with geometric mean $D = 17.9^{+4.3}_{-3.4} \frac{\mu m^2}{s}$. In (b) and (c) only fits with $\chi^2 < 1.2$ were considered.

be anomalous. We therefore considered anomalous diffusion of EGFP, where the mean square displacements grow as a power law in time with an exponent $\alpha < 1$. Whereas two-dimensional membrane diffusion has been clearly shown to be anomalous [98–100], in our knowledges in the cytoplasm anomalous protein diffusion has not been conclusively demonstrate. Fitting the correlation G_a we obtained an anomalous exponent of $\alpha = 0.83 \pm 0.01$ and an anomalous transport coefficient $\Gamma = 4.7 \pm 0.75 \mu m^2/s^\alpha$ with $\chi^2 = 1.1$ As can be seen in figure 2.18(a), the three different fits are barely distinguishable.

A histogram of the diffusion constant obtained by fitting G_{diff} to 1021 curves is presented in figure 2.18(c). The histogram is well described by a lognormal distribution[5] with a geometric mean of $D = 17.9^{+4.3}_{-3.4}\frac{\mu m^2}{s}$. Within the accuracy of our measurements, different cells give the same value for the EGFP diffusion constant. Figure 2.19 shows an example of diffusion constant values in single cell. The SD is of the some order as in measurements in different cells. An hand-selection of curves (see figure 2.20), as is often done in FCS measurements, reduced the 1σ-confidence interval but did not change the geometric mean, For the data shown in figure 2.20 we checked the individual correlation curve for unusually big spikes of intensity and/or inaccurate baselines, and we discharged it if necessary. The fraction of the fast component was $F = 0.96 \pm 0.03$ indicating that

---

[5] Whereas Gaussian distributions describe processes that are a sum of random variables with finite mean and variance, lognormal distributions characterize processes with several *multiplicative* stochastic steps [101].
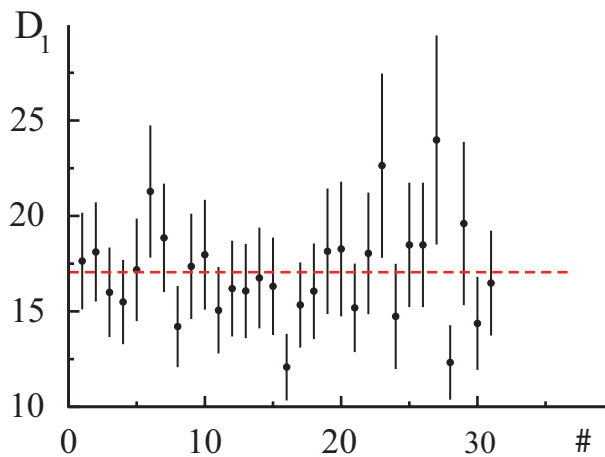
Figure 2.19: Diffusion coefficient of EGFP in a single cell. Each of the 31 points correspond to one single measurement in the same focal volume. The data were fitted with the autocorrelation curve G_{diff}. Error bars have been calculated from $\Delta D = D(2\Delta\omega/\omega + \Delta\tau/\tau)$. The red dashed line is the mean value corresponding to $D = 17.1\frac{\mu m^2}{s}$ with $SD = 2.7\mu m^2/s$.
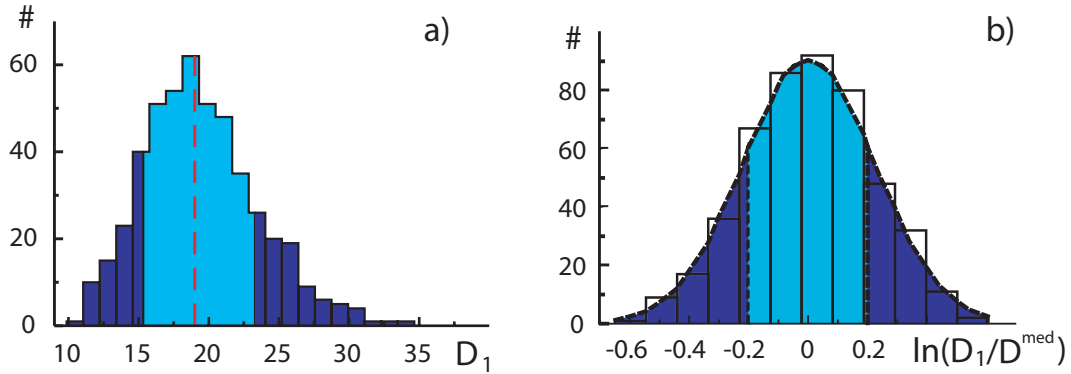
Figure 2.20: Hand-selected data for EGFP. Histogram of the fast diffusion coefficient assuming two diffusing species, for 482 correlation curves in 19 BL21(DE3)pLys cells, hand-selected between 1021 curves in 22 cells. Only fits with $\chi^2 < 1.2$ were considered. a) Original scale. b) Logarithmic scale. $D^{med} = 18.7^{+3.9}_{-3.1} \frac{\mu\text{m}^2}{s}$ is the median value and # is the number of correlation curves measured. Cyran areas, from the median to both sides, correspond to one SD. Dashed line: fit with normal distribution with mean $D_1 = 18.6 \mu\text{m}^2/s$, and variance $\sigma^2_D = 0.18$ in dimensionless unit. # is the number of hand-selected curves.

most of the dynamics results from diffusion. We arrived at the same conclusion using G_{ex} for the data analysis, see tables 2.1 and 2.2. Figure 2.18(b) presents a histogram of anomalous exponents from analyzing the same curves using G_{a}. The mean value is $\alpha = 0.88 \pm 0.1$

Adding a His-tag to EGFP were reported to strongly alter its dynamical properties [88] giving rise to a broad distribution of the diffusion values. We examined **His6-EGFP** expressed in the same strain as was used for the measurement of EGFP mobility. Using either G_{diff} or G_{ex}, we found a decrease in the diffusion constant of approximatively 20% and a slightly broader distribution compared to EGFP. Based on the anomalous diffusion model, we found a slightly reduced value for the anomalous mobility, $\Gamma = 5.6^{+5.7}_{-2.8} \frac{\mu\text{m}^2\,\alpha}{s}$, while the anomalous exponent remained the same, $\alpha = 0.88 \pm 0.1$ The six histidine residues inserted at the N terminus of the EGFP protein could alterate the interaction of the protein with the environment and explain in part the lowering of the diffusion constant value.

GFP-MinD. MinD-mobility was measured in the strain JS964. For the FCS analysis of the MinD-mobility, only fluorescence curves taken from regions in quasi-steady state were considered. Every individual measurement lasted 5s. A typical autocorrelation curve is shown in figure 2.21(a). From the graph it is obvious that two distinct time-scales are present. For the laser power used, the bleaching time for immobilized molecules
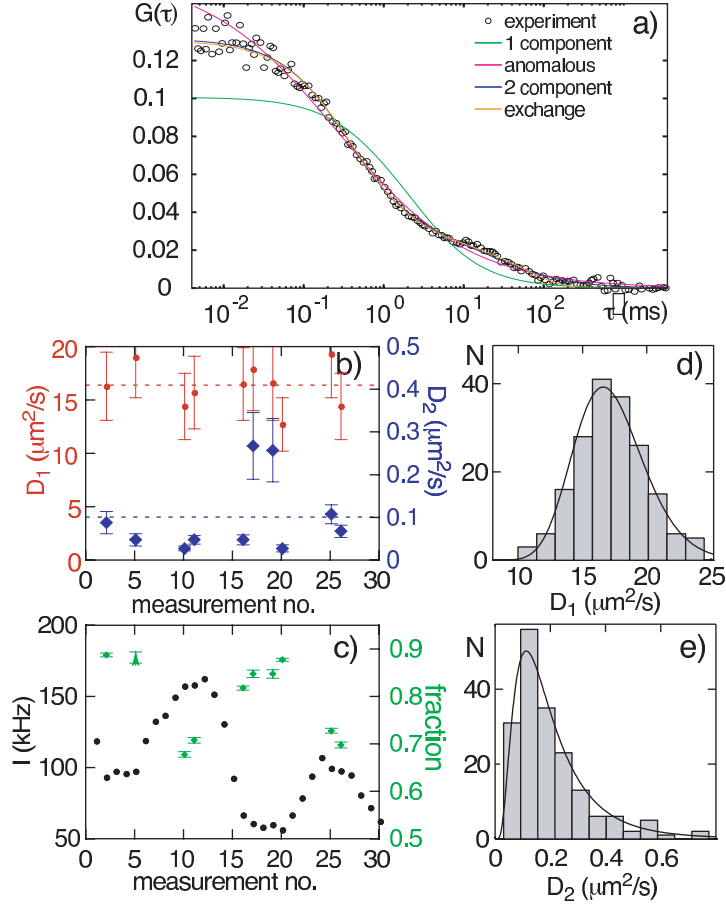
Figure 2.21: Correlation analysis of MinD mobility - two independent diffusing species. a) Typical autocorrelation curve for GFP-MinD in a region of quasi-steady state (black circles) and non-linear least square fits of different expected correlation curves. Green and pink: diffusion and anomalous diffusion, respectively. Essential features of the experimental curve are missed ($\chi^2 = 5.6$ and 1.8, respectively). Blue (the blue curve is partially hidden behind the yellow curve): two independent diffusing populations, equation (A.0.1), yields $D_1 = 19.8 \pm 4.3 \frac{\mu\mathrm{m}^2}{s}$, $D_2 = 0.11 \pm 0.02 \frac{\mu\mathrm{m}^2}{s}$, and $F = 0.74 \pm 0.01$ with $\chi^2 = 1.1$. Yellow: exchange between a diffusing and an immobile state, yields $D = 15.7 \pm 3.1 \frac{\mu\mathrm{m}^2}{s}$, $\tau_1 = 302 \pm 25$ms, and $F = 0.83 \pm 0.004$ with $\chi^2 = 1.18$ b) Apparent diffusion constants D_1 and D_2 for 10 curves admitting a good fit ($\chi^2 < 1.4$) among 30 subsequent measurements on a single cell. The mean values are $D_1 = 16.4 \pm 2 \frac{\mu\mathrm{m}^2}{s}$ (mean±SD) and $D_2 = 0.1 \pm 0.09 \frac{\mu\mathrm{m}^2}{s}$ (mean±SD). c) Fluorescence intensity and fast fraction for the same measurements as in (b). The fast fraction is higher for low intensities. d,e) Histograms of the diffusion constants. Only curves with quasi-steady fluorescence intensity and a fit quality of $\chi^2 < 1.5$ were retained. Solid lines: log-normal distributions with geometric means $D_1 = 17.0^{+3.0}_{-2.5} \frac{\mu\mathrm{m}^2}{s}$ and $D_2 = 0.17^{+0.14}_{-0.08} \frac{\mu\mathrm{m}^2}{s}$.

was on the order of seconds (data not shown). Furthermore, the correlation curves were largely independent of the excitation intensity (data not shown). We therefore concluded that the second time scale is not due to bleaching of immobilized molecules but due to further dynamical processes in addition to cytosolic diffusion. The existence of two MinD populations - on the one hand dissolved in the cytosol, on the other hand bound to the membrane - suggests two obvious candidate processes leading to the additional time-scale visible in the correlation curves. The second relaxation time may for one be due to the diffusion of MinD on the membrane. For the other it may result from the exchange of MinD between the membrane and the cytosol.

We analyzed the measured correlation curves using the two different models separately. Of course, the two processes are not mutually exclusive. It would thus be desirable to analyze the correlation curve using a model that accounts for diffusion and for binding and unbinding. However, the expected correlation curve differs only in small amounts from the curves for either of the two alternatives separately, and the accuracy of our measurements does not allow for distinguishing between them.

We will first present the results assuming two states of different mobility. Figure 2.21(b) displays the results for the two diffusion constants obtained from a fit of G_{diff}, equation (A.0.1), to different correlation curves measured for a single cell. We interpret the faster diffusion constant to represent the mobility of cytosolic MinD. It is of the same order as the diffusion constant of EGFP, see table 2.1. The smaller diffusion constant is interpreted as corresponding to membrane-bound MinD. This is supported by the estimated value of the fraction of the fast component: In agreement with the measurements of the cross-sections, figures 2.17(d) and (e), the fraction of fast moving proteins is larger in
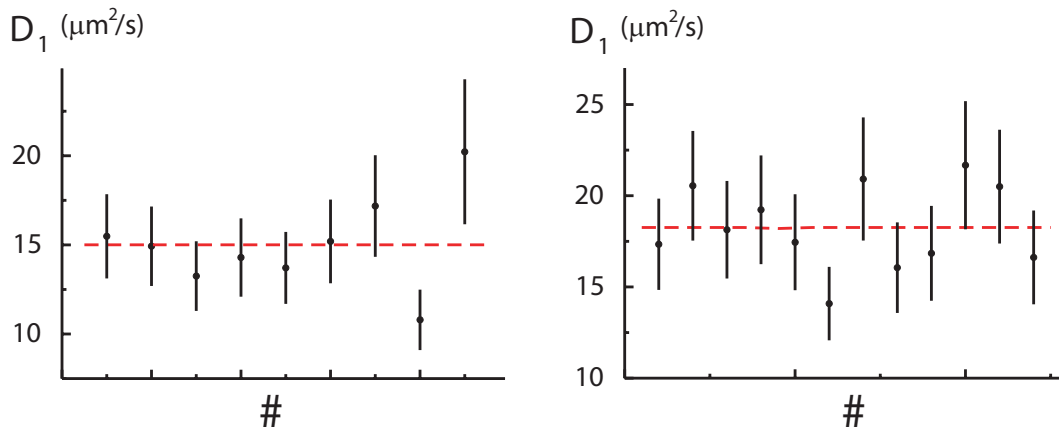
Figure 2.22: Apparent diffusion constants D_1 for a) 9, and b) 12 hand-selected curves admitting a good fit ($\chi^2 < 1.3$) among 30 subsequent measurements on a single cell. The mean values ($\pm SD$) are a) $D_1 = 15.0 \pm 0.65 \frac{\mu\text{m}^2}{s}$ and b) $D_1 = 18.2 \pm 0.5 \frac{\mu\text{m}^2}{s}$.

the low-intensity regions than in the high-intensity regions, see figure 2.17(c). The standard deviation of the mean is smaller than the estimated error of a single measurement, showing that the quality of our results is not limited by the variations within a cell. See also figure 2.22 for the fast diffusion constant from hand-selected measurements within one cell.

Histograms of fast and slow diffusion constants summarizing series of measurements on different cells are shown in figure 2.21(d) and (e). Both histograms are well described by a log-normal distribution. The geometric mean value for the fast diffusion constant is $D_1 = 17.0^{+3.0}_{-2.5} \frac{\mu m^2}{s}$. For the slow diffusion constant we found $D_2 = 0.17^{+0.14}_{-0.08} \frac{\mu m^2}{s}$. This value is one order of magnitude higher than the diffusion constant measured for the membrane-bound histidine kinase PleC measured by single protein tracking *C. crescentus* [87]. On the other hand, using FRAP, a similar value has been obtained in [102] for integral plasma membrane proteins (TatA) fused with GFP, $0.13 \pm 0.03 \mu m^2 s^{-1}$. The authors of this work measured also the diffusion constant for the TorA-GFP on the cytoplasm. They found a value of $9.0 \pm 2.1 \mu m^2 s^{-1}$. In this case because for the cytoplasmic TorA-GFP the bleaching time was of the same order of the fluorescence recovering time they bleach the cell with very high laser power level for only $0.5s$ and considered elongated *E. coli* cells in order to observe the recovery of the bleach coming from regions of the cell far from the bleached area. This value is similar to the one found in [88] using the same technique and both of them are different from the value we found. The difference
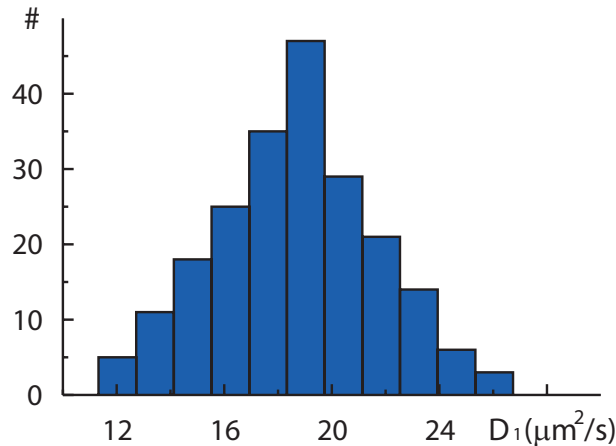
Figure 2.23: Histogram of the fast diffusion constant assuming two independent diffusing species, for 214 hand-selected correlation curves between 1207 curves in 38 JS964 cells. Only curves with quasi-steady fluorescence intensity and a fit quality of $\chi^2 < 1.3$ were retained. The mean value $(\pm SD)$ is $D_1 = 18.2 \pm 3.0 \frac{\mu m^2}{s}$. # is the number of hand-selected curves. Notice that here the original sample of curves is smaller in respect to the automatic selection based only on convergence of the fit algorithm and quality of the fit.

is on the order of the SD in our measurements, therefore we think is not significative. Nevertheless we notice that different cell strains was used in the different experiments, that FRAP and FCS use different approximations in the data analysis and that FCS is in principle a less invasive technique when compared with FRAP which usually need to send laser light a quite hight intensity level. Even between EGFP and MinD-GFP there is a factor of two in size is not surprising they turn out have a very similar diffusion constant. In fact a factor of two in size correspond to a factor of 0.85 in the diffusion constant, i.e. based only in size considerations we are expecting for EGFP a diffusion constant equal to 0.85 times the diffusion constant of GFP-MinD. This value is well inside one SD from the actual value we found. Figure 2.23 shows the histogram of the fast diffusion constant for hand-selected curves. No correlation could be detected between the values of the fast and slow diffusion constants (data not shown). Separating the curves into those of low and high average intensity does not reveal significant differences between the respective fast and slow diffusion constants, see table 2.1. The fraction $F = 0.81 \pm 0.1$ of the fast diffusing component, however, is larger in the low-intensity regions than in the high-intensity regions, where $F = 0.71 \pm 0.10$. The difference in the fractions is more pronounced when averaging over several measurements on a single cell than when averaging over measurements on different cells, figure 2.21(c). This presumably reflects different protein concentration in different cells.

The same data was analyzed based on the exchange of MinD between a mobile (cytosolic) state and an immobile (membrane-bound) state. As suggested by the cross-section profiles, figure 2.17(e) and (f), we assumed the average fraction of mobile molecules to be constant during one measurement. In that case, the residence times τ_1 and τ_2 of MinD in the mobile and immobile states, respectively, are related to the fraction F of mobile molecules by $F = \tau_1/(\tau_1 + \tau_2)$. The results obtained from analyzing the same curves as in figures 2.21(b) and (c) are displayed in figures 2.24(a) and (b). The diffusion constants are in the same range as the values of the fast diffusion constant obtained above. The same holds for the value of the mobile fraction. The histograms of the diffusion constant and the residence time in the mobile state are presented in figures 2.24(c) and (d). The differences in the values for low- and high-intensity regions are not significant, although the residence times seem to be larger in the low-intensity regions, see table 2.1.

We repeated the measurement using a different strain (WM1255). The average cytosolic diffusion constants are smaller in this strain, while the average residence time is somewhat larger, see tables 2.1 and 2.2. In view of the broadness of the distributions, however, the differences are not significant. Due to the small number of good curves, a separation between regions of low and high intensity was not performed.
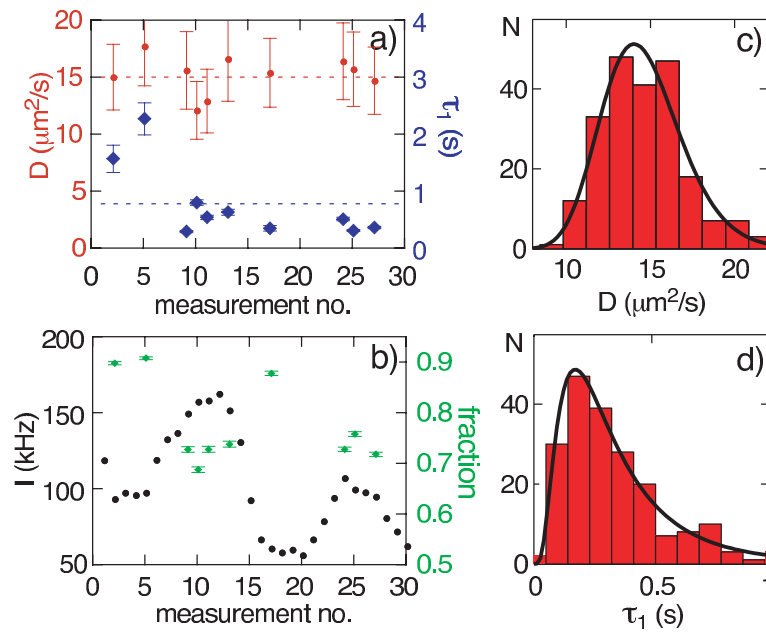
Figure 2.24: Correlation analysis of MinD mobility - exchange between diffusing and immobile state. a) Apparent diffusion constants and residence times in the mobile state for the same 30 subsequent measurements on a single cell as in figure 2.21b,c. The mean values are $D = 15.0 \pm 1.9 \frac{\mu m^2}{s}$ and $\tau_1 = 783 \pm 651$ms (mean±SD). b) Fluorescence intensity and mobile fraction for the same measurements as in (a). The mobile fraction is higher for low intensities. c,d) Histograms of the diffusion constants and residence times obtained from the same 2017 measurements as in figure 2.21(d) and (e). Solid lines: log-normal distributions with geometric means $\bar{D}_1 = 14.4^{+2.6}_{-2.2} \frac{\mu m^2}{s}$ and $\tau_1 = 322^{+422}_{-183} ms$.
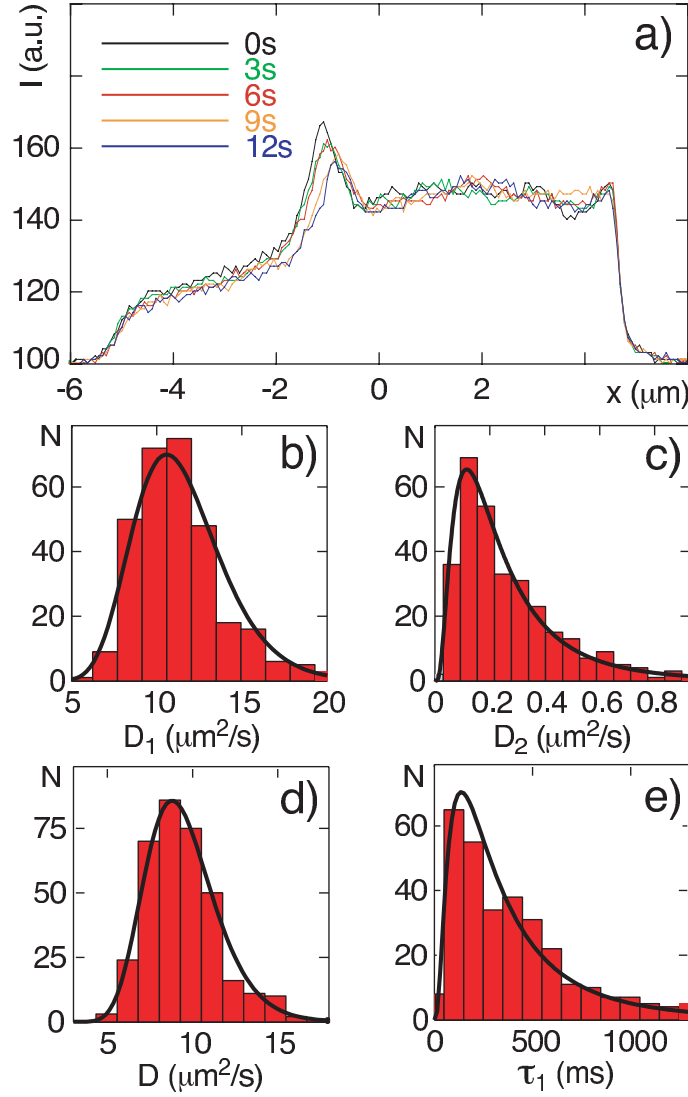
Figure 2.25: Correlation analysis of MinE. a) Quasi-steady state of the MinE distribution along a cell's long axis. Five curves separated each by 3s are varied around a mean profile. An accumulation of MinE close to the cell center, commonly know as MinE ring, can clearly be recognized. It moves slowly to one cell pole. The cell length is approximately $10\mu m$. b,c) lines: log-normal distributions with geometric means $D_1 = 11.2^{+2.9}_{-2.3}\frac{\mu m^2}{s}$ and $D_2 = 0.20^{+0.23}_{-0.11}\frac{\mu m^2}{s}$. d,e) Histograms of the diffusion constants and residence times obtained from the same measurements as in (b,c) assuming exchange between a diffusing and an immobile state. Solid lines: log-normal distributions with geometric means $D = 9.3^{+2.3}_{-1.9}\frac{\mu m^2}{s}$ and $\tau_1 = 396^{+888}_{-274}ms$.
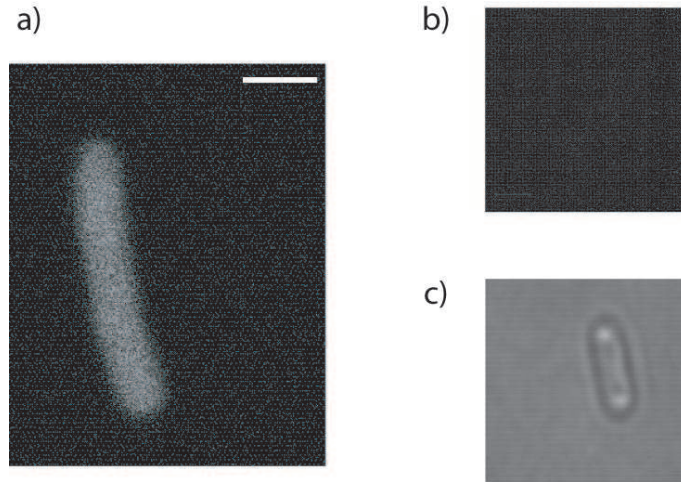
Figure 2.26: Fluorescence images of two strains of *E. coli*. a) Strain BL21 expressing His6-EGFP. b) Strain BL21 , wild-type *E. coli*. c) Strain BL21 , wild-type *E. coli* in dark field. Scale bar: $1\mu m$.

MinE-GFP. For measuring the mobility of MinE we employed the same strategy as for MinD. An example of a quasi-steady state of the MinE distribution is shown in figure 2.25(a). As for MinD, two distinct relaxation times can be detected in the correlation curves. These curves were analyzed using the same models as for MinD. The histograms of the two different diffusion constants and of the diffusion constant and the residence time in the mobile state, respectively, are presented in figure 2.25(b) and (e). As before, the histograms are well described by log-normal distributions. Assuming two independent populations with different mobilities, we find $D_1 = 11.2^{+2.9}_{-2.3}\frac{\mu m^2}{s}$ and $D_2 = 0.20^{+0.23}_{-0.11}\frac{\mu m^2}{s}$. The fraction of the faster diffusion population is $F = 0.79 \pm 0.10$. Assuming the other model, we obtain $D = 9.3^{+2.3}_{-1.9}\frac{\mu m^2}{s}$ and $\tau = 396^{+888}_{-274}$ms. The mobile fraction is in this case $F = 0.86 \pm 0.09$ Separating the curves into those from a low-intensity and those of a high-intensity phase, no significant differences between the values of the diffusion constants or the residence times in the different phases can be detected, see tables 2.1 and 2.2.

Controls. To ascertain that we observed only EGFP and not cellular autofluorescence we imaged *E. coli* strains BL21 expressing His6-EGFP, figure 2.26(a), BL21 wt figure 2.26(b) and JS964 figure 2.26(c) under identical circumstances. In figure 2.26(b), the low autofluorescence of *E. coli* is shown. Figure 2.26(a) shows the homogenous distribution of cytoplasmic EGFP. Similar checks, not shown, were carried out for the other strains.

	N_{tot}	N_{sel}	D_1 ($\frac{\mu\text{m}^2}{s}$)	D_2 ($\frac{\mu\text{m}^2}{s}$)	F	N
EGFP[a]	1021		$17.9^{+4.3}_{-3.4}$	$0.22^{0.51}_{0.16}$	$0.96^{+0.03}_{-0.03}$	652
His6-EGFP[b]	555		$14.9^{+3.7}_{-3.0}$	$0.14^{0.53}_{0.11}$	$0.96^{+0.04}_{-0.04}$	214
GFP-MinD[c]	2017	438	$17.0^{+3.0}_{-2.5}$	$0.17^{+0.14}_{-0.08}$	$0.77^{+0.11}_{-0.11}$	181
GFP-MinD[c] l.i.		191	$16.7^{+3.1}_{-2.6}$	$0.18^{+0.16}_{-0.08}$	$0.81^{+0.10}_{-0.10}$	105
GFP-MinD[c] h.i.		247	$17.4^{+2.6}_{-2.3}$	$0.15^{+0.11}_{-0.06}$	$0.71^{+0.10}_{-0.10}$	76
GFP-MinD[d]	738	102	$14.3^{+2.9}_{-2.4}$	$0.16^{+0.18}_{-0.08}$	$0.82^{+0.08}_{-0.08}$	50
MinE-GFP[e]	1807	528	$11.2^{+2.9}_{-2.3}$	$0.20^{+0.23}_{-0.11}$	$0.79^{+0.10}_{-0.10}$	307
MinE-GFP[e] l.i.		310	$11.4^{+2.8}_{-2.3}$	$0.21^{+0.25}_{-0.11}$	$0.82^{+0.09}_{-0.09}$	198
MinE-GFP[e] h.i.		218	$10.9^{+3.1}_{-2.4}$	$0.20^{+0.20}_{-0.10}$	$0.75^{+0.11}_{-0.11}$	109

Table 2.1: Mobility of EGFP, His6-EGFP, GFP-MinD, MinE-GFP - **two diffusion model**. For the Min proteins, curves from low-intensity phases (l.i.) and high-intensity (h.i.) phases were analyzed separately. N_{tot}: total number of correlation curves analyzed. D_1, D_2: diffusion constants for two independent populations, F: fraction of the faster/mobile population, N: number of curves allowing for a sufficiently good fit. Values were only considered from curves where the fit produced a $\chi^2 < 1.5$ (for EGFP $\chi^2 < 1.3$) and where the intensity was constant. Displayed are the mean values and the 1σ confidence interval. For EGFP, the values of D_1 are well described by a log-normal distribution, while the values of D_2 vary too strongly as that, or any other, a distribution could be identified. For the Min proteins, the values of D_1, D_2, are well described by a log-normal distribution. For all strains, the values of F follow a normal distribution. [a]BL21(DE3)pLys, [b]BL21(DE3)pLys, [c]JS964, [d]WM1255, [e]WM1079.

	N_{tot}	N_{sel}	$D\ (\frac{\mu\text{m}^2}{s})$	τ_1 (ms)	F	N
EGFP[a]	1021		$17.9^{+4.4}_{-3.6}$	1100^{7150}_{953}	$0.97^{-0.04}_{+0.04}$	690
His6-EGFP[b]	555		$15.0^{+5.7}_{-4.1}$	1870^{12200}_{1620}	$0.97^{+0.05}_{-0.05}$	220
GFP-MinD[c]	2017	438	$14.4^{+2.6}_{-2.2}$	322^{+422}_{-183}	$0.79^{+0.11}_{-0.11}$	217
GFP-MinD[c] l.i.		191	$14.7^{+3.0}_{-2.5}$	464^{+643}_{-274}	$0.86^{+0.08}_{-0.08}$	104
GFP-MinD[c] h.i.		247	$14.1^{+2.2}_{-1.9}$	230^{+209}_{-110}	$0.73^{+0.10}_{-0.10}$	113
GFP-MinD[d]	738	102	$12.4^{+1.8}_{-1.6}$	522^{+721}_{-303}	$0.84^{+0.07}_{-0.07}$	43
MinE-GFP[e]	1807	528	$9.3^{+2.3}_{-1.9}$	396^{+888}_{-274}	$0.86^{-0.09}_{+0.09}$	350
MinE-GFP[e] l.i.		310	$9.6^{+2.5}_{-2.0}$	478^{+1105}_{-334}	$0.88^{-0.08}_{+0.08}$	223
MinE-GFP[e] h.i.		218	$8.8^{+1.9}_{-1.5}$	285^{+542}_{-187}	$0.81^{-0.09}_{+0.09}$	127

Table 2.2: Mobility of EGFP, His6-EGFP, GFP-MinD, MinE-GFP - **exchange model**. D, τ_1: diffusion constant and residence time in the mobile state for proteins switching between a mobile and an immobile state, F: fraction of the faster/mobile population, N: number of curves allowing for a sufficiently good fit. Values were only considered from curves where the fit produced a $\chi^2 < 1.5$ (for EGFP $\chi^2 < 1.3$) and where the intensity was constant. Displayed are the mean values and the 1σ confidence interval. For EGFP, the values of D are well described by a log-normal distribution, while the values τ_1 vary too strongly as that, or any other, a distribution could be identified. For the Min proteins, the values of D, and τ_1 are well described by a log-normal distribution. For all strains, the values of F follow a normal distribution. [a]BL21(DE3)pLys, [b]BL21(DE3)pLys, [c]JS964, [d]WM1255, [e]WM1079.

2.3   Discussion

Here, we analyze and give an interpretation of the FCS data, while the implications of these measurements and of the video-rate-microscopy study for understanding the Min-oscillations will be discussed in the final chapter.

The possibility to apply FCS relies on the existence of quasi-stationary steady states in some regions of the bacterium for time intervals of at least 10s, see figures 2.17(c) and (f) and 2.25(a) and (b). Our correlation data clearly show the existence of more than one relaxation time, which can satisfactorily be explained by assuming for both, MinD and MinE, two states of different mobility. This is compatible with the current view that MinD and MinE are exchanged between the cytosol and the membrane. We interpret the faster component as resulting from the dynamics of cytosolic proteins. The second time-scale could result from the mobility of proteins in the membrane-bound state or from transitions between the cytoplasm and the membrane.

The measured correlation curves do not allow for to determining simultaneously all parameters associated with these processes. Therefore, we analyzed the data assuming that there are either no transitions between the cytosolic and the membrane-bound states or that membrane-bound proteins are immobile. The latter assumption is appropriate if the relaxation time resulting from diffusion of membrane-bound MinD or MinE is larger than the maximal time interval for which we recorded correlation curves. The same applies to the first assumption of negligible transitions between the two states. The differences in the corresponding correlation curves, see appendix A equations (A.0.1) and (A.0.2), are too small to be detected in our setup. Correspondingly, we found that all in all both models fit equally well to the data, even though for individual curves there can be significant differences in the fit quality. Another situation in which an analysis based on these reduced models is appropriate occurs when the relaxation times corresponding to the diffusion of membrane proteins and their transition between membrane and cytoplasm are similar. In that case, our analysis gives the values for both, the diffusion constant of membrane-bound proteins as well as the transition rate.

Using either the two correlation curves, G_{diff} or G_{ex}, for analyzing the experimental data, we found values around $16\mu\mathrm{m}^2/s$ and $10\mu\mathrm{m}^2/s$ for the respective cytosolic diffusion constants of GFP-MinD and MinE-GFP, where the latter quickly form dimers. The difference in these values confirms the findings of reference [88] that the diffusion constant is also determined by other factors than geometry, too. In fact, based on size alone, a MinE-GFP dimer of approximatively twice the size of GFP-MinD should have a diffusion constant of approximatively $13\mu\mathrm{m}^2/s$.

The values for the diffusion constants of membrane-bound proteins are approxima-

tively two order of magnitude smaller than the cytosolic constants and about one order of magnitude larger than the diffusion constant for mobile PleC in *Caulobacter* [87]. However, PleC is a transmembrane protein, whereas MinD binds to the polar heads of the lipids forming the membrane. Contrary to the cytosolic diffusion constant, the diffusion constants of membrane-bound MinE and MinD are the same. This is compatible with the MinE being bound to MinD on the membrane.

Comparing the different values measured in high- and low-intensity phases, respectively, we find that the fraction of cytosolic proteins is always larger in the low-intensity phases. Note, that FCS possibly overestimates the fraction of cytosolic proteins. In fact, membrane-bound MinD was reported to form helices [68], and if MinD in the helices is immobilized, it does not contribute to the fluctuations around the average intensity and can thus not be detected by FCS. Note also that the differences in the cytosolic fraction are present in individual cells, see figure 2.21(c) and 2.24(b). From the differences between the cytosolic fractions in the low- and high-intensity regions, one might expect also differences in the cytosolic residence time of MinE which requires MinD as a substrate to locate on the membrane. Assuming a cooperative attachment mechanism underlying the Min-oscillations, one might expect the same for the residence time of cytosolic MinD. While the mean values we measured follow this expectation, the differences are not significant in view of the error bars. We conclude that from our data only a small effect of membrane-bound proteins on the attachment rates of cytosolic proteins can be deduced.

Chapter 3

Deterministic analysis of the Min-oscillations

Introduction

In this chapter a theoretical study of the Min-oscillations will be performed. Previous investigations suggest that the periodic translocation of the Min proteins can be attributed to a collective effect of many interacting molecules resulting from a dynamic instability. In chapter one we divided all of the proposed models in two classes: CAM [69–75] and ACM [76, 77]. Central to all of the mechanisms is the attachment of MinD to the cytoplasmic membrane, recruitment of MinE to the membrane by MinD, and the dissociation of MinD from the membrane induced by MinE. Now, let us examine the deterministic models in more detail.

Aggregation current models. The essence of aggregation models is the formation of MinD-aggregates on the membrane by a two-step process: MinD first binds to the membrane and then aggregates, see figure 3.1. This characteristic distinguishes this mechanism from reaction-diffusion systems where the instability of the stationary homogeneous distribution that gives rise to oscillations is driven by the reactions. Here, the instability is driven by the aggregation current of MinD. MinD first binds to the membrane, then recruits MinE. However, the protein number is conserved.

Cooperative attachment models. The principal difference with AC models is that membrane-associated MinD aggregates are assumed to form in a one-step process where MinD form the cytosol binds directly to membrane-bound MinD. The first model of this kind was proposed by Meinhardt and deBoer [69]. The mechanism they considered belongs to the class of classical reaction-diffusion systems with short-range activation and

long-range inhibition, where the inhibition is due to substrate depletion. Both, MinD and MinE, attach cooperatively to the membrane. In addition, MinE binds to the membrane only in presence of membrane-bound MinD and the attachment rate depends on the concentration of membrane-bound MinD and MinE; it is maximal for a finite value of the MinD concentration and decays to zero for large concentrations of both membrane-bound MinD and MinE. The synthesis and degradation of the Min proteins plays an essential role. In particular, MinD and MinE are destroyed upon unbinding from the membrane.

Howard and coworkers [70], assume that MinD and MinE form complexes in the cytoplasm which then bind to the membrane. Membrane-binding is hampered by MinE present on the membrane. This mechanism does not fall into the class of classical reaction-diffusion systems as MinD and MinE protein numbers are conserved. Denoting the protein densities of cytoplasmic MinD and MinE as well as of MinD and MinE attached to the membrane by C_D, C_E, c_d, and c_e, respectively, the dynamic equation are

$$\partial_t c_D = D_D \partial_x^2 c_D - \frac{\omega_D c_D}{1 + \mu_e c_e} + \omega_{de} c_e c_d \tag{3.0.1}$$

$$\partial_t c_E = D_E \partial_x^2 c_E - \omega_D c_D c_E + \frac{\omega_e c_e}{1 + \mu_D c_D} \tag{3.0.2}$$

$$\partial_t c_d = \frac{\omega_D c_D}{1 + \mu_e c_e} - \omega_{de} c_e c_d \tag{3.0.3}$$

$$\partial_t c_e = \omega_{de} c_D c_E - \frac{\omega_e c_e}{1 + \mu_D c_D} \tag{3.0.4}$$

where ω_D describes the spontaneous rate of MinD binding to the membrane, $\omega_{DE} c_D$ the rate of MinE recruitment to the membrane by cytoplasmic MinD, $\omega_{de} c_e$ the rate of MinE induced dissociation of MinD, and finally ω_e is the spontaneous rate of MinE release from the membrane. Spontaneous dissociation of MinD from the membrane and spontaneous association of MinE with the membrane were neglected in agreement with experiments. The parameters μ_e and μ_D describe suppression of MinD binding to the membrane due to membrane-bound MinE and suppression of MinE unbinding from the membrane due to cytoplasmic MinD. A similar model based on a combination of geometric effects and reaction-diffusion dynamics, was applied to study protein localization in *Bacillus subtilis* [103].

In the model proposed by Huang et al. [71] the CA characteristic has remarkable consequences. Firstly, it is essential to describe the Min dynamics in a three-dimensional geometry to obtain striped oscillatory patterns in long cells. Secondly, a finite ADP to ATP exchange rate for cytosolic MinD is a key ingredient. The one dimensional version

of the equations is the following:

$$\partial_t c_{DD} = D_D \partial_x^2 c_{DD} - \omega_{DT} c_{DD} + \omega_{de} c_{de}, \tag{3.0.5}$$

$$\partial_t c_{DT} = D_D \partial_x^2 c_{DT} - \omega_{DT} c_{DD} - [\omega_D + \mu_{dD}(c_d + c_{de})]c_{DT}, \tag{3.0.6}$$

$$\partial_t c_E = D_E \partial_x^2 c_E + \omega_{de} c_{de} c_E, \tag{3.0.7}$$

$$\partial_t c_d = -\omega_E c_d c_E + [\omega_D + \mu_{dD}(c_d + c_{de})]c_{DT}, \tag{3.0.8}$$

$$\partial_t c_{de} = \omega_{de} c_{de} - \omega_E c_d c_E . \tag{3.0.9}$$

Here, c_{DD} and c_{DT} denote the cytosolic distributions of MinD bound to ADP and to ATP, respectively. Furthermore ω_D is the rate of spontaneous binding of MinD-ATP to the membrane, μ_{dD} describes the modification of this rate due to the presence of MinD on the membrane, while ω_{DT} describes the rate of exchange of ADP to ATP in cytosolic MinD. As transport is purely diffusive, the instability leading to the oscillations is in this case essentially of the same kind as in the other reaction diffusion systems [69, 70]. These equations were also analyzed in a spherical geometry [104].

A first attempt to introduce the polymerization mechanism in the model was carried out by Drew et al. [72]. They made the following assumptions: (i) initial MinD attachment to the membrane can only occur at or near the pole; (ii) membrane-bound MinD recruits cytoplasmic MinD to form polymers, extending from the polar binding site to mid-cell; (iii) MinE has a higher binding affinity for terminal MinD units of the polymers than to internal units. In contrast to all previous models, here, a polar zone formation is initiated specifically at nucleation sites at the cell pole. On the other hand, the existence of stripes in long cells where the division is blocked, suggests that the polar location in normal cells is not the result of a membrane property unique to the ends of the cell.

In this chapter an AC model, conceptually similar to the model introduced by Kruse [76] is being considered. In [76] the aggregation of membrane-bound MinD was formulated in terms of a kinetic hopping model. Here, we will use a phenomenological description which allows for a quantitative comparison with experimental results. The chapter is organized as follows: First, we will describe the equations governing the dynamics of the protein distributions in the cytosol and on the membrane. We then analyze the system in the limiting case of homogenous cytosolic protein distributions and discuss the oscillatory solutions. The dependence of the temporal oscillation period on the system length is then compared to experimental data. Afterwards we discuss possible
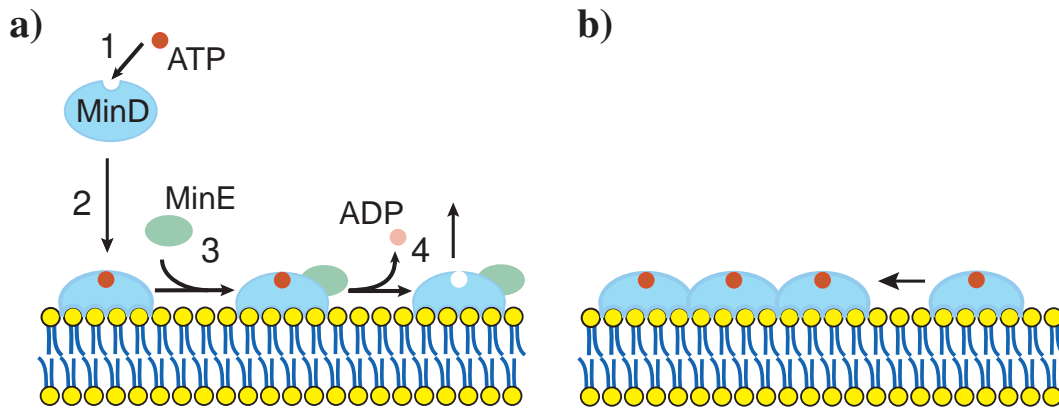
Figure 3.1: Schematic representation of the dynamics of MinD and MinE. a) Exchange of MinD and MinE between the cytosol and the membrane. 1) MinD undergoes a conformational change upon binding ATP, 2) ATP-bound MinD binds to the membrane, 3) MinE binds to membrane-bound MinD, and 4) MinE-induced ATP hydrolysis leads to detachment of MinDE-complexes from the membrane. b) Interaction of membrane-bound proteins leads to the formation of MinD aggregates.

mechanisms underlying the formation of the MinE-ring. Finally, our results in relation to the other proposed mechanisms as well as implications for possible future experiments will be discussed.

3.1   Dynamic equations

As mentioned in chapter one, the periodic changes in the distributions of the Min proteins require the presence of MinD and MinE but not of MinC. Therefore, in the following we will focus on the dynamics of MinD and MinE. Motivated by experimental observations, the dynamics of the Min proteins is assumed to be driven by four properties of the Min proteins [76]: (i) a high affinity of ATP-bound MinD for the membrane; (ii) a high affinity of MinE for membrane-bound MinD; (iii) a MinE-induced increase of the ATP hydrolysis-rate by MinD which leads to the detachment of MinDE-complexes from the membrane; and (iv) interactions between membrane-bound proteins. The last property accounts for the formation of MinD aggregates on the membrane which is likely to result from self-assembly of membrane-bound MinD [66, 68]. In addition, proteins are transported by diffusion. A schematic representation of the Min dynamics is given in figure 3.1.

Formally, the dynamics is given in terms of the concentrations of cytosolic MinD and

MinE, c_D and c_E[1], as well as the concentrations of membrane-bound MinD and MinDE-complexes, c_d and c_{de}. In the direction perpendicular to the long axis of the bacterium, diffusion homogenizes the cytosolic distributions on time scales that are short when compared to the temporal oscillation period. Assuming in addition that MinD aggregates into a linear structure on the membrane, the dynamical equations for the protein densities in the cell can thus be reduced so that they depend only on the position x along the long axis of the bacterium, see appendix C. Explicitly,

$$\partial_t c_D = -\omega_D(c_{\max} - c_d - c_{de})c_D + \omega_{de}c_{de} + D_D\partial_x^2 c_D \qquad (3.1.1)$$

$$\partial_t c_E = \omega_{de}c_{de} - \omega_E c_d c_E + D_E\partial_x^2 c_E \qquad (3.1.2)$$

$$\partial_t c_d = \omega_D(c_{\max} - c_d - c_{de})c_D - \omega_E c_d c_E - \partial_x j_d \qquad (3.1.3)$$

$$\partial_t c_{de} = -\omega_{de}c_{de} + \omega_E c_d c_E - \partial_x j_{de} \qquad (3.1.4)$$

The properties (i)-(iii) lead to an exchange of MinD and MinE between the cytosol and the membrane. The corresponding reactions are described as first- and second-order processes. The density of available binding sites for MinD on the membrane is given by $c_{\max} - c_d - c_{de}$, where $c_{\max}$ is the maximal possible value for the protein density on the membrane, and $\omega_D(c_{\max} - c_d - c_{de})$ is the binding rate of MinD to the membrane. The binding rate of MinE to membrane-bound MinD is $\omega_E c_d$, while ω_{de} is the detachment rate of MinDE complexes from the membrane. That complexes are assumed to consist of one MinD and one MinE molecule. D_D and D_E are the respective diffusion constants for cytosolic MinD and MinE, and the interactions of membrane-bound proteins are captured by the currents j_d and j_{de}. Note that in these equations the re-binding of ATP to MinD after detachment from the membrane is assumed to occur on a sufficiently short time-scale so that it does not need to be incorporated explicitly. The effect of a finite ATP exchange rate will be discussed below.

The current of membrane-bound MinD has a diffusive part and a part due to the interaction between MinD proteins. In order to capture generic effects of the interaction, the current of membrane-bound MinD is taken to be of the Cahn-Hilliard form. Explicitly,

$$j_d = -D_d\partial_x c_d + c_d(c_{\max} - c_d - c_{de})[k_1\partial_x c_d + k_2\partial_x^3 c_d + \bar{k}_1\partial_x c_{de} + \bar{k}_2\partial_x^3 c_{de}]. \qquad (3.1.5)$$

In this expression, D_d is the diffusion constant of the MinD proteins on the membrane and the coefficients k_1 and k_2 are phenomenological parameters that describe the interaction between MinD molecules. Possible modifications of this interaction due to the presence

---

[1]MinE forms dimers [105] and c_E is actually the distribution of MinE dimers. In the following, the term "MinE molecules" will refer to these dimers.

of MinE are taken into account by the parameters $\bar{k}_1$ and $\bar{k}_2$ that describe the interaction between MinD and MinDE-complexes. Note that for an attractive interaction $k_1 > 0$, while $k_1 < 0$ in the opposite case. Stability on small length scales requires $k_2 \geq 0$. The current of MinDE complexes has the same form, but for simplicity will be omitted in the following.

Finally, the boundary conditions need to be specified. Experiments have shown that oscillations are independent of protein synthesis [63], and therefore apparently do not directly rely on the regulation of gene expression. Therefore, we impose zero flux at the boundaries so that the total protein numbers

$$\int_{-L/2}^{L/2} dx \, (c_D + c_d + c_{de}) \;\equiv\; L\mathcal{D} \tag{3.1.6}$$

$$\int_{-L/2}^{L/2} dx \, (c_E + c_{de}) \;\equiv\; L\mathcal{E} \tag{3.1.7}$$

are conserved. Here, L denotes the length of the system and $L\mathcal{D}$ and $L\mathcal{E}$ are the total numbers of MinD and MinE molecules in the system, respectively.

3.2 Homogenous cytosolic distributions

We now analyze the dynamic equations (3.1.1)-(3.1.4) in the limiting case of homogenous cytosolic MinD and MinE distributions, i.e., $c_D(x,t) = c_D(t)$ and $c_E(x,t) = c_E(t)$. This corresponds to the case where the times t_{diff} needed for MinD and MinE to diffuse along the whole length of the bacterium, equal to L^2/D_D and L^2/D_E respectively for MinD and MinE, are short as compared to all other relevant time-scales involved. According to the measured values for the diffusion constants, t_{diff} ranges from $0.1s$ for cells 1μm long, to $1s$ for cells 10μm long. Considering the residence time values shown in the previous chapter, the cytosolic distribution can be considered homogenous for cell lengths of 2μm or less.

In this case, the dynamics of the cytosolic distributions is described by ordinary differential equations

$$\frac{d}{dt}c_D \;=\; -\omega_D(c_{\max} - \mathcal{D} + c_D)c_D + \omega_{de}(\mathcal{E} - c_E) \tag{3.2.1}$$

$$\frac{d}{dt}c_E \;=\; -\omega_E(\mathcal{D} - \mathcal{E} - c_D + c_E)c_E + \omega_{de}(\mathcal{E} - c_E) \quad . \tag{3.2.2}$$

Here, the distributions of membrane-bound MinD and MinDE were eliminated using equations (3.1.6) and (3.1.7).
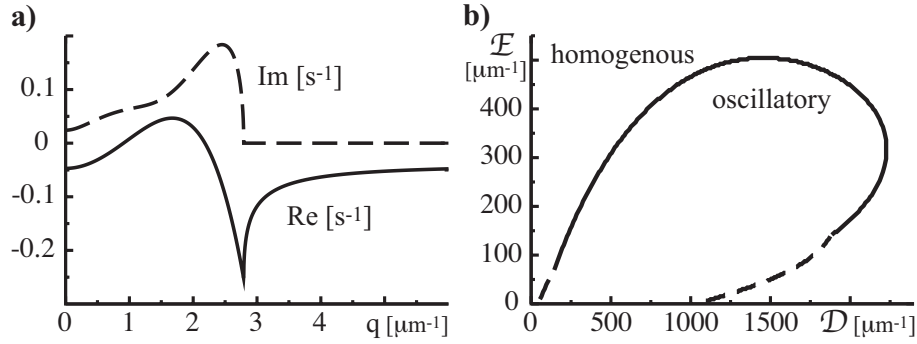
Figure 3.2: Linear stability of the homogenous state. a) Real (Re, solid line) and imaginary part (Im, dashed line) of the eigenvalues of the linear operator describing the dynamics of small perturbations around the homogenous state as a function of the wave number q. Modes with wave numbers between $1\mu m^{-1}$ and $2.2\mu m^{-1}$ are oscillatory and unstable. b) Stability of the homogenous state as a function of the average total MinD and MinE densities $\mathcal{D}$ and $\mathcal{E}$. The solid line indicates a line of oscillatory instabilities while the dashed lines indicate stationary instabilities. The values of the parameters are $\omega_D = 4 \cdot 10^{-5}\mu m s^{-1}$, $\omega_E = 3 \cdot 10^{-4}\mu m s^{-1}$, $\omega_{de} = 0.04 s^{-1}$, $D_d = 0.06\mu m^2 s^{-1}$, $c_{max} = 1000\mu m^{-1}$, $k_1 = 1.5 \cdot 10^{-6}\mu m^4 s^{-1}$, $k_2 = 1.8 \cdot 10^{-7}\mu m^6 s^{-1}$, $\bar{k}_1 = -1.2 \cdot 10^{-6}\mu m^4 s^{-1}$, $\bar{k}_2 = 1.2 \cdot 10^{-10}\mu m^6 s^{-1}$. In (a) $\mathcal{D} = 900\mu m^{-1}$ and $\mathcal{E} = 350\mu m^{-1}$.

Under the conditions $0 \leq c_D \leq \mathcal{D}$ and $0 \leq c_E \leq \mathcal{E}$, the above equations have one and only one fixed point. This point is always stable and, asymptotically, the cytosolic distributions will approach the corresponding stationary values C_D and C_E, respectively. In this limit, the dynamics of the Min proteins is described by two partial differential equations for the distributions of the proteins bound to the membrane:

$$\partial_t c_d = \omega_D C_D (c_{max} - c_d - c_{de}) - \omega_E C_E c_d - \partial_x j_d \qquad (3.2.3)$$

$$\partial_t c_{de} = -\omega_{de} c_{de} + \omega_E C_E c_d \quad . \qquad (3.2.4)$$

Note that the reaction terms in these equations are linear and describe relaxation to a stationary value; only the current contains non-linearities and can generate an instability. This feature distinguishes this system from classical reaction-diffusion systems, where transport is due to diffusion and where instabilities are created by the reaction terms.

The homogenous state $c_d(x) = \mathcal{D} - \mathcal{E} - C_D + C_E$ and $c_{de}(x) = \mathcal{E} - C_E$ is a stationary state of the dynamic equations (3.2.3) and (3.2.4). It is stable, unless k_1 exceeds a critical value $k_{1,c}$. The results of a linear stability analysis for a supercritical value of k_1 are shown in figure 3.2(a). The stability region of the homogenous state as a function of the total MinD and MinE concentrations, $\mathcal{D}$ and $\mathcal{E}$, is shown in figure 3.2(b). At the instability an inhomogeneous stationary state appears if the detachment rate of MinDE complexes
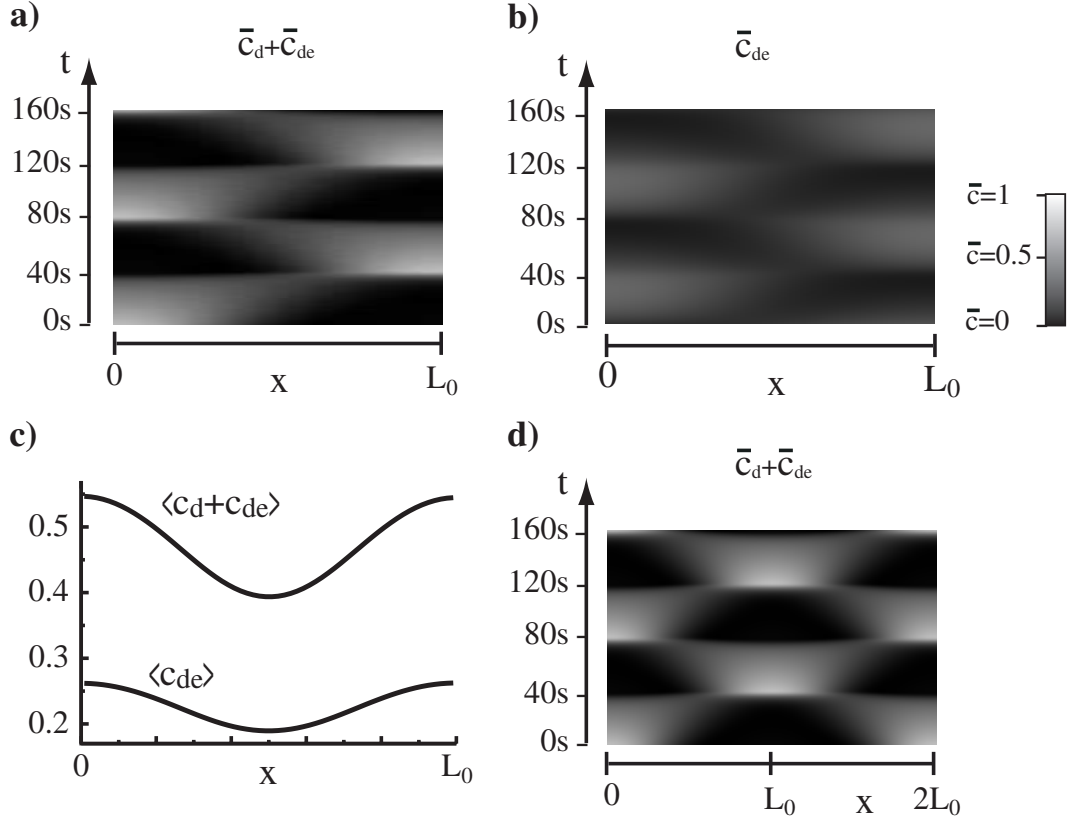
Figure 3.3: Oscillatory solutions of the dynamic equations (3.2.3) and (3.2.4). a,b) Space-time plots of the total MinD and MinDE distributions on the membrane, $\bar{c}_d + \bar{c}_{de} = (c_d + c_{de})/c_{max}$ and $\bar{c}_{de} = c_{de}/c_{max}$, respectively, for system size $L_0 = 2\mu$m. Both distributions show pole-to-pole oscillations with a temporal period of about 80s. c) The total MinD and the MinDE distribution averaged over one temporal period shown in (a) and (b), $\langle \bar{c}_d + \bar{c}_{de} \rangle$ and $\langle \bar{c}_{de} \rangle$. Both distributions display a clear minimum at $x = L_0/2$. d) Space-time plot of the total MinD distribution on the membrane, $\bar{c}_d + \bar{c}_{de}$ for system size $2L_0$. The pattern has doubled as compared to the pattern in the system of length L_0. Parameters are $k_1 = 2.1 \cdot 10^{-6} \mu$m$^4 s^{-1}$, $k_2 = 2.5 \cdot 10^{-7} \mu$m$^6 s^{-1}$, and the remaining values as in figure 3.2(a).

from the membrane is above a certain critical value, $\omega_{de} > \omega_{de,c}$. In the opposite case, an oscillatory state appears. Oscillatory instabilities only occur if the protein density on the membrane cannot exceed a maximal value $c_{\max}$. For an oscillatory instability the unstable mode is of the form

$$c_d \quad \propto \quad \cos(\Omega_c t)\cos(q_c x) \tag{3.2.5}$$

$$c_{de} \quad \propto \quad \cos(\Omega_c t + \phi)\cos(q_c x) \tag{3.2.6}$$

This standing wave reflects the qualitative features of the observed Min-oscillations. The wave number $q_c = n\pi/L$, where n is a natural number, and the frequency Ω_c of the critical mode depend on the system parameters. For instance, we find

$$q_c^4 = \frac{(\omega_D C_D + \omega_{de} + \omega_E C_E)}{C_d(c_{\max} - C_d - C_{de})k_2} \quad , \tag{3.2.7}$$

and if $\bar{k}_1 = \bar{k}_2 = 0$

$$\Omega_c^2 \quad = \quad \omega_D \omega_E C_D C_E - \omega_{de}^2 \tag{3.2.8}$$

A linear stability analysis in term of microscopic parameters associated with the phenomenological parameters k_1 and k_2 and for the non-homogenous cytosolic case is given in appendix D.

The oscillatory patterns can be obtained from the numerical integration of the dynamic equations (3.2.3) and (3.2.4) (see appendix E for a remark about the numerical stability criterion valid for the these equations). A typical example is shown in figures 3.3(a) and (b). For some time the total MinD-distribution $c_d + c_{de}$ is localized in the one half and then switches to the other. In this process, the transition time is very short when compared to the dwell time in the one half. This is in agreement with the experimental observations shown in chapter one, in particular with the presence of the quasi-steady state. The MinE distribution shows a similar behavior, but the transition between the two halves is less rapid. The time-averaged distribution of both, MinD and MinE shows a minimum in the center and increases towards the system boundaries, see figure 3.3(c). The parameters were chosen so that the temporal period is about 80s, which is similar to the values observed in experiments with fluorescently labelled MinD, see figure 2.10. The figure also displays the time-averaged MinD-distribution with a minimum in the center.

In the model, the transition of MinD from the one half to the other can be understood as follows. If MinD is localized in the one half, MinE will bind and drive MinD off the
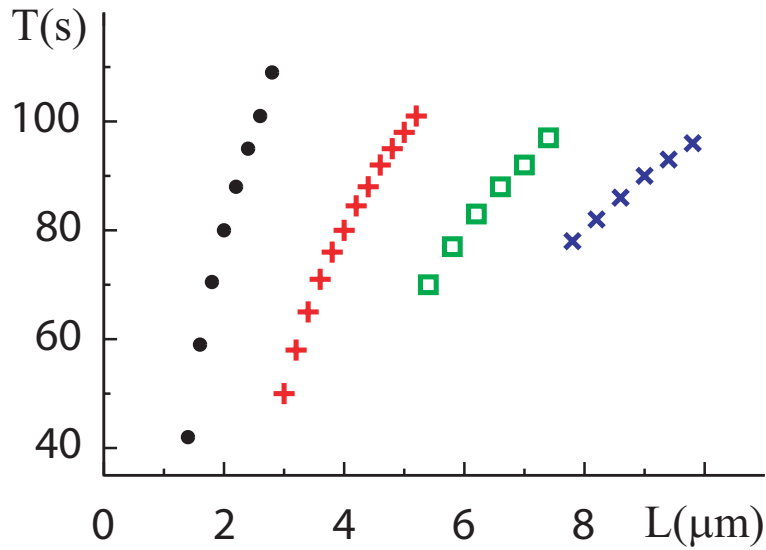
Figure 3.4: Oscillation period of solutions to the equations (3.2.3) and (3.2.4) as a function of the system length. Black dots: oscillation pattern as in figure 3.3(a), red crosses: oscillation pattern as in figure 3.3(b), green and blue dots: oscillation pattern with three and four stripes, respectively. For the system length where the oscillation pattern changes, the period shows a discontinuity. The parameters values are as in figure 3.3(a).

membrane. Although the distribution of cytosolic MinD is homogenous, MinD preferentially binds in the other half because there are more available binding sites. The resulting inhomogeneity of membrane-bound MinD is then amplified by MinD aggregation. As a consequence of the homogenous distribution of cytosolic MinE, the spatial dependence of the attachment rate of MinE follows the profile of membrane-bound MinD, and the distribution of MinDE complexes is similar to the one of MinD on the membrane, see figure 3.3(a) and (b). In particular, the positions of the maxima of c_{de} are linked to the position of the maxima of c_d. In the example given in figures 3.3(a) and (b), the maxima are always located at the boundaries $x = 0$ and $x = L$.

As the system size is increased, the patterns change and the striped patterns for c_d and c_{de} appear, see figure 3.3(d). This reflects the finite wave number of the critical mode. In addition to changes in the oscillation pattern, the temporal period also changes as the system size is varied. It increases monotonically with the system size but at certain sizes jumps back towards a lower value, see figure 3.4. The discontinuities occur for the system sizes where the oscillatory pattern acquires a new "stripe". For the parameter values used here, a new stripe appears for a system size of 3μm. In the case displayed in figure 2.10(f), the minimum at the center is more pronounced than for the theoretical calculation: while experimentally the minimum is at about 50% of the maximum, it is at about 70% in the
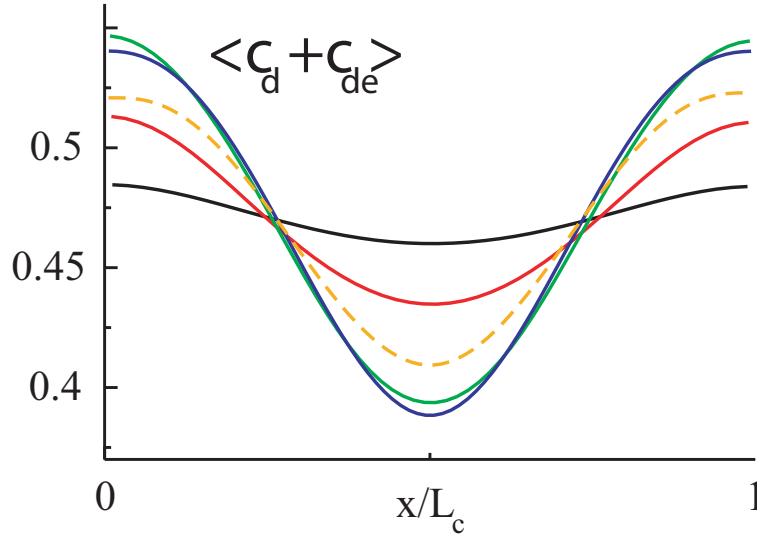
Figure 3.5: Oscillatory solutions of the dynamic equations (3.2.3) and (3.2.4). The total MinD distribution averaged over one temporal period, $\langle \bar{c}_d + \bar{c}_{de} \rangle$, for different lengths. The black, red, green and blue lines correspond to cell length of 1.4μm, 1.6μm, 2.0μm and 2.6μm respectively. The orange dashed curve corresponds to a cell length of 2.8μm, just before the system acquires a new stripe. Parameters are $k_1 = 2.1 \cdot 10^{-6} \mu \text{m}^4 s^{-1}$, $k_2 = 2.5 \cdot 10^{-7} \mu \text{m}^6 s^{-1}$, and the remaining values are as in figure 3.2(a).

numerics. However, as is shown in figure 2.12, for other cells examined, the minimum is much shallower or even absent. This might reflect deviations in the total protein density in individual bacteria from the average total protein density in a bacterial colony. In particular, in the numerics, see figure 3.5, the value of the minimum decreases with the system length up to the point at which the oscillation pattern acquires a new stripe. This behavior is consistent with the experimental data shown in in figure 2.12. It would be interesting to test this dependence of the average MinD distribution on the cell length in single cells.

When increasing the cell length, the oscillation periods found for the dynamic equations (3.2.3) and (3.2.4), see figure 3.4, span the same range as the experimentally observed ones, shown in figure 2.14. Furthermore, experimentally we observed striped oscillation patterns only for bacteria longer than 3μm, however, there is no sharp transition length in which the pattern changes. This behavior, as has been described in section 2.1.3, could be due to variations in the protein densities between different bacteria, and the consequent variation of the oscillation period [63], and thus reflect the individuality of the cells. It could also be a noise effect due to the low protein number which gives rise to fluctuations in the oscillation period in each single cell. An experimental verification would require the measurement of the protein concentration in an individual cell together

a)   **b)**
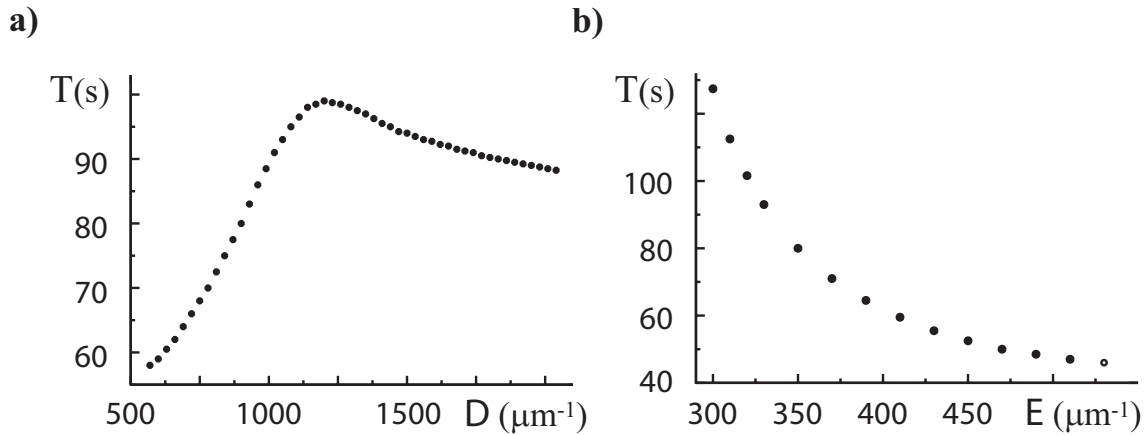
Figure 3.6: a) Oscillation period in the model as a function of the average total MinD concentration $\mathcal{D}$. The period initially increases and then decreases slightly with $\mathcal{D}$. b) The same as (a) but for the average total MinE concentration $\mathcal{E}$. The period decreases with the amount of MinE. The parameters values are as in figure 3.3(a), the system length is 2μm.

with the temporal period and the cell length.

In the model, the temporal oscillation period also depends on the total MinD and MinE concentrations, $\mathcal{D}$ and $\mathcal{E}$, see figure 3.6(a) and (b). It increases monotonically with the amount of MinD until it starts to descend slightly. As a function of the number of MinE molecules, the period decreases.

3.3   The MinE-ring

In the one-dimensional description presented above, MinE-rings correspond to the maxima in the MinDE distribution. In the examples given so far, such maxima only occur at the system boundaries. For system lengths close to the value at which the pattern acquires a new stripe, maxima can be detected closer to the system's center. However, this is unlikely to be the mechanism for MinE-ring formation in *E. coli*, because no dependence of the existence of the ring on the cell size was reported. Furthermore, as argued above, in the limit of homogenous cytosolic MinD- and MinE-distributions, the maxima in the MinDE-distribution were induced by the maxima in the MinD-distribution. MinD-rings were not observed experimentally, though.

There are at least three other possible mechanisms that may, in principle, account for the observed accumulation of MinE at the ends of the MinD helix. In the first mechanism, the diffusion length of cytosolic MinE, $l_E = (D_E/\omega_E c_{\max})^{1/2}$, is shorter than half of the cell length. In this case, cytosolic MinE will predominantly attach before it has reached the opposite cell pole, which might lead to an accumulation close to the cell

center. This seems to be the mechanism of MinE-ring formation in the models proposed in [70, 71]. Accordingly, the ring vanished in [71] when the attachment rate of MinE was reduced, leading to an increase of l_E. To test whether this mechanism is supported by the equations (3.1.1)-(3.1.4), we studied the system for finite values of D_D and D_E. In this case the cytosolic distributions c_D and c_E were not homogenous, and all four equations had to be solved simultaneously. For the parameter values considered above, the oscillation patterns do not change significantly as long as the diffusion constants D_D and D_E are larger than $0.1 \mu m^2/s$ and no maxima of c_{de} independent of maxima of c_d were found. The diffusion length l_E is also influenced by the value of ω_E. For $D_D = D_E = 2.5 \mu m^2/s$, the values for diffusion in the cytosol used in CA models, and values of ω_E smaller than $3.2 \cdot 10^{-4} \mu m/s$ the same behavior was found. Still larger values of ω_E destroy the oscillations. Note that by assumption the one-dimensional description is only appropriate if the diffusion length l_E is larger than the cell diameter, i.e., $l_E \geq 1 \mu m$. We concluded that this mechanism is not supported by the dynamic equations presented above and can be tested only in a three-dimensional description.

Two other mechanisms of minE-ring formation are suggested by studies of kinesin-subfamily Kin13 members [106, 107]. These proteins induce the depolymerization of microtubules. In this process they accumulate at both ends of the microtubule. As MinE might act on MinD filaments in much the same way, accumulation of MinE could follow from a similar mechanism as accumulation of the Kin13-kinesins. The latter could be a consequence of a higher affinity of the microtubule end for binding the motor. Related ideas for the binding of MinE to MinD were proposed in [69] and also in [76]. In the present description, additional terms as the special functional form for the attachment of MinE to the the membrane-bound MinD used in [76], can give a MinE-ring. The analogy with Kin13-kinesins offers still another explanation for the accumulation of MinE, namely a dynamic accumulation due to processive depolymerization [108]. The present framework for studying the dynamics of Min-proteins is not suitable for studying these effects as filaments are not explicitly incorporated.

3.4 Discussion

A phenomenological description of the dynamics of MinD and MinE in *E. coli* has been presented. The description is based on the binding of MinD to the cytosolic membrane, recruitment of MinE to the membrane by membrane-bound MinD, MinE-induced detachment of MinD, as well as an interaction between molecules bound to the membrane. For a sufficiently strong attraction between membrane-bound MinD-molecules, these processes generate pole-to-pole oscillations of the Min-proteins. The phenomenological form of the

current for membrane-bound MinD used in the present work captures generic features of the protein interaction and does not refer to a specific microscopic mechanism. It allows for a quantitative comparison between the oscillatory solutions of the dynamic equations and experimental findings. In agreement with the latter, oscillations with a temporal period from 40s to 120s can be obtained. This value is essentially determined by the detachment rate ω_{de} of MinDE-complexes. For the parameter values given in the text, the oscillatory pattern acquires a second stripe for a system size of 3μm, which agrees well with the smallest bacterial length for which period doubling is seen in figure 2.14. This length is essentially determined by the ratio of the parameters k_1 and k_2.

Our analysis of the dynamic equations (3.1.1)-(3.1.4) was focused on the case of homogenous cytosolic distributions of MinD and MinE, c_D and c_E. The solutions in this limit are very similar to the solutions of the full equations if the diffusion constants of both MinD and MinE have the measured value of approximatively 15μm^2/s. This implies that the approximation of constant c_D and c_E is appropriate and provides a reduced set of equations that is more convenient to study than the four equations of the full system. An implication of our analysis is that the number of available binding sites might need to be limited in order to produce oscillations.

Other mechanisms that were suggested for the Min-oscillations agree in the essential assumptions with the one studied here, namely the ability of ATP-dependent binding of MinD to the membrane, the recruitment of MinE to the membrane by MinD, and the release of MinD from the membrane driven by MinE. The proposed mechanisms differ, however, in essential points. Meinhardt and deBoer suggested that protein synthesis might be an essential element [69], which is not supported by experiments where the synthesis of proteins was interrupted and the oscillations still continued [63]. Howard et al. assumed that MinD and MinE form complexes in the cytosol and bind together to the membrane [70]. They found an exponential increase of the temporal period of the oscillations with the system length with a period of 1000s for a system of length 7μm. This is qualitatively different from the behavior reported for the mechanism examined in our study, see figure 3.4(a). The experimental data presented in figure 3.4(b) show oscillation periods that do not exceed 120s for bacteria of a length of up to 10μm. However, more experiments are needed in particular for obtaining simultaneously values for the protein densities and the oscillation period of individual bacteria.

The system studied by Huang et al. differs from the one studied here in the way that MinD-aggregates are formed on the membrane [71]. In their description, MinD aggregation follows a one-step process: attachment to the membrane occurs with a higher rate at locations where MinD is already bound. This characterizes the models that we define as cooperative attachment models. In contrast, we considered a two step-process, namely,

cytosolic MinD binds first to the membrane and only then self-assembles into a filament, corresponding to an aggregation current model. This difference might at first sight seem minor. However, it leads to striking differences in the behavior of the models. First of all, in assuming a one-step process for MinD aggregation, a three-dimensional geometry as well as a finite ATP-exchange rate is required to generate striped oscillation patterns in long systems. Secondly, in the model by Huang et al. there are no oscillatory solutions at all for homogenous cytosolic distributions. Moreover, in contrast to the model by Huang et al., MinE-rings were not found to form in the model studied here.

In chapter five the differences between the two classes of models ACM and CAM will be further discussed and, suggesting new experiments, the implications of our measurements concerning the possibility of quantitatively discerning between different models will be also considered.

Fluctuations due to the moderate number of Min-molecules might also play an important role. This point will be addressed in the next chapter.

Chapter 4

Stochastic description of the Min-oscillations

> In that Empire, the Art of Cartography attained such Perfection that the map of a single Province occupied the entirety of a City, and the map of the Empire, the entirety of a Province. In time, those Unconscionable Maps no longer satisfied, and Cartographers Guilds struck a Map of the Empire whose size was that of the Empire, and which coincided point for point with it. The following Generations, who were not so fond of the Study of Cartography as their Forebears had been, saw that that a vast Map was Useless, and not without some Pitilessness was it that they delivered it up to the Inclemencies of the Sun and Winters. In the Deserts of the West, still today, there are Tattered Ruins of the Map, inhabited by Animals and Beggars; in all the Land there is no other Relic of the Disciplines of Geography.
>
> Jorge Luis Borges and Adolfo Bioy Cesares, "On Exactitude in Science"[1]

Introduction

In this chapter our theoretical investigations on the oscillatory Min-system will be extended on the effects of fluctuations. Because the number of involved Min molecules in each bacterium is rather small, only a few thousand [109, 110], stochastic fluctuations are expected to be significant [83, 111]. Unfortunately, there are only measurements of protein numbers averaged over a population of cells [110]. As a consequence, assuming an average length of the cell, only an approximate estimation of 700 MinE/μm and

---

[1]English translated version from J. L. Borges, *Collected Fictions*, A. Hurley, trans., Penguin, New York (1999).
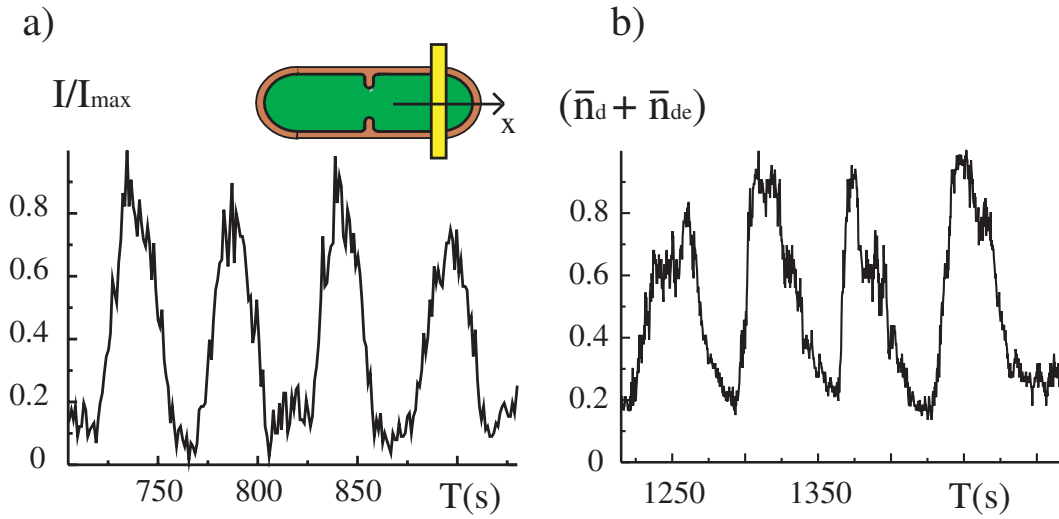
Figure 4.1: MinD oscillations. (a) Fluorescence intensity I of MinD-GFP measured by LSCM, rescaled by the maximum value $I_{\max}$ during the oscillations (in a confocal volume corresponding to the yellow area in the sketch), as a function of the time. b) Stochastic simulations of MinD concentration on the membrane, as explained in the tex, $\bar{n}_d + \bar{n}_{de} = (n_d + n_{de})/n_{\max}$ at site $i = 1, 2$, as function of the time.

1000 MinD/μm is possible, corresponding to a concentration of approximately 1μM. Figure 4.1 clearly shows fluctuations in the oscillatory fluorescence intensity signal due to the low number of proteins. All of the FCS measurements we performed (see section 2.2) were only possible because of the presence of such fluctuations.

The effects of noise were studied for some spatially extended patterns, *e.g.* Ca^{++} distributions [112–116]. Inside the cells, mostly models without spatial degrees of freedom were considered [117–119]. Only recently, first attempts to study the influence of fluctuations on the Min-oscillations were undertaken [74, 75, 120–122]. All these studies were carried out in the context of CA models. A stochastic study was carried out also for a different bacterial system, namely Soj proteins in *Bacillus subtilis* [123].

Howard and Rutenberg [120] considered a stochastic model of discrete particles moving in a one-dimensional lattice. The occupancy at site i is $n_j^{\{i\}}$, with $j = D, d, E, e$ representing cytoplasmic MinD, membrane MinD, cytoplasmic MinE, and membrane MinE, respectively. Given the size of a lattice site Δx, in a time Δt, particles hop to the neighboring sites with probabilities $D_j \Delta t/(\Delta x)^2$. The transformation of cytosolic particles into membrane bound particles and vice versa occurs in the same time interval with prob-

abilities given by

$$P_{D \to d} = \tilde{\omega}_D \Delta t / (1 + \tilde{\mu}_e n_e^{\{i\}}), \tag{4.0.1}$$

$$P_{d \to D} = \tilde{\omega}_{de} n_e^{\{i\}} \Delta t, \tag{4.0.2}$$

$$P_{E \to e} = \tilde{\omega}_{DE} n_D^{\{i\}} \Delta t, \tag{4.0.3}$$

$$P_{e \to E} = \tilde{\omega}_e \Delta t / (1 + \tilde{\mu}_D n_D^{\{i\}}). \tag{4.0.4}$$

Numerical simulations of this model show pole-to-pole oscillations for particle numbers in which the corresponding continuum model [70] does not oscillate. Particularly interesting is the result at low protein concentrations, where fluctuations induce and sustain oscillatory patterns.

A one-dimensional stochastic model incorporating membrane polymerization of MinD, was considered by Tostevin and Howard [74]. In this context, they also studied Min oscillations during the division process, simulating a closing septum through its effects on the cytosolic diffusion constant. In agreement with reports of oscillations in constricting cells [61, 63], and with our observation of unaffected oscillations during division[2], they found that oscillations cut off sharply at some time during the closing of the septum and then the daughter cells show independent oscillations. They also found that the fraction of Min-proteins in the daughter cells vary widely, from $50\% - 50\%$ up to $85\% - 15\%$ of the total from the parent cell. In the most extreme cases, due to the low protein number, oscillations were not supported in one of the daughter cells. However, wt[3] cells without pole-to-pole oscillations have not been reported so far.

Pavin *et al.* [73] considered a 3-D stochastic extention of the model proposed by Huang *et al.* Their model generated pole-to-pole oscillations of the membrane-associated MinD proteins, MinE ring, as well as filaments of the membrane-bound MinD proteins. To this end they considered four different rates for the detachment process of MinDE:ATP complexes, depending on many bonds a MinD:ATP formed with its MinD:ATP neighbors. In particular, in order to generate oscillations, the rate corresponding in the case of four bound ones has to be significantly small when compared with the others.

Different stochastic versions of the model introduced in [71] were considered in [75, 121, 122].

Kerr *et al.* [75] made stochastic simulations in three spatial dimensions of the model introduced by Huang *et al.* [71], using MCELL, a Monte Carlo modeling program for cellular microphysiology [124]. In contrast to Howard and Rutenberg [120] they found

---

[2]Figure 2.7 is one single frame of a video showing such behavior in a long cell, just before the birth of a minicell (right down). Oscillation started immediately in the new-born cell.

[3]Of course to be observed cells have to express GFP fused proteins.

that fluctuations destroy oscillations in the range of values of the protein numbers where the deterministic version of the model still shows oscillations.

Finally, Fange and Elf [122] considered $3-D$ stochastic reaction-diffusion kinetics of the Min proteins for all documented mutant phenotypes and compared the results to the corresponding deterministic mean-field description. They found that wt and $ftsZ^-$ cells are well described by the mean-field model but that a stochastic model is necessary to reproduce the characteristics of the spherical ($rodA^-$) and phospathedylethanolamide-deficient (PE^-) phenotypes[4]. In particular, for spherical cells, the mean-field model is bi-stable and the system can get trapped in a non-oscillatory state, however, when the intrinsic noise is considered, the experimental behavior emerges.

In the vast and growing literature covering noise in physical and, more recently, biological systems, words such as *noise*, *external noise*, *internal noise*, *fluctuations*, have been applied to processes of different origin. In order to avoid misunderstandings, we will specify here our use of these words. We differentiate between three different sources of noise: (i) instrumental, (ii) external noise, (iii) internal noise (of course, a larger classification is possible [125]).

Instrumental noise is the noise intrinsically associated with the measurement procedure.

External noise depends on how the system interacts with the rest of the world. An idealization of a physical system, needed for modeling, takes place through the precise identification of its boundaries, and every system is coupled with whatever there is outside these boundaries. In mathematical modeling, this type of noise is usually introduced by simply adding noise to the deterministic equations. For the specific case of the Min-system, sources of external noise can, for example, be the intracellular environment or the gene expression of proteins [44] that give rise to fluctuations in the protein numbers.

Internal noise, which is the kind of noise we focus on in this work, does not have an external origin. By internal noise we refer to the molecular composition of real physical systems that are otherwise described by coarse grained equations. The associated macrovariables, which are protein densities in the deterministic equations, represent a sort of averaging over an underlying microscopic description. Consequently, intrinsic fluctuations of molecular origin are associated with each macrovariable.

There are several approaches to studying intrinsic fluctuations. In traditional statistical physics, fluctuations are of thermal origin, giving rise to small departures from a mean value. They go to zero as one approaches the thermodynamic limit. Near equilibrium, the Onsager theory can be used, and the fluctuation-dissipation relation, which connects the strength of the fluctuations to the magnitude of associated dissipative parameters, is valid.

---

[4]MinD is localized in tight clusters which randomly appear and disappear at a minute timescale [80].

Far from equilibrium, these tools are not available. Instead, the system can be described by the probability of being in a certain state. The dynamics of the probability distribution is given by the master equation [126]. A direct integration of the master equation is, in general, impossible, and different methods of analysis have to be developed, *e.g.* the so called Gillespie method[5] [128]. Nevertheless, most of these methods, including Gillespie method, do not work when space is taken into account[6].

Here, we perform computer simulations of a particle based description, where the probability for each event is calculated according to the corresponding probability in the master equation. Stochastic simulations are compared with deterministic simulations and experimental data from LSCM. We compare, numerically and experimentally, the contribution to the large spreading of the values of the period at a fixed length that result from cell to cell variability with the contribution resulting from the internal noise in single cells. In the last five years, the importance of going from cell population measurements to single cell measurements has become more and more obvious, for instance in the context of gene regulation [44]. The final goal, in our case, is to expose the true dependence of the oscillation period as a function of the length of a single cell as opposed to the cell population measurement in figure 2.14.

A general aspect that we want to emphasize is the ability of nonlinear systems to sustain organized behavior even in the presence of a substantial amount of fluctuations [115]. In this context, noise need not only be a nuisance that destroys the desired behavior of a system, but might lead to a behavior that is absent in the deterministic limit. An example for the Min-system are "fluctuation driven instabilities" that were found for the model introduced in [120].

Finally, in order to bridge the gap between our microscopic description and the deterministic one used in chapter two, Langevin equations (LEs) for the fluctuating protein densities will be derived through coarse graining of the microscopic master equation. The deterministic limit of these LEs corresponds to equations (3.2.3) and (3.2.4).

In the last 20 years, we have seen a growing interest in stochastic phenomena in the context of nonlinear dynamics and instabilities away from equilibrium. A LE describes microscopic stochastic dynamics in terms of a deterministic and a noise part. This description was studied in the last decade under different circumstances, from the kinetic

---

[5]The Gillespie method was previously introduced in the context of the Ising spin system by Bortz *et al.* [127].

[6]The Gillespie method automatically sets up the time step, generating directly the time when each single event occurs. The application of this method to spatially extended systems requires modifications which does not make it an advantageous method in that case (François Nédélec "Microtubule functions: Three examples of modeling using simulations" course at summer school "Physics of Cellular Objects", Cargèse 2006).

theory of adsorbates [129–141] to the study of the exchange market [142] and turbulent cascades [143]. However, to our knowledge, there are no applications of that approach to spatially extended biological systems. In the kinetic theory of adsorbates, lateral interactions between adsorbed molecules play a key role in determining the process of pattern formation at nanoscales on metal surfaces similar to the role played by the interaction between MinD proteins in our model.

4.1   Analysis of the master equation

Here, we introduce a particle-based description of the Min-protein dynamics based on the same processes used in the deterministic description. The fluctuation effects are fully incorporated into the model by discrete particles. The starting point is a 1-D microscopic lattice model with lattice length l_0, N total number of sites and Ω sites per unit length. Each site can either be empty or occupied by a single protein MinD or a complex MinDE, i.e. the multiple occupation of a site is not permitted. The master equation for the multidimensional distribution $p(\{n_{d,1}, \ldots, n_{d,N}\}, \{n_{de,1}, \ldots, n_{de,N}\}, t)$, which gives the probability of finding $n_{d,1}, \ldots, n_{d,N}$ and $n_{de,1}, \ldots, n_{de,N}$ proteins MinD or MinDE, respectively, in the boxes positioned at $x_1, \ldots, x_N$ at the time t is given in equation (F.0.5). We first carried out lattice simulations where the probability of each event is calculated according to the corresponding probability in this master equation. Since such a single site description is numerically too expensive, the lattice was soon after coarsely grained, i. e, the entire lattice was divided in m boxes. Moreover, due to the finite resolution of the instruments, coarse graining allowed for a better comparison with the experimental data. This situation correspond to the master equation for the multidimensional distribution $P(n_{d,1} \ldots n_{d,m}, n_{de,1} \ldots n_{de,m}, t)$ shown in equation (F.0.11) (appendix F). Now, each box can be occupied by a maximum number $n_{\max}$ of proteins and has a length l_b much smaller than the characteristic length of the spatial patterns which appear. This length characterizes the resolution of our system. Complete diffusional mixing is assumed to take place inside each box so that single proteins cannot be distinguished inside a box. We define the rates $\tilde{\omega}_{D,E} = \omega_{D,E} c_{\max}$, where $\omega_{D,E}$ are the parameters introduced in equations (3.2.3) and (3.2.4), and to simplify the notations in the following the "tilde" will be

dropped. For each box j the probability P of attachment in a time step Δt is given by

$$P_{D \to d} = \Delta t\, \omega_D \left(\frac{N_D}{m} \right) \left(1 - \frac{n_{d,j} + n_{de,j}}{n_{\max}} \right) \tag{4.1.1}$$

$$P_{E \to de} = \Delta t\, \omega_E \left(\frac{N_E}{m} \right) \frac{n_{d,j}}{n_{\max}} \tag{4.1.2}$$

for MinD and MinE respectively, and

$$P_{de \to E+D} = \Delta t\, \omega_{de} n_{de,j} \tag{4.1.3}$$

for the detachment process of MinDE. The variables $n_{d,j}$ and $n_{de,j}$, are, respectively, the number of MinD and MinDE proteins in each box j. The parameters N_D and N_E are the total numbers of cytosolic MinD and MinE proteins, respectively. Their values are updated at every time step. At each time step, the probabilities of a transition between the neighboring boxes of the MinD proteins, $P(j \to j \pm 1)$, are proportional to the number $n_{d,j}$ of proteins in the jth box and to the fraction $1 - (n_{d,j\pm1} - n_{de,j\pm1})/n_{\max}$ of empty sites in the neighboring box. Moreover, it depends on the interaction between membrane-bound proteins, and according to the Metropolis dynamics we write:

$$P_{j \to j\pm1} = \left(\frac{D_d\, \Delta t}{l_b^2} \right) n_{d,j} \left(1 - \frac{n_{d,j\pm1} + n_{de,j\pm1}}{n_{\max}} \right) I_{j \to j\pm1} \tag{4.1.4}$$

where

$$I_{j \to j\pm1} = \begin{cases} 1 & \text{if } \Delta E_j < 0 \\ exp\left(\dfrac{-\Delta E_j}{k_B T} \right) & \text{if } \Delta E_j > 0, \end{cases} \tag{4.1.5}$$

with $\Delta E_j = V_{j\pm1} - V_j$. The potential $V(x)$, describes the interaction between Min-proteins on the membrane. Concerning the shape of V_j, we chose a square hole potential:

$$V(j) = - \left[\sum_{j=-R_d}^{R_d} \tilde{g}_d n_{d,j} - \sum_{j=-R_{de}}^{R_{de}} \tilde{g}_{de} n_{de,j} \right] \tag{4.1.6}$$

where R_d and R_{de} are the number of boxes over which the sum is taken and which correspond to the interaction ranges, $r_d \simeq l_0 \times R_d$ and $r_{de} \simeq l_0 \times R_{de}$. The parameters $\tilde{g}_d$ and $\tilde{g}_{de}$ are the "coarsely grained" (renormalized) interaction strengths:

$$\tilde{g}_d \simeq \frac{g_d}{2 \sum_{j=-R_d}^{R_d} n_{\max}}; \quad \tilde{g}_{de} \simeq \frac{g_{de}}{2 \sum_{j=-R_{de}}^{R_{de}} n_{\max}} \tag{4.1.7}$$

We controlled that for a fixed interaction range and strength, different shapes for V_j would lead to similar results.

4.1.1   Simulations

In our stochastic simulations, we use a time step $\Delta t = 1/(P_{\max}\omega_E)$, where $P_{\max}$ is the maximum possible value for the sum of all probabilities, typically, $\Delta t = 5 \times 10^{-5}s$. The box length is $l_b = 0.033\mu$m, so that 60 boxes model a 2μm bacterium. The number of sites in each box is $n_{\max} = 33$, corresponding to $c_{\max} \simeq 1000/\mu$m. We use $D_d = 0.15\mu\mathrm{m}^2 s^{-1}$, $g_d = 30k_BT$, $g_{de} = -20k_BT$, $r_d = 800nm$, $r_{de} = 22nm$ $\omega_D = 0.04s^{-1}$, $\omega_E = 0.3s^{-1}$, and $\omega_{de} = 0.04s^{-1}$. For each box j the probability for each possible event is calculated at every time step Δt and then the occupancies for all boxes are simultaneously updated. We recorded the number of particles in each box, after a number s of time steps such that $\Delta t \times s \gg \tau_d$, where $\tau_d = l_b^2/D_d$ is the mixing time due to pure diffusion on the membrane. The value used for D_d is the same we found experimentally (see table 2.1). An estimation of $c_{\max}$, g_d, g_{de}, r_d and r_{de} is given in appendix H, the values of r_d and r_{de} will be also discussed in section 4.3, and the values of the rate ω_D, ω_E and ω_{de} are compatible with the residence times we found experimentally (see table 2.2).

4.1.2   Macroscopic limit

Numerically, the macroscopic limit can be approached in the stochastic simulations by appropriate rescaling some of the parameters. Keeping the value of m fixed we considered the macroscopic limit by sending $n_{\max}$ and N_p to ∞, where N_p is the average total Min-protein density. Then we considered the new rescaled quantities $\tilde{n}_{\max}$ and $\tilde{N}_p$

$$\tilde{n}_{\max} = n_{\max} \times p^{\gamma} \tag{4.1.8}$$

$$\tilde{N}_p = N_p \times p^{\delta} \tag{4.1.9}$$

We found numerically that by choosing γ and δ equal to 1 the deterministic limit is recovered with good approximation. In figure 4.2 the space-time plots for the total MinD concentrations for four different values of p are shown. We want to point out that this is not the macroscopic mathematical limit (see section 4.2.2) where the box size l_b goes to zero, difficult to obtain numerically. Its consistency is supported by the simulations.
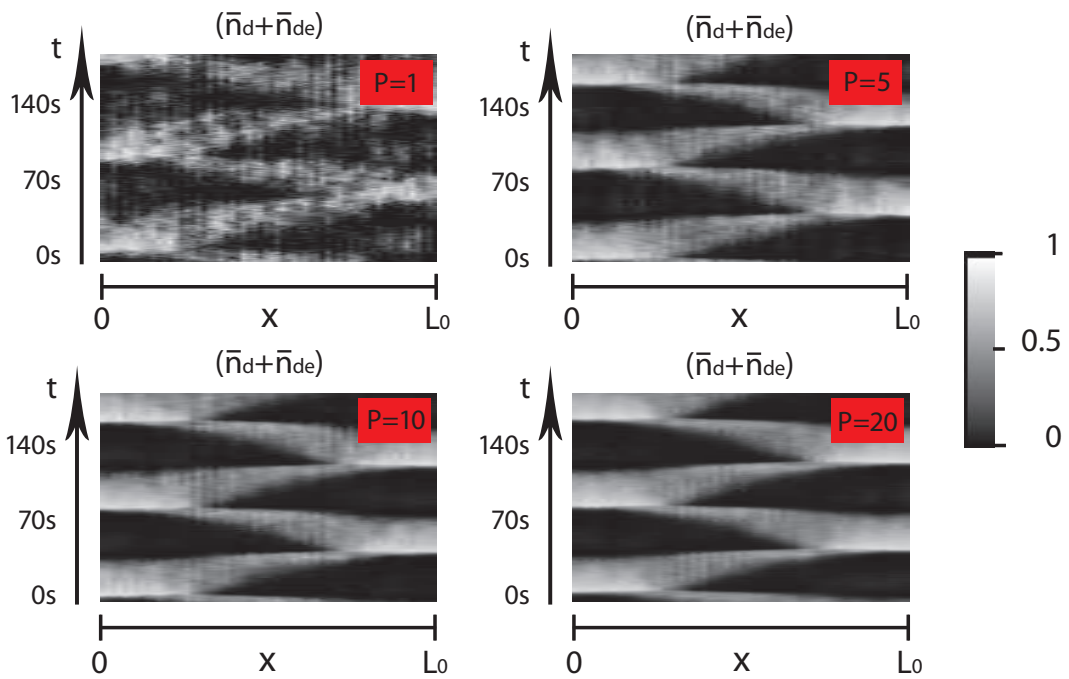
Figure 4.2: Macroscopic limit of microscopic simulations. Space-time plots of the total MinD and MinDE distributions on the membrane, for system size $L_0 = 2\mu$m, and for different values of the rescaling parameter: $p = 1$, $p = 5$, $p = 10$, and $p = 20$. For all values of p, the distributions show pole-to-pole oscillations with a temporal period of approx. 70s. Increasing p the particle distribution approaches the continuum limit.
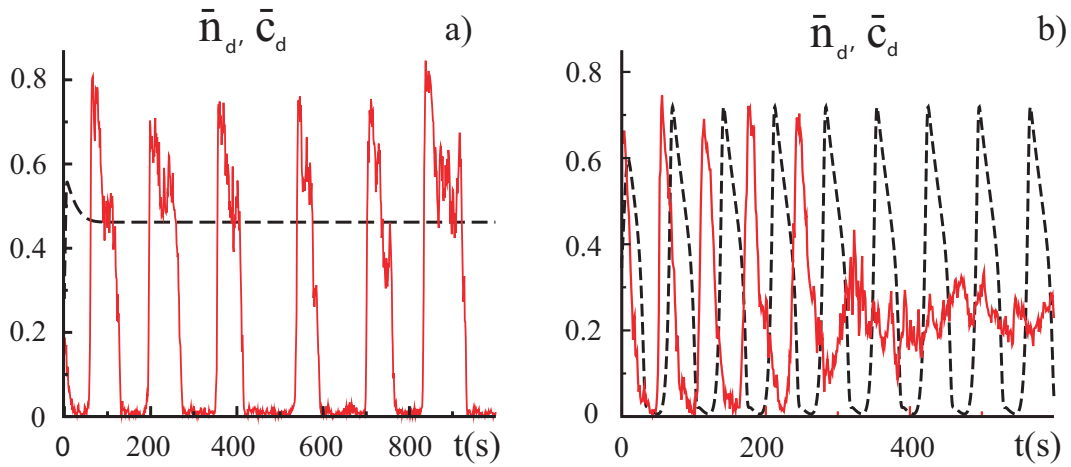
Figure 4.3: Simulations. Local MinD concentration as function of time. Full red lines: stochastic dynamics, $\bar{n}_d = n_d/n_{\max}$ at site $i = 1$. Dashed lines: deterministic dynamics with equivalent parameters, $\bar{c}_d(0) = c_d(0)/c_{\max}$. (a) $D = 360\mu\mathrm{m}^{-1}$ and $E = 134\mu\mathrm{m}^{-1}$, (b) $D = 945\mu\mathrm{m}^{-1}$ and $E = 368\mu\mathrm{m}^{-1}$. $D/E \simeq 2.6$ in both cases. System length 2μm.

4.1.3   Fluctuation-driven instability

To study the effects of stochasticity in our model, we changed the average total protein concentration N_p keeping fixed all other parameters. Figure 4.3 compares the deterministic with the stochastic case, at low and high values of N_p. At low values, in the deterministic case (starting from a perturbation of the homogeneous steady state) the protein concentrations rapidly decay to the homogeneous state, whereas regular oscillations continue for the stochastic model, figure 4.3(a). The opposite happened at high total protein concentration, figure 4.3(b). To investigate this issue in more detail, we reported the oscillation period as function of $N_p = \mathcal{D} + \mathcal{E}$, the average total MinD concentration $\mathcal{D}$, and the average total MinE concentration $\mathcal{E}$. The value of the period was calculated by considering the discrete Fourier transform (DFT) as a function of the period and by taking the value corresponding to the maximum of the DFT as the value of the period. For the error of the period, we considered the width at half height of the DFT. The DFT was performed in a time interval of $20min$. We checked that much longer intervals shift the value of the period only by a small fraction of the error. Figure 4.4 shows the oscillation period as a function of N_p. The stochasticity shifts the regime of oscillations to lower values and reduces the range of the values of N_p supporting oscillations. In the stochastic case, oscillations continue to very low concentrations, $N_p \simeq 400\mu\mathrm{m}^{-1}$, and stop around the middle of the deterministic range. The qualitative behavior is maintained, i.e. the period decreases with the amount of the total Min-protein average concentration in both cases, stochastic and deterministic.

Figure 4.4: Dependence of the oscillation period T on the average total Min concentration N_p. Red dots stochastic simulations, black dots deterministic simulations. I) Region of the values of the average total Min concentration N_p where oscillations are possible only in the stochastic case. II) Region of oscillatory solutions for both cases, deterministic and stochastic. III) Region of oscillatory solution only in the deterministic case. IV) Region where oscillatory solutions are not possible. Error bar for the stochastic case are calculated taking the width at half heigh of the discrete Fourier transform (DFT) performed in a time interval of 20min. The system length is 2μm.
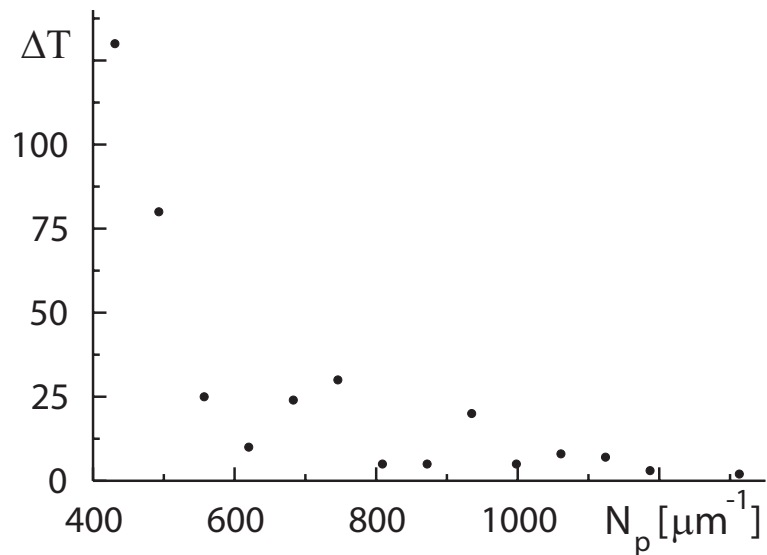
Figure 4.5: Standard deviation of the period, ΔT. as a function of the average total Min-protein density N_p. System length 2μm.
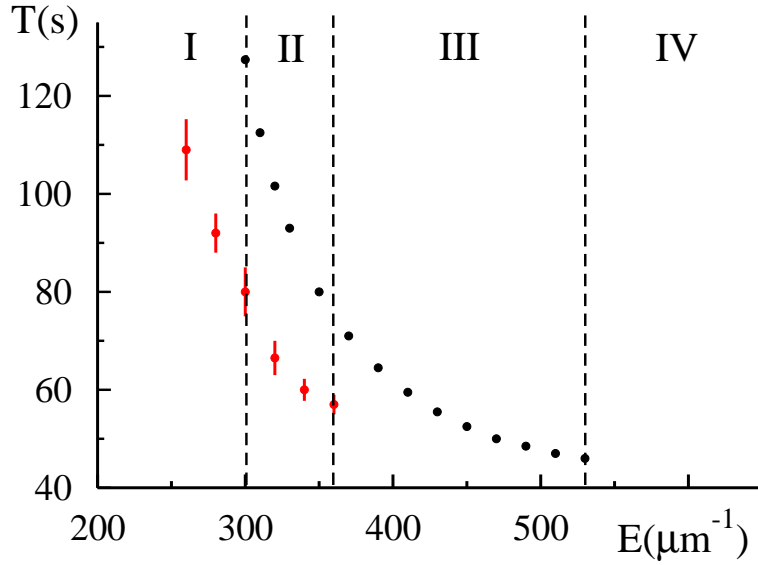
Figure 4.6:   Dependence of the oscillation period T on the average total MinE concentration $\mathcal{E}$. Red dots stochastic simulations, black dots deterministic simulations. I) Region of the values of the average total MinE concentration $\mathcal{E}$ where oscillations are possible only in the stochastic case. II) Region of oscillatory solutions for both cases, deterministic and stochastic. III) Region of oscillatory solution only in the deterministic case. IV) Region where oscillatory solutions are not possible. Error bars for the stochastic case are calculated taking the width at half heigh of the DFT performed on a time interval of 20min. The system length is 2μm.

We also notice that the value of the period itself decreases in the stochastic case compared to the deterministic one. A similar behavior was found for different values of the parameters and different ratios $\mathcal{D}/\mathcal{E}$ (considered in this particular case, data not shown). The standard deviation (SD) of the period, figure 4.5, qualitatively increases at low values of N_p but does not show a regular behavior. At the expected values of N_p in wt cells [110], it oscillates between $5s$ and $30s$. Figure 4.6 shows the oscillation period as a function of the average total MinE density $\mathcal{E}$. Similar considerations, as for the case of the total Min-protein concentration, can be carried out. Furthermore, the range of N_p supporting oscillations is even more reduced. Figure 4.7 shows the oscillation period as a function of the average total MinD density $\mathcal{D}$. In this case, the stochasticity shifts the range of $\mathcal{D}$ values supporting oscillations up to higher values with respect to the deterministic case. The deterministic behavior is qualitatively maintained, i.e. the period initially increases and then decreases slightly with $\mathcal{D}$. However, the stochasticity considerably reduces the variation of T, whose values stay between $60s$ and $80s$.

Figure 4.8 shows the time-averaged total MinD concentration. As opposed to [75] we did not perform the average over the entire cell cycle time of $20min$ but over three periods
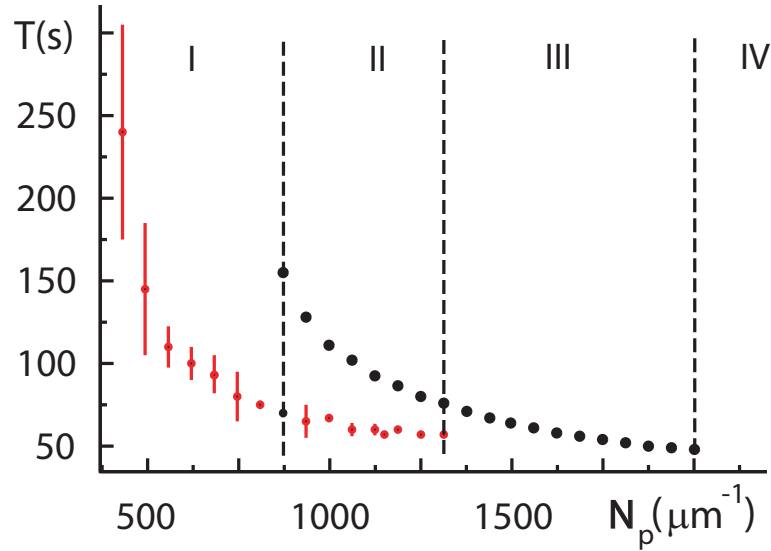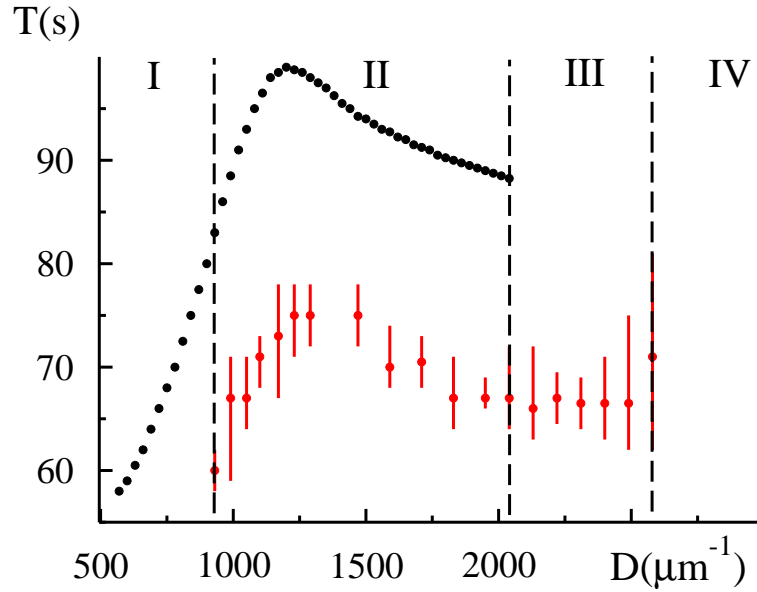
Figure 4.7: Dependence of the oscillation period T on the average total MinD concentration $\mathcal{D}$. Red dots stochastic simulations, black dots deterministic simulations. I) Region of the values of the average total MinD concentration $\mathcal{D}$ where oscillations are possible only in the deterministic case. II) Region of oscillatory solutions for both cases, deterministic and stochastic. III) Region of oscillatory solution only in the stochastic case. IV) Region where oscillatory solutions are not possible. Error bars for the stochastic case are calculated taking the width at half heigh of the DFT performed on a time interval of 20min. The system length is 2μm.

only. In fact, the cell spends only a small fraction of this time on selecting the division site. The figure clearly shows that, lowering N_p, the minimum of the spatial averaged profile becomes deeper and the profile less noisy apparently in contrast to the fact that the local fluctuations increase at low values of N_p. Because the period increases when lowering N_p, this might be due to the fact that the average was carried out for a longer time at a low proteins levels. However, this characteristic is preserved considering average times of $20min$. A possible explanation of this non-intuitive behavior might be the following. At low protein levels and at some time during the oscillations, all proteins accumulate at one pole (roughly within an half period) and then switch almost all together to the opposite pole and stay there during the next semi-period, leaving always one pole and the mid-cell empty and without fluctuations at all. In contrast when the protein levels are increased not all of the proteins switch from one pole to the other during oscillations. In fact, the interaction is not strong enough to aggregate all proteins at one pole, in addition, the maximum value $n_{\max}$ also prevents this possibility. Then, a small number of proteins is alway present at one pole and at the middle of the cell. As a consequence, very strong local
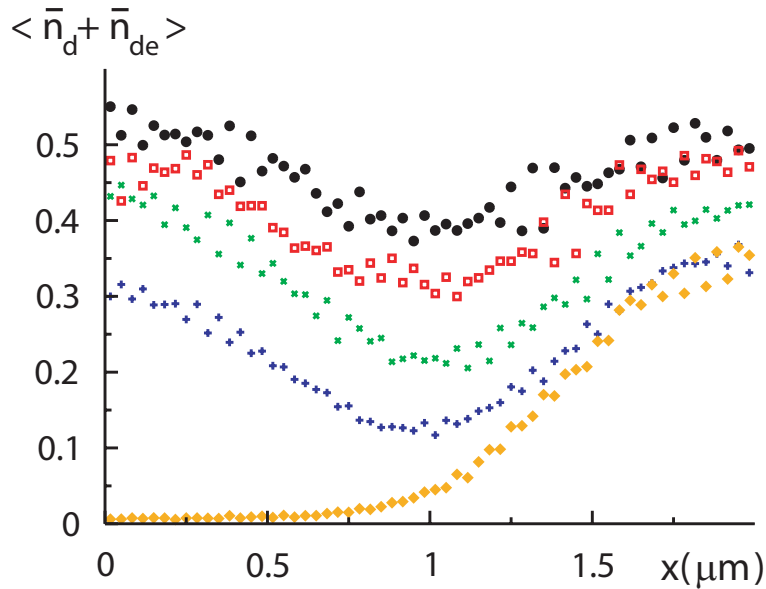
Figure 4.8:   The total MinD distribution averaged over three periods $\langle \bar{n}_d + \bar{n}_{de} \rangle$, for different total protein concentrations N_p. Black dots $N_p = 1187 \mu\text{m}^{-1}$, red squares $N_p = 935 \mu\text{m}^{-1}$, green crosses $N_p = 683 \mu\text{m}^{-1}$, blue pluses $N_p = 431 \mu\text{m}^{-1}$, orange diamonds $N_p = 179 \mu\text{m}^{-1}$. The ratio between the MinD and MinE average total concentrations is $\mathcal{D}/\mathcal{E} \simeq 2.6$.

fluctuations appear that make the time-averaged spatial profile noisier and the minimum in the middle of the cell less pronounced.

Finally, we noticed that for very low protein numbers, $N_p \simeq 180 \mu\text{m}^{-1}$, stationary patterns appear (orange diamonds in figure 4.8). In this case, reducing the value of the interaction range r_d and keeping the same system length, stationary states exist with the maxima at both poles. This indicates that the present model might also apply to the case of the Min-system in *B. subtilis*, where MinD and homologues of MinE are present.

4.1.4   Oscillation period as a function of the cell length

Figure 4.9 shows the oscillation period as a function of the cell length with constant protein density. For the system length at which the oscillation pattern changes in the deterministic case, i.e. around 3μm, the stochastic simulations show two peaks in the DFT, see figure 4.9(c). The intrinsic noise cannot account for the large variations of the oscillation period at approximately fixed length observed in a cell population measurement, see figure 2.14. In fact, the SD is always much smaller than the variation of the period[7], according to the experimental data in single cell measurements (figure 2.5 and

---

[7]Has to be notice that the SD increase if we calculate within a time shorter than $20min$ and if we take the parameter value of p equal to 1 in the simulations.
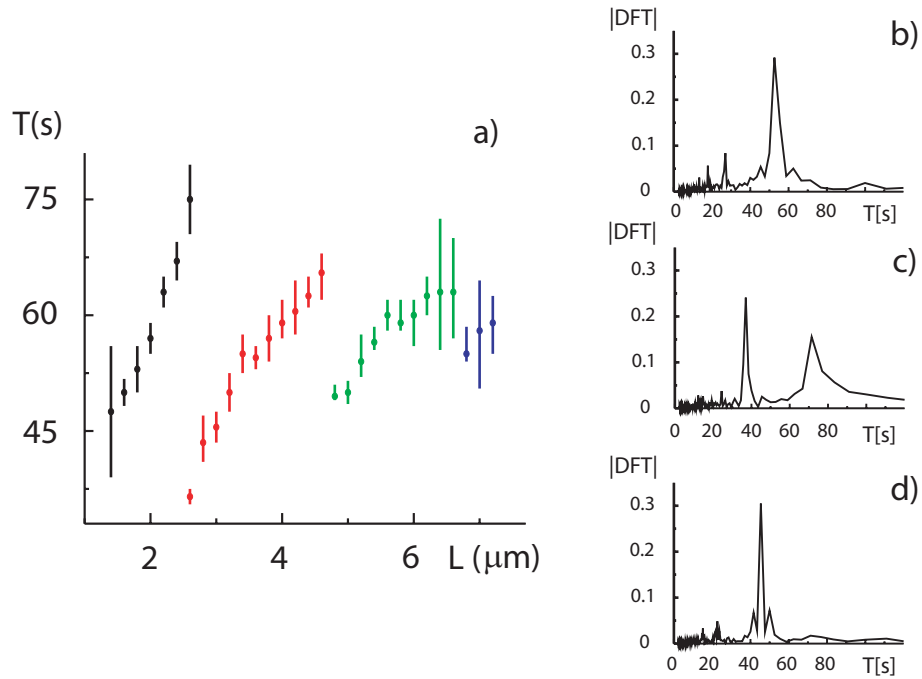
Figure 4.9:   a) Oscillation period of stochastic simulations as a function of the system length. Black dots: oscillation pattern as in figure 4.2, red, green, and blue dots: oscillation pattern with two, three and four stripes, respectively. Error bars are calculated taking the width at half heigh of the DFT performed within a time interval of 20min. b), c), and d) DFT performed on a time interval of 20min, for system length of 1.8μm, 2.6μm, and 3μm, respectively.

data not shown). Figure 4.9 shows the oscillation period as a function of the cell length with constant protein density.

   Figure 4.10 shows the oscillation period of solutions to the deterministic equations (3.2.3) and (3.2.4) as a function of the cell length. For each one of the data points a different value of the protein densities $\mathcal{E}$ and $\mathcal{D}$ was used. In particular, for each kind of spatial pattern (one, two, three and four stripes) the same number of points as in the reported experimental data were considered. Experimentally, typical values of the cell-cell variations in protein concentrations are on the order of ten percent of the mean [144–147]. However, in order to reproduce the experimental data the values of $\mathcal{E}$ and $\mathcal{D}$ were chosen in a larger interval compared to a variation of the ten percent of the mean. Of course, as figure 4.10 shows, with so many free parameters it is possible to reproduce quite well the experimental data. Although the contribution to the large variations of the oscillation period at approximately fixed length that come from cell-cell variations in protein concentrations seems to be higher when compared with the one due to internal noise, our simulations indicate that both of them must be included. Further studies are
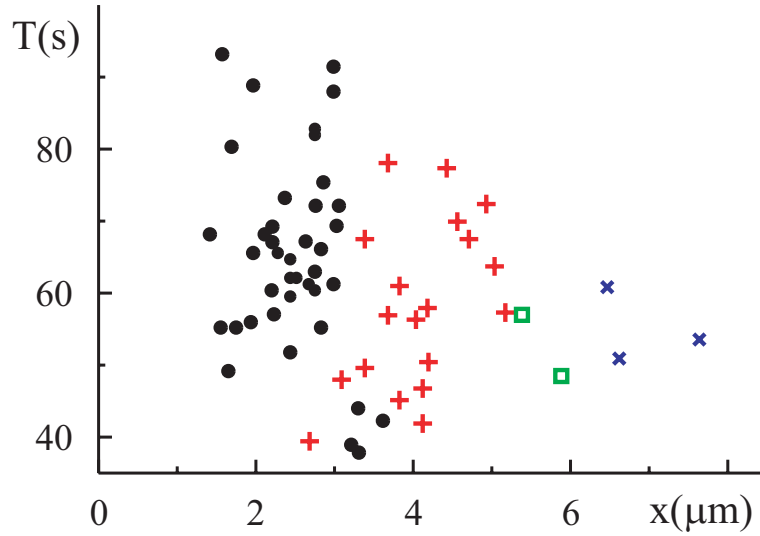
Figure 4.10:   Oscillation period of solutions to the equations (3.2.3) and (3.2.4) as a function of the system length. Black dots: oscillation pattern as in figure 3.3(a), red pluses: oscillation pattern as in figure 3.3(b), green squares and blue Xs: oscillation pattern with three and four stripes, respectively. For each point different values of $\mathcal{E}$ and $\mathcal{D}$ were chosen. All the other parameters values are as in figure 3.3(a).

necessary in order to quantitatively specify this point. Finally, numerically we found (data not shown) that the period T and its standard deviation (SD) increase and decrease, respectively, with D_d.

4.2   Langevin equation

In 1954 it was pointed out by D. K. C. MacDonald that for nonlinear equations the addition of a Langevin force is inconsistent [148, 149]. One cannot add indiscriminately a Langevin term to a macroscopic equation when that equation is not linear. This was forcefully expressed by the question: Does a diode rectify its own fluctuations? This situation gave rise to some discussion, involving the notorious Itô-Stratonovich dilemma; for literature see reference [126]. The conclusion was that it is necessary to start from a more fundamental level which includes the physical cause and the actual form of the noise. This episode, however, was soon forgotten in favor of the so convenient Langevin device.

Niko van Kampen [150]

In the previous section we analyzed through MonteCarlo simulations the processes considered in the deterministic model. These stochastic simulations correspond to the coarsely grained master equation (F.0.11) derived in appendix F. In appendix F, starting from a microscopic master equation (F.0.5), we derived, through coarse graining, a functional Fokker-Planck equation (FPE), and the associated LEs for the protein densities c_d and c_{de}. The deterministic limit of these LEs corresponds to the equations (3.2.3) and (3.2.4). This correspondence (obtained analytically) allowed us to compare the stochastic simulations performed in the previous section with the deterministic ones shown in chapter three. Below, after a short general introduction to the LE, the LEs for the membrane-bound protein concentrations in the case of the homogeneous cytosolic distribution will be presented, and an outline of the procedure used for the derivation of these equations will be given. In particular, we will analyze the hypothesis used and discuss the space and time scales involved. Furthermore, the expression of the current j_d used in the equations (3.2.3) and (3.2.4) will be derived starting from the expression (F.0.28) obtained in appendix F, and, in this way, the phenomenological parameters k_1, k_2, $\bar{k}_1$ and $\bar{k}_2$ in the equations (3.2.3) and (3.2.4) will be linked with the microscopic quantities used for the microscopic simulations in the previous section.

A stochastic differential equation (SDE) in the case in which the noise term appears linearly, is a Langevin equation. Let us see what this means precisely. A SDE is a differential equation which contains a stochastic process $\hat{\xi}(t)$[8]:

$$\frac{d\hat{c}(t)}{dt} = G(\hat{c}(t), t, \hat{\xi}(t)) \quad , \tag{4.2.1}$$

where G depend on three variables. $\hat{\xi}(t)$ is a stochastic process: a family of functions $\xi_u(t)$ depending on the outcome u of an experiment (for example a numerical experiment) S. As a consequence, as SDE is not a single differential equation but rather a family of ordinary differential equations:

$$\frac{dc_u(t)}{dt} = G(c_u(t), t, \xi_u(t)) \quad . \tag{4.2.2}$$

Therefore, the family of solutions $c_u(t)$ of these differential equations, constitutes a stochastic process $\hat{c}(t)$. To "solve" a SDE means to completely characterize the stochastic process $\hat{c}(t)$, i.e. to give the m-times probability density function $p(c_1, ..., c_m; t_1, .., t_m)$, which, in general, is quite a difficult task.

---

[8]See [151] for a short introduction to stochastic processes from a physical point of view.

When the stochastic process $\hat{\xi}(t)$ appears linearly one speaks of a Langevin equation, which has the following general shape:

$$\frac{dc(t)}{dt} = f(c, t) + g(c, t)\xi(t) \tag{4.2.3}$$

(from now on, to simplify the notation, the "hat" will be dropped). In the LE, $\xi(t)$ is usually referred to as the "noise" term[9]. If the function $g(c, t)$ has a constant value, the noise is said to be *additive*, otherwise *multiplicative*.

The stochastic integral associated with a SDE with multiplicative noise is not uniquely defined [152]. For instance, when we consider the integral

$$\int_{t}^{t+h} g(c(s))\xi(s)ds \tag{4.2.4}$$

to be computed in the limit $h \to 0$. The unbounded variation of the stochastic process $\xi(t)dt$ leads to a lack of mathematical rigor and gives rise to some problems of interpretation. Among the many interpretations that can be given to this integral, two are frequently used [126, 152]: the Stratonovich interpretation that follows the standard rules of calculus but gives rise to nonintuitive statistical properties of the noise terms and the Itô interpretation that avoids this problem, at the expense of requiring new rules of calculus. Here, we are not interested in the mathematical definitions of these two interpretations [126, 152][10], but only in what they differ concerning possible applications to our study. The rule that links the two interpretations is the following. Considering a white noise, i.e. a stochastic process ξ_w, satisfying the correlations

$$\langle \xi_w(t) \rangle = 0 \quad , \tag{4.2.5}$$

$$\langle \xi_w(t_1)\xi_w(t_2) \rangle = \delta(t_1 - t_2) \quad , \tag{4.2.6}$$

the SDE

$$\frac{dc(t)}{dt} = f(c) + g(c)\xi_w(t) \tag{4.2.7}$$

in the Itô sense is equivalent to the SDE

$$\frac{dc(t)}{dt} = f(c) + \frac{1}{2}g(c)\frac{\partial g(c)}{\partial c} + g(c)\xi_w(t) \tag{4.2.8}$$

---

[9]The word "noise" comes from the random "noise" one can actually hear in electric circuits

[10]See also reference [153] for a brief introduction to Itô calculus (pages 40-41 contain a compact definition of Itô and Stratonovich stochastic integral), and reference [154] for more mathematical details.

in the Stratonovich sense. Both interpretations coincide for the additive case. Thus, given a stochastic equation with multiplicative noise, as is the case here, the result depends on the interpretation, and a preliminary analysis of the physical problem has to be performed to make an appropriate choice [155]. In any physical process, there is a finite correlation time τ for the noise variables. The Stratonovich prescription for white noise gives us the result one would get for a time-correlated noise in the limit of vanishing correlation time. In our case, we are considering internal noise which is simple due to the fact the number of proteins is finite. We assume that the noise is genuinely uncorrelated even for the closest time moments, and therefore we consider the Itô interpretation. We notice that this assumption cannot be made in the context of cooperative attachment process and that also in our case is an approximation. In fact because of the maximum possible coverage for the proteins on membrane, the probability of an attachment event in the same spatial point is modified by a previous attachment process.

In the case of homogenous cytosolic distributions, as was shown in the previous section, the effects of noise are negligible for the cytosolic concentrations that fluctuate around an average value. In fact, there is no interaction between the proteins in the cytosol that can create confined agglomerations of proteins, and local fluctuations are immediately quenched by fast diffusion. In the following, we will neglect these fluctuations, assuming a constant uniform value for the protein concentrations in the cytosol. In appendix G, we will derive the LEs for the case of the 0-dimensional system and will explicitly show, in this particular case, how the amplitude of the relative fluctuations in the cytosol is small when compared to the ones on the membrane (the absolute values of the fluctuations associated with each one of the reaction processes are exactly the same, as a simple consequence of the conservation of the protein number).

The deterministic equations (3.2.3) and (3.2.4) in chapter three can be seen as the deterministic limit of the following Langevin equation (derived in appendix F) for the fluctuating proteins density c_d and c_{de}:

$$\partial_t c_d = \omega_D C_D (1 - c_d - c_{de}) - \omega_E C_E c_d - \partial_x j_d$$

$$+ \, \xi_d(x,t) \quad , \tag{4.2.9}$$

$$\partial_t c_{de} = -\omega_{de} c_{de} + \omega_E C_E c_d + \xi_{de}(x,t) \quad , \tag{4.2.10}$$

where now the protein concentrations are dimensionless fluctuating fields $c_{d,de}(r,t)$, defined as $c_{d,de} = \tilde{c}_{d,de}/c_{\max}$, where $\tilde{c}_{d,de}$ are the protein densities of equations (3.2.3) and (3.2.4). All the other symbols in the deterministic part have the same meaning as in equations (3.2.3) and (3.2.4), included the current term j_d. However, now the current j_d is

expressed in term of microscopic quantities that can be directly linked to the phenomeno-logical parameters k_1, k_2, $\bar{k}_1$ and $\bar{k}_2$ used in the deterministic description. A detailed analysis of the current j_d is carried out in section 4.2.2. The noise terms $\xi_d(r, t)$ and $\xi_{de}(r, t)$ take into account internal fluctuations of attachment, detachment, and transport processes, and have the form

$$\xi_d(x, t) = \Omega^{1/2} \sqrt{\omega_D C_D (1 - c_d - c_{de})} \alpha_D(x, t) +$$

$$+\Omega^{1/2} \sqrt{\omega_{de} C_E c_d} \alpha_E(x, t) + \qquad\qquad (4.2.11)$$

$$+\Omega^{1/2} \partial_x (\sqrt{2 D_d c_d (1 - c_d - c_{de})} \beta(x, t)) \quad,$$

$$\xi_{de}(x, t) = \Omega^{1/2} \left(\sqrt{\omega_{de} c_{de}} \alpha_{de}(x, t) - \sqrt{\omega_E C_E c_d} \alpha_E(x, t) \right) \quad, \qquad (4.2.12)$$

where $\alpha_D(x, t)$, $\alpha_E(x, t)$, $\alpha_{de}(x, t)$, associated with attachment and detachment processes, and $\beta(x, t)$, associated with transport processes, are independent white noises of unit intensity:

$$\langle \alpha_i(x, t) \alpha_i(x', t') \rangle = \delta(x - x') \delta(t - t') \quad, \quad i = D, E, de$$

$$\langle \beta(x, t) \beta_d(x', t') \rangle = \delta(x - x') \delta(t - t') \quad,$$

$$\qquad\qquad (4.2.13)$$

$$\langle \alpha_i(x, t) \alpha_j(x', t') \rangle = 0, \quad for \quad i \neq j \quad,$$

$$\langle \beta(x, t) \alpha_i(x', t') \rangle = 0 \quad.$$

The prefactor of the noise variables α's and β, reflect that the noise strength depends on the number of free binding sites and possible binding molecules. Their can be derived from the N sites lattice model introduced before. Let L be the length of the system. Then the parameter $\Omega = L/N$, which goes to zero in the deterministic limit ($N_p \to \infty$, $N \to \infty$), specifies the number of lattice sites per unit length. The noise terms associated with the cytosolic distributions is $\Omega_{\text{cyt}} = L/N_{\text{cyt}}$, where N_{cyt} is the number of available sites in the cytosol (see appendix G). Assuming $N_{\text{cyt}} \gg N$, the relative fluctuations of the cytosolic protein concentrations can be neglected when they are compared with the relative fluctuations of the membrane-bound protein concentrations. The internal noise of reactions and diffusion is multiplicative. It is proportional to the square root of the local protein concentrations in such a way that the noise terms are directly linked to the

deterministic part. It was pointed out a long time ago by van Kampen that noise in a *jump* Markov process "is inherent in the very mechanism by which the state of the system evolves and cannot be divorced from its equations of motion"[11].

The LEs allow for estimating the relative contribution of different physical processes to the noise, namely attachment and detachment processes and transport processes, as well as their role for the behavior of the dynamics.

The integration of LEs with multiplicative noise as in equations (4.2.9) and (4.2.10) has to be performed carefully. In fact, standard schemes give rise to unphysical negative values for the protein concentrations $c(x, t)$ [156–158].

4.2.1 Reaction processes

In this section, we consider the simple case of the 0-dimensional system. Thus, only the reaction processes have to be taken into account. We would like to give an impression of the derivation of the LEs (4.2.9) and (4.2.10), and show in detail some of the hypotheses behind this derivation. The next section, where the spatial extension of the system will be taken into account, was written from a similar motivation. A mathematical derivation of the LEs (4.2.9) and (4.2.10) is given in appendix F.

Let us consider the following reactions [12]

$$
\begin{array}{rcll}
D & \longrightarrow & d & (\omega_D) \quad , \\
E + d & \longrightarrow & de & (\omega_E) \quad , \\
de & \longrightarrow & E + D & (\omega_{de}) \quad ,
\end{array}
\tag{4.2.14}
$$
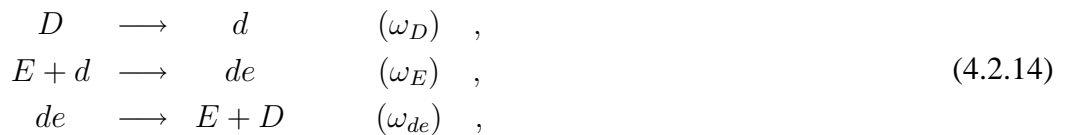
where D and E represent cytosolic MinD and MinE molecules, d and e membrane-bound MinD and MinE molecules, respectively, and ω_D, ω_E and ω_{de} are the associated rates. Each one of these reactions takes place only in one direction, thus breaking the detailed balance.

For the sake of simplicity, here, we consider only the membrane-bound proteins as variables. In appendix G we show that the LEs associated with these variables do not change when the cytosolic protein concentrations are also considered as variables.

We can write the total number of MinD, N_D, and MinE, N_E of the stationary uniform state in the cytosol in terms of the stationary uniform state values of MinD, n_d^0 and MinDE,

---

[11]See the 1981 edition of reference [126], p. 247.

[12]In wild-type cells, MinE is likely to be active as a dimer [105], therefore the second reaction is $2E + d \longrightarrow de$, and the third is $de \longrightarrow 2E + D$. Here, the symbols E and e refer to these dimers.

n_{de}^0, on the membrane

$$N_D = N_D^{\text{tot}} - n_d^0 - n_{de}^0 \quad ,$$
$$N_E = N_E^{\text{tot}} - n_{de}^0 \quad ,$$
(4.2.15)

where N_D^{tot}, and N_E^{tot} , are the total MinD and MinE proteins, respectively. Let us consider the first reaction in (4.2.14). It can be interpreted as the generation of a single membrane-bound MinD molecule at an average rate of

$$\omega_D N_D \Big(1 - \frac{n_d + n_{de}}{N} \Big) \quad ,$$
(4.2.16)

proteins per unit time. In this case, the number of sites N corresponds to the maximum number of Min proteins allowed to be membrane-bound, therefore the last term is the fraction of cytosolic proteins MinD that can be converted to membrane-bound MinD. ω_D is the attachment rate of a single MinD protein. Assuming that all of the other reactions are quenched, the probability $p(n_d, t)$ of finding n_d MinD proteins at a time t satisfies the following master equation [126, 152, 159]:

$$\frac{dp}{dt} = -\omega_D N_D \Big(1 - \frac{n_d + n_{de}}{N} \Big) p(n_d, t) +$$
$$+\omega_D N_D \Big(1 - \frac{n_d - 1 + n_{de}}{N} \Big) p(n_d - 1, t) \quad ,$$
(4.2.17)

where $\sum_{n_d} p(n_d, t) = 1$ at any time t, with $n_d = 0, \ldots, N$ and $p(n_d - 1, t) = 0$ when $n_d = 0$. In order to consider the probability density $p(c_d) = \frac{1}{N} p(n_d)$, we introduced the quantities $c_d = n_d/N$ and $c_{de} = n_{de}/N$. Taking into account that these quantities change only a little as a result of an attachment event, we can write

$$p(c_d - 1/N) \approx p(c_d) - N^{-1} \frac{\partial p}{\partial c_d} + \frac{1}{2} N^{-2} \frac{\partial^2 p}{\partial c_d^2} + O(\frac{1}{N^3}) \quad .$$
(4.2.18)

Remark

We want to stress that this is not the usual procedure adopted in similar situations. In fact, we would say 'as a rule', the previous expansion is typically carried out in respect to the number of actual particles (the so called van Kampen Ω-expansion) and not in respect to the number of 'possible' particles. This would not be possible in our case, in fact, a priori, the number of proteins n_d can also be zero at some moment in time, even when the total number of MinD proteins is extremely high. This cause the fluctuations

to be so large that the Ω-expansion breaks down. This point will be become clearer in the next section, where the case of the spatially extended system will be considered. This approach has as a consequence that one of the key parameters of our model, the parameter $c_{\max} = n_{\max}/N$ (here dimensionless) goes into the noise prefactor Ω. It turns out that the amplitude of the noise is in part fixed by the value of this parameter. In particular, the noise terms vanish when $c_{\max} \rightarrow \infty$. When this limit is applied to the deterministic equations, the oscillations are lost. The other standard features of the LE, like the noise amplitude equal the square root of the deterministic term, are preserved.

Let us continue with our derivation of the LE. For smooth distributions $p(c_d)$ the terms with higher derivatives in expansion (4.2.18) can be ignored. Substituting the approximation (4.2.18) into (4.2.17) and retaining the terms up to the order $1/N$, we obtain the following Fokker-Planck equation [160, 161]

$$\partial_t p = -\frac{\partial}{\partial c_d}(f_D p) + \frac{1}{2}N^{-1}\frac{\partial^2}{\partial c_d^2}(f_D p) \quad , \tag{4.2.19}$$

where

$$f_D = \omega_D \left(\frac{N_D}{N}\right)(1 - c_d - c_{de}) \quad , \tag{4.2.20}$$

As follows from the theory of random processes [126, 152, 159], this Fokker-Planck equation is equivalent to the stochastic differential equation

$$\frac{d}{dt}c_d = f_D + \frac{1}{\sqrt{N}}[\sqrt{f_D}\alpha_D(t)] \quad , \tag{4.2.21}$$

where $\alpha_D(t)$, is an independent white noise of unity intensity

$$\langle \alpha_D(t)\alpha_D(t')\rangle = \delta(t - t') \quad . \tag{4.2.22}$$

Now, we will consider the second reaction in (4.2.14). Following the above derivation, we write the stochastic differential equations as

$$\frac{d}{dt}c_d = -f_E + \frac{1}{\sqrt{N}}\left[\sqrt{f_E}\alpha_E(t))\right] \quad ,$$

$$\tag{4.2.23}$$

$$\frac{d}{dt}c_{de} = f_E - \frac{1}{\sqrt{N}}\left[\sqrt{f_E}\alpha_E(t)\right] \quad ,$$

where

$$f_E = \omega_E \left(\frac{N_E}{N} \right) c_d \quad .$$

(4.2.24)

The noise terms in this equation have to be identical in absolute value and with opposite signs, because each reaction event simultaneously changes the number of proteins of both species. The same procedure can be followed for the last reaction, yielding

$$\frac{d}{dt} c_d = f_D + \frac{1}{\sqrt{N}} \left[\sqrt{f_D} \alpha_D(t) \right] \quad ,$$

$$\frac{d}{dt} c_{de} = -f_{de} + \frac{1}{\sqrt{N}} \left[\sqrt{f_{de}} \alpha_{de}(t) \right] \quad ,$$

(4.2.25)

where

$$f_{de} = \omega_{de} c_{de} \quad .$$

(4.2.26)

In principle, taking into account that our actual system has a finite spatial extension, like we did with the maximum protein number N of membrane-bound proteins, a maximum protein number N_{cyt} for the cytosolic proteins has to be introduced. Thus, the previous expression would take the form

$$f_{de} = \omega_{de} c_{de} \left(1 - \frac{n_D + n_E}{N_{\mathrm{cyt}}} \right) \quad .$$

(4.2.27)

However, a reasonable assumption is that $N_{\mathrm{cyt}} \gg N_D^{\mathrm{tot}}, N_E^{\mathrm{tot}}$, thus

$$\left(1 - \frac{n_D + n_E}{N_{\mathrm{cyt}}} \right) \approx 1 \quad .$$

(4.2.28)

Such an assumption was implicit in the deterministic equations, where only the parameter c_{max} for the membrane-bound protein concentrations was present and its corresponding parameter for the cytosolic protein concentrations was not.

Now, assuming the different noise processes as completely independent,

$$\langle \alpha_i(t) \alpha_j(t') \rangle = 0 \quad \text{when} \quad i \neq j \quad ,$$

(4.2.29)

i.e. each reaction make an independent contribution to the noise terms, the total LEs are given by the sum of each term on the right side of the previous equations. However,

this assumption is only an approximation. In fact, if we consider, for instance, the MinE attachment and hydrolysis processes, some correlation between the two processes would have built up after some temporal interval Δt.

In the deterministic limit ($N \rightarrow \infty$) the noise terms vanish, and the deterministic equations (3.2.3) and (3.2.4) are recovered without spatial degrees of freedom.

4.2.2   Transport processes

Here, the spatial degrees of freedom and the coarse graining procedure are introduced. Then, the space scales involved are analyzed. Finally, the current term j_d introduced in the deterministic equations (3.2.3) and (3.2.4) is considered from a microscopic point of view, starting from the expression (F.0.28).

A 1-dimensional lattice, with lattice length l_0, N total number of sites and total length $L = l_0 N$ is considered. The lattice spacing is assumed $l_0 \approx l_p$, where l_p is the protein size, assumed to be equal for all species. The state of the system is completely defined when the occupation numbers of all protein species on each site are given. The occupancy of site j is $n_{i,j}$, with $i = d, de$ representing membrane-bound MinD and the complex MinDE, respectively. The occupation numbers can only be 1 or 0. Coarse graining consists of dividing the lattice into m boxes of length l_b, each containing a number of sites $n_{\max} > 1$. At the same time, the length l_b has to be smaller in comparison to the minimal characteristic length scale of the spatial pattern. The fraction of occupied sites in box j is introduced as

$$c_j = (\text{number of proteins})_{\text{j}}/(\text{number of sites})_{\text{j}} \quad . \tag{4.2.30}$$

With the above definition, the values of this variables change only a little as a result of an attachment, detachment event or a single diffusion jump. This can be used to transform the associated master equation to a FPE by performing a Taylor expansion up to the second order in $\left[1/(\text{sites number})\right]_{\text{j}}$. Similar to the 0-dimensional case we want to point out that an expansion in term of $\left[1/(\text{particle number})\right]_{\text{j}}$ would not be possible for our specific system, in fact the occupation numbers n_d and n_{de} in each box can also be zero at some moment in time during the oscillations.

Furthermore, complete diffusional mixing is assumed to take place inside every box. This means that, for a fixed box length l_b, our mesoscopic model is valid only on time scales bigger than $\tau = l_b^2/D$ where D is the smallest diffusion constant in the system. In our case $\tau_d = l_b^2/D_d$. Therefore, because l_b is smaller than the characteristic scale of the spatial pattern, the variables c_j can be regarded as values of a smooth density $c(x)$ taken at
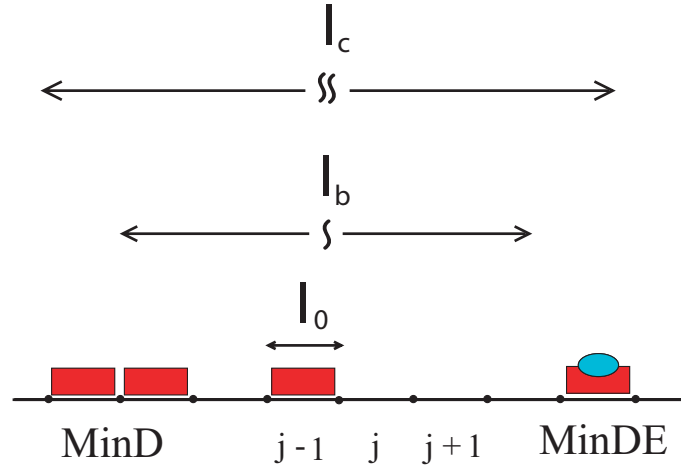
Figure 4.11: In the lower line a possible protein distribution on the membrane is shown. The sites of the lattice are labeled with the index j, l_0 is the lattice size, l_b the box size of the coarse graining procedure, and l_c represent all other lengths related to the spatial distribution of the proteins, with $l_0 < l_b < l_c$.

the discrete coordinates point x_j, and continuum variables can be introduced. Figure 4.11 shows all of the important length scales of the model. The smallest is the lattice length l_0, the microscopic length scales of our system. As concern the length box l_b, we have the freedom to choose the size that allows for a better comparison with the experimental data. Using a metaphoric picture, we can think of the model as a microscope, where the maximum resolution is l_b. The value of l_b must be chosen in such a way as to bring into focus the characteristics of the system which we are interested in. Characteristics of the system with length scales smaller than l_b cannot be brought out, they appear out of focus and only some qualitative aspects can be seen. All other lengths, like the typical length Λ of the pattern or lengths related to quantities that determine the spatial distribution of the proteins, which we want to observe in detail, are represent by l_c. Because inside the space interval l_b and the time interval $\tau_d = l_b^2/D_d$, the system appears homogeneous, all these lengths have to be bigger than l_b and their changes have to be observed over a time scale bigger than τ_d. In conclusion, l_b and τ, are the space and time scales of our model.

Now, we will explicitly consider the transport term. In appendix F the following

general expression for the current is derived:

$$j_d = \left[c_d(1 - c_d - c_{de}) \frac{\partial (V/k_B T)}{\partial \xi} \right] - \frac{\partial c_d}{\partial \xi} \quad , \tag{4.2.31}$$

here, written in dimensionless form (see appendix D). In this way, we can introduce the parameter $l_d = \sqrt{D_d/\omega_E}$, in regard to which we want to specify the limits of validity for the approximation in the expansion of the current j_d to be considered. For simplicity we consider only MinD-MinD interaction that correspond in term of macroscopic parameter to fix $\bar{k}_1 = 0$ and $\bar{k}_2 = 0$. V is a binary attraction potential (with the dimensions of an energy)

$$V(\xi) = - \int u(\xi - \xi') c_d(\xi') d\xi' \tag{4.2.32}$$

between two proteins separated by a distance $x = \xi l_d$ on the membrane and $u(\xi - \xi')$ is significantly different from zero only in a range of $|\xi - \xi'| = r_d/l_d$.

If the membrane concentration $c_d(\xi)$ does not vary significantly within the interaction range, i.e. $\xi_d = r_d/l_d$, the following Taylor expansion can be considered

$$\int u(\xi - \xi') \left[c_d(\xi) + (\xi - \xi') \frac{\partial c_d}{\partial \xi} + \frac{1}{2}(\xi - \xi')^2 \frac{\partial^2 c_d}{\partial \xi^2} + ... \right] d\xi' \quad , \tag{4.2.33}$$

where the spatial derivatives are taken at point ξ and where we assume

$$(\xi - \xi') = r_d/l_d \ll 1, \quad \text{i.e.} \quad r_d \ll l_d \quad . \tag{4.2.34}$$

Therefore, we have

$$\int u(\xi - \xi') c_d(\xi') d\xi' \approx u_0 c_d + \chi \frac{\partial^2 c_d}{\partial \xi^2} \quad , \tag{4.2.35}$$

where the coefficients are

$$u_0 = \int u(\xi) d\xi \quad ,$$

$$\chi = \tfrac{1}{2} \int u(\xi) \xi^2 d\xi \quad , \tag{4.2.36}$$

and we have taken into account that, by symmetry, the second term in the expansion is $\int \xi u(\xi) d\xi = 0$. The coefficients in (4.2.36) can be estimated by an order of magnitude as

$$u_0 \approx U_d \quad , \qquad \chi \approx U_d \, r_d^2 \quad , \tag{4.2.37}$$

where r_d is the interaction length and $U_d \approx u_{\max} r_d$, with $u_{\max}$ the maximal intensity of $u(x)$. Therefore, we can write the local (dependent on a finite number of spatial derivatives) expression for the current:

$$j_d = D_d \Big[1 - \frac{U_d}{k_B T} c_d (1 - c_d - c_{de}) \Big] \frac{\partial c_d}{\partial x} -$$
$$- D_d \frac{U_d \, r_d^2}{k_B T} c_d (1 - c_d - c_{de}) \frac{\partial^3 c_d}{\partial x^3} \quad .$$

(4.2.38)

Comparing this expression with the current term in the deterministic equation (3.2.3) and taking into account that the proteins densities in (4.2.38) were rescaled by $c_{\max}$, we can link the parameters ks to microscopic quantities by

$$k_1 \;\; = \;\; \frac{1}{c_{\max}^2} \frac{D_d}{k_B T} U_d \quad , \tag{4.2.39}$$

$$k_2 \;\; = \;\; \frac{1}{c_{\max}^2} \frac{D_d}{k_B T} U_d r_d^2 \quad , \tag{4.2.40}$$

and analogously for $\bar{k}_1$ and $\bar{k}_2$. We can define an effective diffusion constant

$$D_{\text{eff}}(c_d, c_{de}) = D_d \Big[1 - \frac{U_d}{k_B T} c_d (1 - c_d - c_{de}) \Big] \quad , \tag{4.2.41}$$

and

$$F(c_d, c_{de}) = D_d \, \frac{U_d \, r_d^2}{k_B T} \, c_d \, (1 - c_d - c_{de}) \quad , \tag{4.2.42}$$

thus write the current as

$$j_d = D_{\text{eff}}(c_d, c_{de}) \frac{\partial c_d}{\partial x} - F(c_d, c_{de}) \frac{\partial^3 c_d}{\partial x^3} \quad . \tag{4.2.43}$$

The MinD proteins can move diffusively over the membrane with the effective diffusion constant D_{eff}. Moreover, potential gradients induce a flow of proteins as described by the term $F(c_d, c_{de})$. The coefficient $D_d / k_B T$ represents the mobility of Mind proteins on the membrane determined by the diffusion constant D_d and temperature T. The factor $(1 - c_d - c_{de})$ takes into account that the flow can pass only through vacant sites on the membrane.

We noticed that a new length scale had been introduced, i.e. the interaction range r_d. Coherently with the meaning of our mesoscopic model we assume $r_d > l_b$, and the same

relation must be satisfied by the interaction range r_{de}. The mesoscopic theory is justified in our specific model only if

$$l_0 \ < l_b < r_d, r_{de} < l_d, \Lambda, \tag{4.2.44}$$

where Λ was assumed to be larger or of the same order of l_d. We also noticed that the validity of the mesoscopic description does not depend, for instance, on the number of proteins involved, they can also be zero for all species of proteins, i.e. zero value of smooth densities $c(x)$.

Finally, we can relate the noise prefactor Ω, absent in the deterministic limit, with different parameters. The lattice spacing l_0, the box length l_b and the box site number $n_{\max}$, the system length L and the total site number N, and with the maximum protein density $c_{\max}$,

$$\Omega = l_0 = l_b/n_{\max} = L/N = 1/c_{\max} \quad . \tag{4.2.45}$$

Then, we can imagine different ways for obtaining the deterministic limit, as

$$N_p \to \infty \quad , \qquad l_b \to 0 \quad , \qquad m \to \infty \quad , \qquad l_b m = L \quad \text{fixed,} \tag{4.2.46}$$

or

$$N_p \to \infty, \qquad l_0 \to 0, \qquad N \to \infty, \qquad l_0 N = L \quad \text{fixed.} \tag{4.2.47}$$

In principle, these limits have to be applied to the microscopic simulations considered in the previous paragraph in order to obtain the continuum limit. However, from a practical point of view, verify numerically these limits require a large amount of CPU time. For this reason we chose the less expensive procedure shown in section 4.1.2, where the value of l_b is kept fixed and $n_{\max}$ goes to ∞.

4.3 Discussion

In this chapter we studied the effect of the internal noise due to a finite number of proteins. To this end we performed stochastic simulations based on single particle description. Deriving the LEs for the protein concentrations, we linked this stochastic description with the deterministic one presented in chapter three. Such a link allows us to relate the phenomenological parameters k_1, k_2, $\bar{k}_1$ and $\bar{k}_2$ used in the deterministic description of

the aggregation current j_d with the microscopic parameters, r_d, r_{de}, U_d and U_{de} introduced here.

These relationships are shown in the microscopic equations (4.2.39) and (4.2.40). Assuming that a simple process leads to aggregation based on short-range pair interaction potentials, they are valid whenever r_d and r_{de} are much smaller than the diffusion length $l_d = \sqrt{D_d/\omega_E}$. Taking a diffusion constant of $0.06\mu\mathrm{m}^2/s$ for membrane-bound MinD, which falls well into the regime we measured (see table 2.1), the values of the phenomenological coefficients ks imply values of $35k_BT$ for the interaction strength between membrane-bound MinD and $20k_BT$ between MinD and MinDE complexes. The range for MinD-MinD interactions is then 350nm, and for MinD-MinDE interactions it is 10nm. While all other values are acceptable, the range for MinD-MinD interactions is too large for purely electrostatic interaction. This points to more involved microscopic dynamics of membrane-bound MinD than discussed here.

The effects of the noise in the Min-system will be discussed further in the next conclusive chapter.

Chapter 5

Conclusions and Perspectives

The subject of this research was a quantitative analysis of the Min-protein dynamics in *E. coli*. From a theoretical point of view, we considered a phenomenological deterministic description, where lateral interactions between proteins on the cell membrane play a key role, and in addition we studied the effects of fluctuations using stochastic simulations. Experimentally, we investigated the predictions of the theoretical model and measured some of the model parameters. In particular, we measured the temporal period of the oscillations as a function of the cell length that we found to be compatible with the theoretical prediction. Also, we measured the Min-protein mobilities in the cytoplasm and on the membrane.

What are the implications of our experimental study for understanding the Min-oscillations?

So far, theoretical analysis of the Min-oscillations has been essentially qualitative as no values for the dynamic parameters of the Min-proteins were available. Our FCS measurements of the protein mobility partially filled this gap. Let us recall the distinctive features of the two classes of mechanisms in which we divided all models proposed so far (see also figure 2.3):

- MinD proteins attach cooperatively to the membrane, i.e. preferentially at points where MinD is already bound. We denoted this class of models as Cooperative Attachment Models (CAM).

- Proteins attach to the membrane unbiased, and MinD-aggregates are formed after the proteins have bound to the membrane as a consequence of protein-protein interaction. We denoted this class of models as Aggregation Current Models (ACM).

Our measurements enable us to propose precise experimental conditions in order to compare the two mechanisms. For the diffusion constants of cytosolic Min-proteins, the val-

ues suggested by FRAP measurements of GFP [88] were considered in all of the mathematical models proposed. In these measurements, the diffusion constant of GFP fused to a cytoplasmic maltose binding protein was determined to be $2.5\mu\mathrm{m}^2/s$. The values for the cytosolic MinD diffusion constant that we found is approx. $16\mu\mathrm{m}^2/s$, *i.e.* a factor of 6 higher, and for the cytosolic MinE is about $10\mu\mathrm{m}^2/s$. Therefore, a cytosolic MinD molecule explores the volume of a 4μm long cell within roughly a second. A cytosolic MinE molecule needs about $1.5s$. With a residence time τ of about 300ms of cytosolic MinD, the value of the diffusion constant D implies a diffusion length $l = (D\tau)^{1/2}$ of 2.3μm. For MinE, this value is about 1.8μm. At least for small bacteria of about 2μm in length, these values suggest a rather homogeneous distribution of cytosolic MinD and MinE. Min-oscillations were reported also in short cells just after division [61][1]. CA models do not show oscillations under the condition of homogenous cytosolic protein densities. Thus, a detailed experimental and theoretical analysis of short bacteria might provide a way to put the CA models to a crucial test. Particular attention should be paid to the MinE-ring in these cells. In fact, the analysis of the CA model by Huang et al. [71] suggests the disappearance of the MinE-ring if the diffusion length is increased in comparison to the cell length. The presence of the MinE-ring in short cells might therefore provide information on the mechanism of its formation. Figure 2.7 shows a possible candidate, in fact, the MinE-ring in the low-side indicated by the red arrow belongs to a coming mini-cell (it can be see in the next frames of the corresponding movie) and its length can be estimated as being somewhat larger than 2μm (see scale bar).

The values for the cytosolic diffusion constants also support our assumption of a homogenous cytosolic protein distribution, which allowed for a theoretical description in terms of the concentrations of membrane-bound MinD and MinDE complexes.

Moreover, in order to generate "striped" patterns in long bacteria, the CA model introduced in [71] requires that the exchange of ATP for ADP on cytosolic MinD be not too fast. For the parameters used there [71], the authors found a critical rate of $1/s$. On the other hand, our measured residence time provides a lower limit to the exchange rate of approx. $3.3s^{-1}$ (only after rebinding of ATP, MinD can attach again to the membrane).

The values for the diffusion constants of membrane-bound proteins are about two orders of magnitude smaller than the cytosolic constants. For membrane-bound MinD, it is of the same order as the value we used in our theoretical model [77]. This shows that the mobility of membrane-bound MinD is sufficiently large to allow for an AC mechanism causing the oscillations. It is also compatible with the CA mechanism as shown by Fange and Elf [122].

The measurement of the oscillation period as a function of the cell length (see fig-

---

[1]Figure 2.7 is one single frame of one of our videos showing such behavior.

ure 2.14), carried out on a population of cells, was motivated by calculations using the stochastic and the deterministic model. In the theoretical study, the average total protein densities were fixed and a characteristic dependence of the period on the cell length was found, see figure 3.4 and 4.9.

Experimentally, we did not find a simple relation between period and length. However, the variation of the period in a single-cell measurement at approximately constant length, seen for example in figure 2.5, cannot account for the large variation of values found in cell population measurements, see figure 2.14. This is probably due to cell to cell variations in the protein density. This is also consistent with the small variation of the period found in stochastic simulations at fixed length and average total protein density. Thus, we believe that a measurement in a single cell is able to test the discontinuous dependence of the oscillation period on the system length predicted by our calculations. To this end, we developed the necessary technique for a future experiment. Using an LSCM and keeping the cells at $37°$C, we recorded the oscillations of the fluorescence intensity for more than 30 minutes. At the same time, we observed the cell size increasing by micrometers. Up to now, we have performed only one single measurement of such kind, whose results are shown in figure 2.15, and we are confident that successive measurements will give a more definite result.

A "secondary" result

As a control for the measurement of the Min-protein mobility, we also measured the mobility of the Enhanced Green Fluorescent Protein (EGFP) and found significant deviations from previous measurements. In fact, in [88], using FRAP, it was found that $D_{\mathrm{GFP}} \simeq 7.5 \mu\mathrm{m}^2/s$. There, it was also found that the diffusion constant can be changed significantly by modifying small parts of the protein, e.g. by adding a His-tag. In contrast, using FCS, we found $D_{\mathrm{GFP}} \simeq 18 \mu\mathrm{m}^2/s$, which was compatible with the values we measured for MinD and MinE. Furthermore, compared with the FRAP measurements, our results indicated that a His-tag has a much weaker effect on the diffusion constant of GFP.

What more do we need from the experiments?

A complete experimental verification of our theoretical predictions or, in other words, a complete characterization of the Min system allowing for a theoretical quantitative study, would at least require the knowledge of: (i) the global and local concentration of molecules in individual cells; (ii) the variation of the global concentration among

individual, genetically identical members of the cell population; (iii) whether, and how these quantities vary with time, with the cell length or other quantities of interest; (iv) and, finally, the rates of the individual reactions causing that variation. For instance, during the measurement of the period in a growing cell, it might be interesting to investigate whether the total average protein density stays constant. We experienced the difficulty of such a measurement with LSCM, in which only the measurement of local relative concentrations was possible. Generating methods to achieve this information is one of the greatest challenges for biology in the twenty-first century [162]. Examples of new methods to quantify the protein number inside the cell are given in [163, 164].

A suggested experiment from the theoretical analysis

In the AC model, non-linear terms appear in the current term describing the protein interaction on the membrane; in the CA models they appear in the reaction term, describing the attachment-detachment processes. One possibility for discriminating between the two mechanisms would be to study the dynamics of Min-proteins which are not confined to a cell. In fact, our analysis of the deterministic model shows that the approximation of homogenous cytosolic distribution of MinD and MinE is appropriate and that this approximation might have an important implication regarding experiments. One might expect that oscillations are observable in a purified system containing essentially only MinD, MinE, and phospholipid vesicles. Our analysis suggests that oscillations will show up in the presence of a homogenous distribution of cytosolic proteins. Therefore, the closed geometry of the bacterium might not be essential, and an open geometry could be used instead.

How do the Min-oscillations regulate the position of the Z-ring?

Our numerical calculations of the deterministic and the stochastic case give a MinD-distribution which has a minimum in time average at the cell center. An obvious mechanism for Z-ring positioning may be based on the existence of such a minimum [63]. Starting from an almost homogeneous average distribution, the depth of the minimum increases with the system length (figure 3.5). This feature could also be used to couple the constriction of the Z-ring to the cell length and, hence, to control the cell cycle. Qualitatively, this behavior was confirmed experimentally (figure 2.12).

However, in our view, the mechanism based on the mid-cell minimum may have been overemphasized in the recent literature and not analyzed sufficiently. This is still an unsolved problem and we would like give two arguments: one against and one in favour of

this mechanism.

(i) What do we know about the MinC proteins in connection to this issue? They depolymerize the Z-ring filaments in *vitro*, and *minc⁻* mutants allow for division near the cell poles. In principle, the mechanism based on the minimum of the time-averaged protein concentration in the middle is not necessary. In fact, let us consider a two-thresholds based mechanism: (i) one threshold for the local protein density, C_{th}, below which the growth of the Z-ring is permitted, (ii) a threshold for the time, T_{th}, during which the threshold C_{th} is not to be exceeded in order for the Z-ring to grow. It is easy to show that a time-averaged protein concentration with a maximum at the cell center can be obtained also with $(c_d + c_{de}) < C_{th}$ at the mid-cell for a time much longer than T_{th}, i.e. thus allowing for the growth of the Z-ring. Indeed, some of our measurements show a time-average MinD concentration which is approximately flat, see figure 2.12.

(ii) On the other hand, we would like to make the following point: The MinC protein concentrations does not entirely correspond to the MinD protein concentration. In fact, MinE and MinC cannot bind MinD simultaneously [22]. This means that in order to obtain the MinC protein concentration on the membrane, the MinE membrane-bound protein concentration has to be subtracted from the total MinD membrane-bound protein concentration. Now, the MinE ring is oscillating near the mid-cell and its time-averaged concentration shows a maximum at the mid-cell (see figure 2.13), therefore the MinC protein concentration at the cell center is much lower than the MinD one.

Also, one should be aware of the possibility that, in addition to the Min system and "nucleoid occlusion", other yet to be identified factors may explain the high spatial precision of division-site placement.

The selection of different oscillatory patterns of the Min-protein distributions as a function of the cell length provides the bacterium with information about its own length and could thus be used to regulate cell division. Given a certain value of the average total protein density, there is a threshold L_{min} corresponding to the minimal length supporting oscillations. It fixes the minimal value at which the cell can divide. When the cell grows, oscillations start with the characteristic "one stripe" spatial pattern. Before the doubling of the spatial period of this pattern, the Z-ring is located in a MinC poor domain that allows the ring to grow. After period-doubling, i.e. the acquisition of a second "stripe", the Z-ring is located in MinC rich domain. We can speculate that the same protein, MinC, that inhibits the growth of the Z-ring once its growth has started might induce a conformational change in FtsZ protein that leads to Z-ring contraction. Thus, the cell cycle would be controlled by the period-doubling of the spatial pattern of the Min-protein concentrations, *i.e.* by the cell length. Recent theoretical and experimental studies suggest also that chromosome segregation might be directly related to the cell

length [55, 56] due to entropic effects.

Are there helices?

In order to keep abreast of the experiments, the formation of MinD helices must be included. To this end, it is necessary to consider a 3-D system and include, starting from a microscopic level, a mechanism capable of generating filaments. The mechanism introduced in [72] based on nucleation sites at the cell poles is in our opinion not adequate. In fact, the existence of stripes in long cells, where the division is blocked, suggests that the polar location in normal cells is not the result of a membrane property unique to the poles of the cell. In this way, on the one hand such a model introduces an ad hoc hypothesis, and on the other hand it is not capable of reproducing the characteristic striped patterns of the Min oscillations. A key point is the dynamics of these helices, i.e. do they originate from a fixed spiral scaffold, or are they moving along the cell following the oscillations? Future experiments will clarify this point.

The model introduced by Pavin *et al.* [73] also used an ad hoc hypothesis in order to generate filaments. In particular, they considered four different rates for the detachment process of MinDE:ATP complexes, depending on how many bonds a MinD:ATP has formed with its MinD:ATP neighbors.

The effect of noise

In order to study the possible effects of noise due to the low number of involved proteins, we performed computer simulations of a particle-based description. The probability for each event was calculated according to the corresponding probability in the master equation. Stochastic simulations were compared with deterministic simulations and experimental data from LSCM. Together with our experimental measurements, this study points to the importance of investigating the Min-protein dynamics through single cell measurements. In fact, the concentration of a certain protein in a population of genetically identical cells varies from cell to cell due to stochastic processes [83, 84]. Experimental observations [63] indicate that the period increases with the MinD concentration and decreases with the MinE concentration. The last observation is consistent with our numerical simulations, see figure 3.6. The cell-cell variations in protein concentrations are often on the order of ten percent of the mean [144–147]. We believe that this is the most important contribution to explaining the spread of the data shown in figure 2.14. On the other hand, we found that the fluctuations in the period in a single cell at fixed length and

average total protein density either numerically, due to internal noise, or experimentally[2], are small enough to allow, in principle, for a measurement that shows the characteristic behavior predicted by our theoretical model, see figure 3.4 and 4.9. Figure 2.15 shows a first attempt of such a measurement. Although it is not clear if this measurement can differentiate between the different proposed models, it would be an important test for our model.

Furthermore, as can be seen in figure 4.4, we found that stochasticity destroys oscillations at high protein number corresponding to values of the total protein concentration where the deterministic case still shows oscillation. The opposite happened at low protein number where fluctuations are necessary in order to generate oscillations. Moreover, figure 4.8 shows that in our model fluctuations allowed the system to exploit low protein numbers to generate more precise time-averaged distributions with a more pronounced minimum at mid-cell. We noticed that all simulations were performed at the constant ratio of $D/E \simeq 2.6$, it would be interesting to study these behaviors for different values of this ratio.

Finally, to bridge the gap between the microscopic and the deterministic descriptions, a Langevin equation for the fluctuating protein densities was derived through coarse graining of the microscopic master equation. In this way, we analytically showed the relationship between the master equation, used to calculate the probability of each event in the microscopic simulations, and the deterministic equations (3.2.3) and (3.2.4). Therefore, the stochastic simulations justify the deterministic model, showing that oscillations are resistant to the perturbations induced by the stochastic reactions and by diffusion. Writing the LE, we also developed an analytical description that keeps separate the noise terms associated with the different processes, allowing for an estimation of their relative contributions. We analytically showed (see appendix G) that the relative fluctuations of the cytosolic protein concentrations are smaller when they are compared with the relative fluctuations of the membrane-bound protein concentrations. In the limit when the noise prefactor Ω vanishes, the LEs allow for a direct comparison with the deterministic case. For these reasons we believe that the numerical integration of these equations can give rise to interesting developments in the study of the noise in the Min-system, and, speaking more generally, this approach could be applied to the study of noise in other biological spatially extended systems. Finally, we notice that once the LEs are numerically integrated, our stochastic simulations can then be used to validate the description of the system that the LEs result in.

---

[2]In this case the protein density was not under experimental control.

Similar systems

The Min system is a prime example of a mechanism that controls spatial relationships within the cell. It will be of interest to see if other mechanisms of topological identification and spatial regulation work in a similar manner in other systems. A possible candidate could be the bacterium *B. subtilis*, where MinCD proteins prevent septation near the poles, making a stationary pattern with a minimum of the concentration at mid-cell. In a different context respect to the cell division process, it will be interesting to see if there are any similarities between the Min-oscillations and the FrzS-oscillations found in *Myxobacteria* [31]. FrzS is a protein that regulates mobility in *Myxobacteria* which is mediated by type *IV pili*[3]. Oscillations of FrzS suggest that for each reversal some components at the leading cell pole are inactivated to allow for a function of the *pili* at the opposite pole.

Closing remarks

While the mechanism of a dynamic instability inducing Min-protein oscillations has been conclusively established as fundamental by all existing models, including the model studied here, a fully quantitative model of the Min-protein dynamics is still missing. Testing the basic assumptions of our model, probing its predictions, measuring some of the model parameters, and studying the effects of noise, we hope to get going in that direction.

With this we end our story for now in confidence that understanding the physics of cell division will have important applications in the near future. For example, one might envision therapeutic strategies that suppress the replication of bacterial cells which cause infections. At a level of greater abstraction, this knowledge might prove useful to building an artificial cell [165], thereby being instrumental in recreating life.

---

[3]*Pili* are used to adhere to surfaces and to facilitate the genetic exchange between bacteria.

Appendix A

Materials and Methods

Flourescence video-rate microscopy

Bacteria of the *E. coli* K12 strain JS964 were generously donated by J. Lutkenhaus, University of Kansas. Bacteria taken from the freezer were grown overnight in 3ml Luria-Bertani (LB) medium at 37°C together with 3μl spectinomycin. The overnight culture of 500μl was added to 50μl spectinomycin and $50ml$ LB medium and then grown at 37°C for two hours. The expression of MinD-GFP was induced by 50μl IPTG and growing the bacteria at 31°C for at least one hour. The bacteria were immobilized for fluorescence imagery by using silane-coated cover slips. Fluorescent images were taken at room temperature with an inverted microscope (Axiovert 200M, Zeiss) using a $100\times$ NA 1.4 oil immersion objective and a CCD camera from Spot Diagnostic Instruments, Inc. driven by Metavue (Universal Imaging). The frame rate for measuring the time-average in figure 2.10 was 1Hz and varied between 0.33Hz and 1Hz for the data in figure 3.4b. Data were analyzed using Metamorph (Universal Imaging).

FCS

Sample Preparation
Bacteria of the *E. coli* K12 WM1079 and WM1255 strains and of the *E. coli* K12 strains JS964 were kindly donated by W. Margolin, Houston Medical School at University of Texas, and J. Lutkenhaus, University of Kansas, respectively. Bacteria of the *E. coli* BL21 strains BL21(DE3)pLysS were obtained from Novagen (CN Biosciences). GFPmut2(S65A,V68L,S65T) [23, 166] were expressed in bacteria of the *E. coli* K12 JS964, WM1079 and WM1255 strains. EGFP and His6-EGFP, with the same kind of mutant, EGFP(F64L/S65T) were expressed in bacteria of the *E. coli* BL21 strains

BL21(DE3)pLysS using the vector pBAT4 and pET9d, respectively. The strains WM1079 and WM1255 were also used in [167, 168], where it was possible to find general information about the plasmids. For information about the strain JS964 see [23, 169]. *E. coli* strains were grown overnight in 3ml LB medium at 37°C together with a concentration of $25\mu g/ml$ Spectinomycin, $25\mu g/ml$ Kanamycin, $20\mu g/ml$ Chloramphenicol and $50\mu g/ml$ Ampicillin, respectively for JS964, BL21, WM1079 and WM1255 strains. The LB medium consists of 10g of tryptone, 5g of yeast extract and 5g of NaCl per liter. The overnight culture of $500\mu l$ together with the same concentration of antibiotics as above, was added to $50ml$ of fresh LB medium and grown at 37°C until the optical density (OD) at $600nm$ reached ≈ 0.2. The expression of GFP-MinD in JS964 and EGFP in BL21(DE3)pLysS was induced by adding $20\mu M$ isopropyl-β-D-thiogalactopyranoside (IPTG). The expression of MinE-GFP in WM1079 was induced by adding 0.005% L-arabinose. No inducer was used for GFP-MinD expression in WM1255 and for His6-EGFP expression in BL21(DE3)pLysS. Then the bacteria were grown at 30°C for 1-2 hours usually sufficient to produce visible fluorescence and to see Min proteins oscillations. Different induction levels were tested to find the best signal to noise ratio in the measurements of the correlation function and to minimize perturbations to cellular physiology. In fact, $G(0)$ is inversely proportional to the number of fluorophores, and with a high level of induction the signal will be very low. In addition, to avoid fluorescent impurity, samples of the LB medium were prepared with a lower level of yeast extract of 1g per liter. For microscopic examination a solid slab of 1% agarose (Invitrogene, 15510-027) in LB medium had previously been prepared. A molten (geling temperature 37-42°C for 2% agarose concentration) 1% (wt/vol) agarose/LB medium, was sandwiched between a 25mm×75mm glass slide and a 18mm×18mm cover slide and allowed to cool to room temperature. Before measurements, the cover slide was removed and $3\mu l$ of cell culture were spread on to this pad (18 mm × 18 mm × $\approx$ 0.5 mm) of solid agarose. This method allows for the immobilization of the cells and for keeping the sample near the objective as is necessary for FCS measurements. At the same time, this does not allow the cells to settle into multiple planes of view as, would happen if the cells were mixed with the liquid agarose and then cooled. The cells also grow and divide more easily on the slides. Data collection lasted no more than 2h on each slide.

Optical setup

Fluorescence Correlations Spectroscopy (FCS) measurements were performed on a LSM Meta 510 system (Carl Zeiss, Jena, Germany) using a 40× NA 1.2 UV-VIS-IR C-Apochromat water immersion objective and a home-built detection unit at the fiber output channel: A bandpass filter (AHF Analyse Technik, Tübingen, Germany) was used

behind a collimating achromat to reject the residual laser and background light. Another achromat (LINOS Photonics, Göttingen, Germany) with a shorter focal length was used to image the internal pinhole onto the aperture of the fiber of the avalanche photo diode (APD, PerkinElmer, Boston, MA, USA). The correlation curves were obtained with a hardware correlator Flex 02-01D (correlator.com, Bridgewater, NJ, USA). The position for FCS measurements could be selected accurately in a corresponding LSM image. The waist w_0 of the detection volume was determined in calibration measurements with free Alexa 488 in water to be $w_0 = 157 \pm 12$ nm assuming a diffusion constant of $D = 280 \frac{\mu m^2}{s}$.

Theoretical autocorrelation curves. The experimental autocorrelation curves were analyzed by fitting the expected autocorrelation curves for different processes. Since the actual height of the detection volume is larger than the diameter of the bacterium, the cytosolic diffusion can be approximated to occur in two dimensions. Fitting with a more refined model, taking into account the geometry of the detection volume in the bacterium [170], did not significantly change the values obtained by assuming the simplified geometry. For two independent species, diffusing with respective diffusion constants D_1 and D_2 the correlation curve is [89, 171]

$$G_{\text{diff}}(\tau) = \frac{1}{N_1 + N_2} \left\{ F \frac{1}{1 + \tau/\tau_1} + (1 - F) \frac{1}{1 + \tau/\tau_2} \right\} \quad . \tag{A.0.1}$$

Here, the number fraction of particles of one species is given by $F = N_1/(N_1 + N_2)$, where N_1 and N_2, respectively, are the average numbers of particles of the different species in the detection volume. The characteristic relaxation times τ_1 and τ_2 are linked to the respective diffusion constants and the width w_0 of the detection volume through $\tau_i = w_0^2/(4D_i)$, $i = 1, 2$. For a single species diffusing anomalously in two dimensions the autocorrelation function is given by [93–95] as

$$G_{\text{a}}(\tau) = \frac{1}{N} \frac{1}{1 + \left(\frac{\tau}{\tau_{\text{a}}} \right)^\alpha} \quad . \tag{A.0.2}$$

Here, $\tau_{\text{a}}^{-\alpha} = 4\Gamma/w_0^2$, where the anomalous exponent α governs the spreading of an initially localized distribution, $\langle x^2 \rangle \sim t^\alpha$ and Γ is the anomalous transport coefficient. For particles changing between a mobile state (diffusion constant D) and an immobile state we assume the following reaction kinetics for fraction F of the mobile state $dF/dt = -F/\tau_1 + (1 - F)/\tau_2$, where τ_1 and τ_2 are the cytosolic and membrane residence times, respectively. The autocorrelation of the fluctuations has the form [89, 171]

$$G_{\text{ex}}(\tau) = \frac{(2\pi)^{-2} w_0^2}{(N_1 + N_2)} \int_0^\infty dk\, k\, e^{-\frac{w_0^2}{4}(k_x^2 + k_y^2)} \left\{ A_1 e^{\lambda_1 \tau} + A_2 e^{\lambda_2 \tau} \right\} \quad , \tag{A.0.3}$$

where $\lambda_{1,2} = -(Dk^2 + \tau_1^{-1} + \tau_2^{-1})/2 \pm \{(Dk^2 + 1/\tau_1 + 1/\tau_2)^2 - 4Dk^2/\tau_2\}^{1/2}/2$, $A_{1,2} = \{\lambda_{2,1} + Dk^2\tau_1/(\tau_2 + \tau_1)\}/(\lambda_{2,1} - \lambda_{1,2})$.

Since the cytoplasmic pH of *E. coli* is about 7.7 [172], pH-dependent blinking can be neglected [173].

Data analysis

The correlation curves were fitted in the time interval $\tau \in [5\mu s, 1s]$ with a weighted nonlinear least-squares fitting algorithm. Curves were selected automatically based on the convergence of the fit algorithm and the quality of the fit ($\chi^2 < 1.3$ for EGFP and $\chi^2 < 1.5$ for Min proteins). For the Min proteins, curves were at first hand-selected for low and high intensity phases and then automatically for the quasi-steady states. The latter were checked by requiring a constant fluorescence intensity during the measurement.

Period measurement in single cells.

We used bacteria of the *E. coli* K12 JS964 strain expressing GFP-MinD, and we prepared the sample in the same way as for the FCS measurements. To make measurements of growing cells possible we used a heater and a chamber for live cell imaging (Bachhoffer Chamber). Measurements were performed on an inverted Laser scanning Confocal Microscope (LSCM), Zeiss Axiovert 200, manual stage (Jena, Germany) using a $100\times$ NA 1.4 oil immersion objective. The position for measurements could be selected accurately in a corresponding LSM image.

Appendix B

FRAP & FCS

Basic concepts

Fluorescence is a part of the luminescence class processes in which molecules emit light from electronically excited states. The formation of luminescence through excitation of a molecule by ultraviolet or visible light photons is termed photoluminescence, which is formally divided into two categories, fluorescence and phosphorescence, depending on the nature of the excited state. Fluorescence is the emission of light from singlet excited states. In excited single states, the electron in the excited orbital is paired (to opposite spin) to the second electron in the ground-state orbital. Consequently, the return to the ground state is spin allowed and occurs rapidly by the emission of a photon. **Phosphorescence** is the emission of light from triplet excited states. An electron in the excited orbital has the same spin orientation as the ground-state electron, and according to Pauli's principle, transitions to the ground state are forbidden, which results in rate constants for the triplet emission that are several orders of magnitude lower than those for fluorescence.

Photobleaching (also termed fading) occurs when a fluorophore permanently loses the ability to fluoresce due to photon-induced chemical damage and covalent modification. The probability for a transition from an excited singlet state to an excited triplet state increases with the intensity of the excitation light. Because the triplet state is relatively long-lived with respect to the singlet state, fluorophores have enough time to undergo chemical reactions with components in the environment and produce irreversible modifications. Each fluorophore has different photobleaching-characteristics, depending on the molecular structure and the local environment.
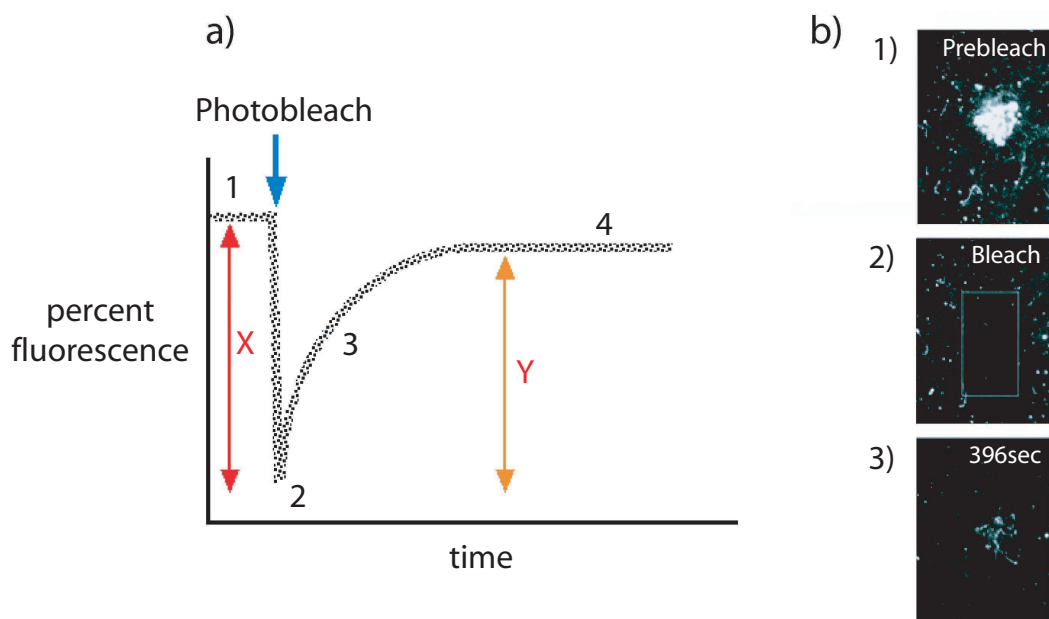
Figure B.1: Fluorescence Recovery After Photobleaching. a) Fluorescence recovering as a function of time during a FRAP experiment. (1) A baseline of fluorescence is collected before photobleaching occurs (image b1); (2) Photobleaching (blue arrow and image b2); (3) The amount of fluorescence in the photobleached area increases as unbleached molecules migrate into this area (3 and image b3). b) Images (taken from [174]) of viral glycoprotein ts045 VSVG tagged with green fluorescence protein (VSVG-GFP) and photobleached in the rectangular area shown in image (2).

FRAP

Fluorescence Recovery After Photobleaching (FRAP) consists of measuring the fluorescence recovery after optically bleaching the molecules in a certain region by high excitation laser power. The analysis of this process reveals information about the underlying protein dynamics.

The principles of FRAP are illustrated in figure B.1. In a selected area the fluorescence intensity is collected before and after photobleaching occurs. Immediately after photobleaching the intensity decreases. Over time, the amount of fluorescence increases as unbleached molecules move into the bleached area. Later, there is a stabilization of the amount of fluorescence recovery. If X is the fluorescence before photobleaching and Y is the amount of fluorescence that returned to the bleached area, the ratio X/Y almost never reaches 1. The mobility is determined by the slope of the curve of the intensity in function of the time during the recovering phase. The steeper the curve, the faster the recovery and, therefore, the more mobile the molecules.

For FRAP experiments it is important to choose a dye which bleaches minimally at low illumination power to prevent photobleaching during image acquisition but bleaches quickly and irreversibly at high illumination power.

In addition, a high protein number is needed [175]. In bacteria, a region of half of the cell size is bleached and fluorescence recovery is due to proteins coming from the opposite half. An example is given in [88], where the FRAP technique was used to measure GFP mobility in *E. coli*. In the case of the Min proteins, FRAP is clearly not appropriate. In fact, as is shown in section 2.2.1, the dwelling time, during which half of the cell is almost empty and half is almost full of proteins, is an order of magnitude larger then the diffusion time. So, bleaching half of the cell, no proper fluorescence recovery would be observed.

FCS

Distinct from other fluorescence techniques, Fluorescence Correlation Spectroscopy (FCS) does not exploit the emission intensity itself but rather intensity fluctuations. Intensity fluctuations in the fluorescence signal collected from a small volume are caused by the motion of fluorescent particles or chemical processes leading to changes in the fluorescence intensity of individual particles. Among the many physical parameters in principle accessible by FCS are local concentrations, mobility coefficients and rate constants of reactions. In the following we will give a short introduction to FCS. For the interested reader the are many reviews and books that introduce the technique [89, 171, 176–179].
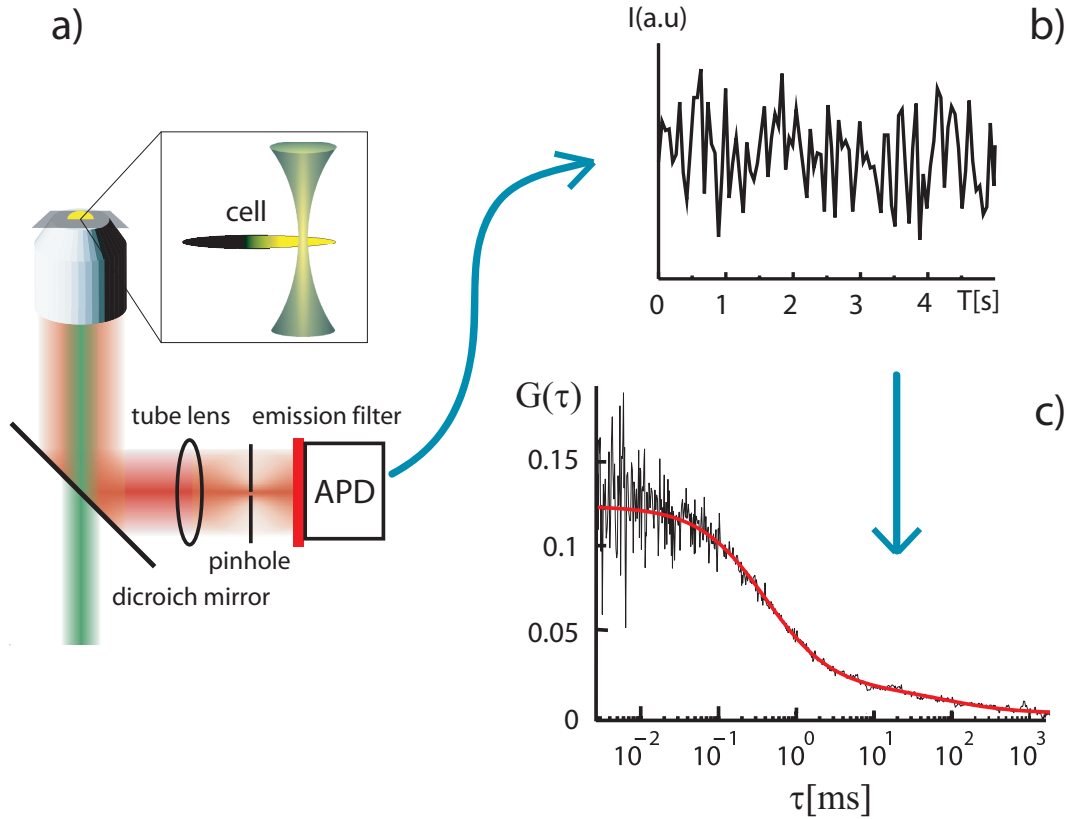
Figure B.2: FCS measurement. a) Fluorescent light from a nM volume in the cell is collected by means of a dichroic mirror through a tube lens, a pinhole and an emission filter to APD which amplifies the signal. b) GFP-MinD fluorescence signal in function of the time for a single run of $5s$. c) Fit (red curve) with a $2 - D$ diffusion formula B.0.5 of the correlated signal in b).

The number of molecules within a given volume is at any time governed by the Poisson distribution. Then, the root mean square fluctuation of the particle number N is

$$\frac{\sigma_N}{<N>} = \frac{1}{\sqrt{N}} \quad . \tag{B.0.1}$$

Therefore, fluctuations are bigger for small numbers. To perform FCS measurements properly, it is important to have concentrations and detection volumes so that only few molecules are detected simultaneously. However, the fluorescence signal must be higher than the residual background signal. Typical values are nanomolar or sub-nanomolar concentrations and detection volumes in the femtoliter ($10^{-15}l$) range. FCS was introduced in 1972 by Madge *et al* [180], but efficient detection characteristics were achieved only in 1993 with the implementation of confocal microscopy FCS [181]. Figure B.2a shows a typical schematic confocal FCS setup. The actual setup we used in our measurements is

shown in figure 2.16. With this setup, the incoming laser light, through a dichroic mirror, is focused by a high numerical aperture objective to a diffraction limited volume. The fluorescent light from the sample is collected by the same objective and passed through the dichroic and the emission filter. In addition, a pinhole in the image plane blocks all light not coming from the focal region. For molecule concentrations in the nM range or below, the detection of signal fluctuations resulting from individual particles is possible. Subsequently, the light is focused onto an avalanche photodiode detector. The resulting signal is shown in figure B.2b. Improvements could be made using strong and stable sources like lasers and very sensitive detectors as avalanche photodiodes (APD) with single-photon sensitivity. The characteristics of the fluorophore are also important, namely fluorescence lifetime and quantum yield. The quantum yield is the number of emitted photons relative to the number of absorbed photons. Substances with fluorescence photon yields per single molecule approaching unity display the brightest emission. The lifetime determines the time available for the fluorophore to be recorded during interactions with or diffusion in its environment. The fluorescence lifetime is about $1 - 10ns$. The phosphorescence lifetimes typically go from milliseconds to seconds. The triplet-state population induces correlations in the recorded fluorescence signal and is the most conspicuous fast dynamics that can be observed in FCS measurements.

The mathematical quantity used to quantify fluctuations is called the correlation function. In the case of the temporal fluctuations of the fluorescence signal $F(t)$ this quantity is:

$$g(\tau) = \langle F(t)F(t+\tau)\rangle - \langle F(t)\rangle\langle F(t+\tau)\rangle \quad , \tag{B.0.2}$$

where $\langle\cdot\rangle$ denotes an ensemble average and t and τ are two different instant time. Now, it is clear that if the signal is completely uncorrelated, $g(\tau) = 0$ for every τ. Assuming that the system under investigation is in the equilibrium state the fluorescence signal $F(t)$ is a stationary random process, which means that it can be expressed as zero-mean fluctuations $\delta F(t)$ around a constant mean value $\langle F(t)\rangle$:

$$F(t) = \langle F(t)\rangle + \delta F(t) \quad ; \qquad \langle \delta F(t)\rangle = 0 \quad , \tag{B.0.3}$$

where δF denotes the fluctuations around a constant value $\langle F(t)\rangle$. In other words the system is invariant in respect to the temporal translation $\langle F(t)\rangle = \langle F(t+\tau)\rangle$, and the correlation function can be written as

$$g(\tau) = \langle F(t)F(t+\tau)\rangle - \langle F(t)\rangle^2 \quad . \tag{B.0.4}$$

In experimental situations, the ergodic theorem is applied and the ensemble averaging is replaced by time-averaging: $\langle \cdot \rangle = (1/n) \sum_{i=0}^{n-1}$; $\tau = m\Delta t$, $n\Delta t$ is the total duration of the experiment and Δt is the sampling interval with n and m integer. The mean fluorescence intensity is strictly positive: $\langle F(t) \rangle > 0$ and the *normalized* correlation function is defined as

$$G(\tau) = \frac{g(\tau)}{\langle F \rangle^2} + 1 = \frac{\langle \delta F(t) \delta F(t+\tau) \rangle}{\langle F(t) \rangle^2} \quad . \tag{B.0.5}$$

The correlation amplitude $G(0) > 0$ is the normalized variance of the fluctuating fluorescence signal $\delta F(t)$. In the experimental setup displayed in figure B.2b, the fluorescence signal is evaluated by a hardware correlator PC card for a time T to obtain the autocorrelation function $G(\tau)$. A typical experimental $G(\tau)$ curve is shown in figure B.2c. If there is some memory in the signal, *i.e.* some correlation between fluctuations at time t and fluctuations at a later time $t + \tau$, then $G(\tau) \neq 0$ at some range for the values of the lag time τ around zero. When τ becomes large when compared to the characteristic memory time of the system, the signal values separated by τ become statistically independent and $G(\tau)$ decays to zero. The characteristic time decay of the correlation function is then associated with the characteristic time of the physical process generating the observed fluctuations, as, for example, thermal diffusion. The slower the decay of the correlation function, the longer is the memory of the associated physical process.

Making an appropriate hypothesis on the physical origin of the fluctuations and on the efficiency of the setup, it is often possible to write an analytical expression for $G(\tau)$ in terms of the physical parameters to be measured and, using this formula, to fit the experimental curve as is shown in figure B.2c. Assuming that all fluctuations come from the variation in the local concentration δC within the focal volume V, it is possible to write $\delta F(t)$ in terms of $\delta C(t)$

$$\delta F(t) = \eta \int_V I(\vec{r}) \delta C(\vec{r}, t) dV \quad , \tag{B.0.6}$$

where η is a parameter that includes the physical characteristics of the fluorophore, like fluctuations in the quantum yield and in the molecular absorption cross-section, the detection efficiency and the maximum value of the excitation energy and determines the photon count rate per detected molecule per second. This parameter can be a measure for the signal to noise ratio. $I(\vec{r})$ describes the spatial distribution of the emitted light and in the usual confocal illumination/detection optical FCS setup can be approximated by a

Gaussian intensity illumination profile

$$I(\vec{r}) = exp\left(-\frac{2(x^2 + y^2)}{w_{xy}^2} - \frac{2z^2}{w_z^2} \right) \quad , \tag{B.0.7}$$

where w_z and w_{xy} are the sizes of the beam waist in the direction of the propagation of light and in the perpendicular direction, respectively. Introducing equation (B.0.7) in equation (B.0.6) and equation (B.0.6) in equation (B.0.5) we obtain the general expression:

$$G(\tau) = \frac{\int_{V'} \int_V I(\vec{r}) I(\vec{r}') \langle \delta C(\vec{r}, 0) \delta C \rangle (\vec{r}', \tau) dV dV'}{(\langle C \rangle \int_V I(\vec{r}) dV)^2} \quad . \tag{B.0.8}$$

Now, solving the equation for the relaxation of δC, we can obtain a formula for the specific case we are considering. Given s chemical components with concentrations $C_i(\vec{r}, t)$ participating in diffusion and chemical reactions near the equilibrium, the nonlinear equation can be linearized and the equation for δC_i is

$$\frac{\partial \delta C_i(\vec{r}, t)}{\partial t} = D_i \nabla^2 \delta C_i(\vec{r}, t) + \sum_{k=1}^{s} T_{ij} \delta C_j(\vec{r}, t) \quad , \tag{B.0.9}$$

where the first term accounts for diffusion and T is a matrix of kinetic coefficients. For example, in the case of two diffusing non-interacting species, equation (B.0.9), consist of the diffusion equation for each species, respectively, which can be solved easily. In our experimental condition, we can assume $w_z^2 \gg w_{xy}^2$ and approximate the $3D$ diffusion with a two-dimension diffusion in the xy plane. From equation (B.0.8) we obtain the following expression for the correlation function

$$G(\tau) = \frac{\bar{N}_1}{\left(\bar{N}_1 + \bar{N}_2 \right)^2} \left(\frac{1}{1 + \tau/\tau_{D_1}} \right) + \frac{\bar{N}_2}{\left(\bar{N}_1 + \bar{N}_2 \right)^2} \left(\frac{1}{1 + \tau/\tau_{D_2}} \right) \quad , \tag{B.0.10}$$

where $\bar{N}_i$ is the average number of the molecules in the sampling volume $V_{\text{eff}} = \pi^3 w_{xy} w_z$: $\bar{N}_i = V_{\text{eff}} \langle C_i \rangle$, and

$$\tau_{D_i} = \frac{w_{xy}^2}{4D_i} \tag{B.0.11}$$

is the lateral diffusion time during which a molecule remains in the focal volume. The expression of $G(\tau)$ in equation (B.0.10) can be used to fit experimental autocorrelation

curves with four parameters: the relative fraction of the two species $F = \bar{N}_1/(\bar{N}_1 + \bar{N}_2)$, one of the two average number $\bar{N}_i$, and the two diffusion times.

To summarize, both FCS and FRAP are methods for investigating the mobility of fluorescent proteins. However, due to the different characteristics of these methods, the fields of application are different. FCS is capable of monitoring the volume of less than 1 femtoliter inside the living cell and registering the fluorescence fluctuations resulting from diffusion of individual molecules. It is sensitive in the nM to μM range and allows for the calculation of the actual diffusion coefficient and precise local concentration. It is applied to the study of very fast to slow processes (μs to s). FRAP is applied generally to higher concentrations (mM) and slower processes. It allows the calculation of the diffusion coefficient and percentage of mobile and immobile fractions. Inherently being an imaging technique, FRAP also helps to visualize the connectivity of cellular compartments.

Appendix C

Reduction from three dimensions to one dimension

Here, we show how the dynamics of the Min protein distributions in three spatial dimensions can be reduced to a description in one spatial dimension. The bacterium is conveniently approximated by a cylinder with radius R_0 and length L. The volume densities of cytosolic MinD and MinE at a given point are $c_D(r, \vartheta, x)$ and $c_E(r, \vartheta, x)$, respectively. Here, r and ϑ denote the radial and azimuthal coordinate, respectively, while x is the coordinate along the long axis. Their time evolution is governed by

$$\partial_t c_D(r, \vartheta, x) \quad = -\omega_D(c_{\max} - c_d(\vartheta, x) - c_{de}(\vartheta, x))c_D(r, \vartheta, x)\delta(r - R_0)$$

$$+\omega_{de}c_{de}(\vartheta, x)\delta(r - R_0) + D_D\Delta_{3d}c_D(r, \vartheta, x) \quad , \qquad \text{(C.0.1)}$$

$$\partial_t c_E(r, \vartheta, x) \; = -\omega_E c_d(\vartheta, x)c_E(r, \vartheta, x)\delta(r - R_0) + \omega_{de}c_{de}(\vartheta, x)\delta(r - R_0)$$

$$+D_E\Delta_{3d}c_E(r, \vartheta, x) \quad . \qquad \text{(C.0.2)}$$

Here, c_d and c_{de} are the surface densities of membrane-bound MinD and MinDE-complexes, Δ_{3d} is the three-dimensional Laplace-operator, and the factors of $\delta(r - R_0)$ restrict attachment to and detachment from the cytoplasmic membrane to a region adjacent to the cell wall.

Since the diffusion constant of cytosolic MinD and MinE is of the order of $15\frac{\mu m^2}{s}$, and the diffusion length of the order of $2\mu m$, whereas the period of the oscillations is about 1min, we consider the density of cytosolic MinD and MinE to be homogenous perpendicular to the bacterial long axis. The volume densities of cytosolic MinD and

MinE can then be replaced by surface densities $\tilde{c}_D$ and $\tilde{c}_E$ with

$$c_D(r, \vartheta, x) = \frac{1}{R_0}\tilde{c}_D(\vartheta, x) \quad , \tag{C.0.3}$$

$$c_E(r, \vartheta, x) = \frac{1}{R_0}\tilde{c}_E(\vartheta, x) \quad . \tag{C.0.4}$$

Then, the equations governing the evolution of the protein densities are read as

$$\partial_t \tilde{c}_D = -\frac{\omega_D}{R_0}(c_{\max} - c_d - c_{de})\tilde{c}_D + \omega_{de}c_{de} + D_D\Delta_{2d}\tilde{c}_D \quad , \tag{C.0.5}$$

$$\partial_t \tilde{c}_E = -\frac{\omega_E}{R_0}c_d\tilde{c}_E + \omega_{de}c_{de} + D_E\Delta_{2d}\tilde{c}_E \quad , \tag{C.0.6}$$

$$\partial_t c_d = \frac{\omega_D}{R_0}(c_{\max} - c_d - c_{de})\tilde{c}_D - \frac{\omega_E}{R_0}c_d\tilde{c}_E - \nabla \cdot \mathbf{j}_d \quad , \tag{C.0.7}$$

$$\partial_t c_{de} = \frac{\omega_E}{R_0}c_d\tilde{c}_E - \omega_{de}c_{de} \quad , \tag{C.0.8}$$

where $\mathbf{j}$ is the aggregation current of MinD on the inner cell membrane and Δ_{2d} is the two-dimensional Laplace operator on the cylinder surface.

It has been shown that MinD forms a filamentous structure on the inner cell membrane [68]. The projection onto this structure yields line-densities, e.g., $\bar{c}_d(x) = \int_0^{2\pi} c_d(\vartheta, x)R_0 \, d\vartheta$. They are connected to the surface densities via

$$\tilde{c}_D(\vartheta, x) \approx \frac{1}{2\pi R_0}\bar{c}_D(x) \quad , \tag{C.0.9}$$

$$\tilde{c}_E(\vartheta, x) \approx \frac{1}{2\pi R_0}\bar{c}_E(x) \quad , \tag{C.0.10}$$

$$c_d(\vartheta, x) \approx \bar{c}_d(x)\delta(\vartheta - \vartheta(x)) \quad , \tag{C.0.11}$$

$$c_{de}(\vartheta, x) \approx \bar{c}_{de}(x)\delta(\vartheta - \vartheta(x)) \quad , \tag{C.0.12}$$

where $\vartheta(x)$ parameterizes the MinD-helix on the inner cell membrane. The dynamic equations for the line densities $\bar{c}_D$, $\bar{c}_E$, $\bar{c}_d$, and $\bar{c}_{de}$ are then given by equations. (3.1.1)-(3.1.4). The current j_d appearing there is obtained by the projection of the surface current $\mathbf{j}_d$ onto the x-direction. Note that a description of the formation of MinD-helices would also require a specification of the perpendicular component of the current $\mathbf{j}_d$.

Appendix D

Linear stability analysis of the homogenous distribution

In this appendix, we carry out the linear stability study for the case of homogenous cytosolic distributions, non-homogenous cytosolic distributions, and a finite ATP exchange rate.

The stability analysis is performed in terms of microscopic parameters, the interaction strengths U_d and U_{de}, and the interaction ranges r_d and r_{de} between membrane-bound MinD proteins and membrane-bound MinD and MinDE complexes, respectively. They are linked to the phenomenological parameters ks in equations (3.2.3) and (3.2.4) through

$$k_1 \;=\; \frac{1}{c_{\max}^2}\frac{D_d}{k_B T}U_d \quad, \tag{D.0.1}$$

$$k_2 \;=\; \frac{1}{c_{\max}^2}\frac{D_d}{k_B T}U_d r_d^2 \quad. \tag{D.0.2}$$

Similar expressions hold for $\bar{k}_1$, and $\bar{k}_2$. We introduce the dimensionless fields $\tilde{c}_{d,de}(x,t)$ defined as $\tilde{c}_{d,de} = c_{d,de}/c_{\max}$ and a similar expression for the quantities C_D and C_E. We define the rates $\tilde{\omega}_{D,E} = \omega_{D,E}c_{\max}$, where $\omega_{D,E}$ are the parameters introduced in equations (3.2.3) and (3.2.4). To simplify the notation in the following the "tilde" will be dropped. We introduce the dimensionless parameters $\alpha = \omega_D/\omega_E$, $\beta = \omega_{de}/\omega_E$, $g_d = U_d/k_B T$, $g_{de} = U_{de}/k_B T$ and scale time and space like $\tau = \omega_E t$, $\xi = x/l_d$, where $l_d = \sqrt{D_d/\omega_E}$ is the diffusion length of MinD proteins on the membrane. We also define $\eta_d = (r_d/l_d)$ and $\eta_{de} = (r_{de}/l_d)$. The dimensionless version of equations (3.2.3) and (3.2.4) take the following shape

$$\partial_\tau c_d = \alpha(1 - c_d - c_{de})C_D - c_d C_E - \partial_\xi j_d \quad,$$

$$\partial_\tau c_{de} = -\beta c_{de} + c_d C_E \quad, \tag{D.0.3}$$

with

$$j_d = j_{d,d} + j_{d,de} \quad , \tag{D.0.4}$$

where

$$j_{d,d} = -\partial_\xi c_d + c_d(1 - c_d - c_{de})\big[g_d(\partial_\xi c_d + \eta_d^2 \partial_\xi^3 c_d)\big] \quad , \tag{D.0.5}$$

and

$$j_{d,de} = c_d(1 - c_d - c_{de})\big[g_{de}(\partial_\xi c_{de} + \eta_{de}^2 \partial_\xi^3 c_{de})\big] \quad , \tag{D.0.6}$$

correspond to the current terms, respectively associated with the interaction between MinD-MinD proteins and MinD-MinDE complexes proteins on the membrane.

The stationary uniform values $c_d = c_d^0$, $c_{de} = c_{de}^0$ are the solution of the following equations

$$0 = -\alpha(1 - c_d - c_{de})C_D + c_d C_E \quad ,$$
$$\tag{D.0.7}$$
$$0 = -\beta c_{de} + c_d C_E \quad ,$$

i.e.

$$c_d^0 = 1 \Big/ \Big[1 + \frac{C_E}{\beta} + \frac{C_E}{\alpha C_D}\Big] \quad ,$$
$$\tag{D.0.8}$$
$$c_{de}^0 = 1 \Big/ \Big[1 + \frac{\beta}{C_E} + \frac{\beta}{\alpha C_D}\Big] \quad .$$

We notice that for $C_E = 0$ we have $c_d^0 = 1$ and $c_{de}^0 = 0$, while for $C_D = 0$, $c_d^0 = c_{de}^0 = 0$. The stability of the uniform stationary states is studied by applying a small perturbation and then linearizing the dynamic equations. Taking periodic boundary conditions, we substitute c_d and c_{de} with the expression $c_d^0 + \delta c_d \, exp(\lambda_k \tau + ik\xi)$ and $c_{de}^0 + \delta c_{de} \, exp(\lambda_k \tau + ik\xi)$ into the equations. D.0.3, where λ_k and k are the dimensionless frequency and wavenumber respectively. After linearization, we obtain the following eigenvalues equation

$$(\mathbf{A}(k) - \lambda_k \mathbf{I}) \begin{pmatrix} \delta c_d \\ \\ \delta c_{de} \end{pmatrix} = 0 \quad ,$$

that determines the dimensionless linear growth rates λ_k as a function of the dimensionless wavenumber k. The elements of the dimensionless 2×2 linearization matrix $\mathbf{A}$ are given by

$$\mathbf{A}_{11}(k) = -\alpha C_D - C_E - k^2 \Big[1 - g_d c_d^0 (1 - c_d^0 - c_{de}^0)(1 - \eta_d^2 k^2) \Big] \quad ,$$

$$\mathbf{A}_{12}(k) = -\alpha C_D - k^2 \Big[g_{de} c_d^0 (1 - c_d^0 - c_{de}^0)(1 - \eta_{de}^2 k^2) \Big] \quad ,$$

$$\mathbf{A}_{21}(k) = C_E \quad ,$$

$$\mathbf{A}_{22}(k) = -\beta \quad .$$

(D.0.9)

The correspondent characteristic equation is

$$\lambda^2 - \mathrm{Tr}(\mathbf{A})\lambda + \det(\mathbf{A}) = 0 \quad ,$$

(D.0.10)

with the solution

$$\lambda_{1,2} = \frac{\mathrm{Tr}(\mathbf{A}) \pm (\mathrm{Tr}(\mathbf{A})^2 - 4\det(\mathbf{A}))^{1/2}}{2} \quad .$$

(D.0.11)

The uniform stationary state becomes unstable with respect to spatially periodic perturbations with a dimensionless wavenumber k_c when the conditions $R(\lambda_k) = 0$ and $dR(\lambda_k)/dk^2 = 0$ are satisfied at $k = k_c$[1].

If λ_k is complex at the instability point, this is a Hopf bifurcation with broken translational symmetry. Because we have $R(\lambda_k) = \mathrm{Tr}[\mathbf{A}(k)]/2$, the conditions for such bifurcation are

$$\mathrm{Tr}\big[\mathbf{A}(k)\big] = 0, \qquad \frac{d\mathrm{Tr}\big[\mathbf{A}(k)\big]}{dk^2} = 0 \quad .$$

(D.0.12)

From this conditions we derive the dimensionless wavenumber k_H at the first unstable mode, corresponding to the Hopf bifurcation:

$$k_H^2 = \sqrt{\frac{\beta + \alpha C_D + C_E}{g_d \eta_d^2 c_d^0 (1 - c_d^0 - c_{de}^0)}} \quad .$$

(D.0.13)

---

[1] We notice that in principle not all values of k are accessible. In fact, strictly speaking, the perturbations added to the densities c_d and c_{de} are expanded in the basis $exp(ik_n\xi)$, where $k_n \sim \pi(l_d/L)n$ with n integer. Therefore, for L finite the critical value k_c will be given by the closest number to the expression $\pi(l_d/L)n$.
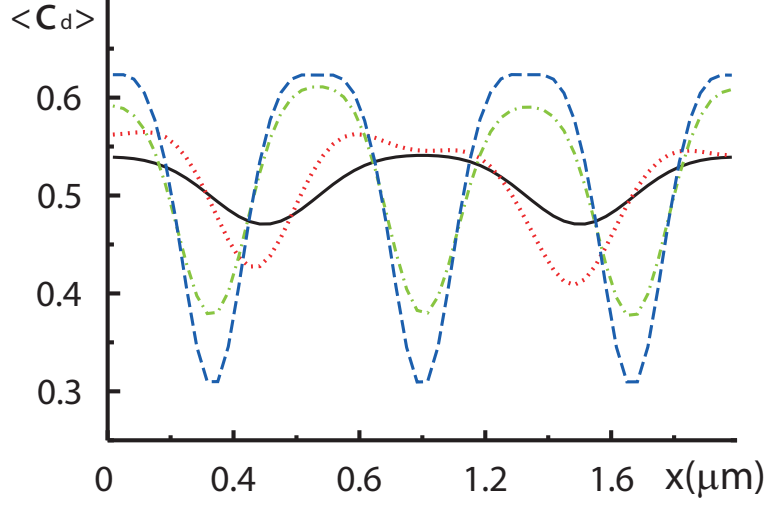
Figure D.1: The MinD distribution averaged over one temporal period $\langle c_d \rangle$, for different values of the intensity strength g_d. Increasing the interaction strength g_d, the spatial average distribution period decrease. Solid, dotted, dash-dotted and dash line refer to $g_d = 10.5$, $g_d = 12.5$, $g_d = 13.5$ and $g_d = 16$ respectively.

Therefore the wavelength of the first unstable mode in non rescaled units is

$$\Lambda_H = 2\pi \left[\frac{2g_d c_d^0 (1 - c_d^0 - c_{de}^0)}{\beta + \alpha C_D + C_E} \right]^{1/4} \sqrt{r_d l_d} \quad . \tag{D.0.14}$$

Whit the parameters α, β and C fixed, this corresponds to the following behavior

$$\Lambda_H \sim g_d^{1/4} \sqrt{r_d l_d} \quad . \tag{D.0.15}$$

The wavelength of the spatial pattern, obtained directly from integration of the equations D.0.3, doesn't follow this rule. Infact, as it is shown in figure D.1, it decreases when g_d increase. The critical frequency correspondent to Hopf bifurcation given by the imaginary part of λ_H in unrescaled units is

$$\Omega_H = \omega_E \sqrt{\det(\mathbf{A}(k_H))} = \omega_E \sqrt{\alpha C_E C_D - \beta^2} \quad . \tag{D.0.16}$$

If Ω is different from zero, oscillating solutions appear. This is the case when

$$\beta^2 < \alpha C_E C_D, \quad i.e. \quad \omega_{de}^2 < \omega_d \omega_E C_D C_E \quad . \tag{D.0.17}$$

We can estimate the value for the period T of the oscillations from $\mathrm{Im}(q_H) = 2\pi/T_H$, obtaining the value $T \simeq 80s$. The numerical study of linear stability has given the following
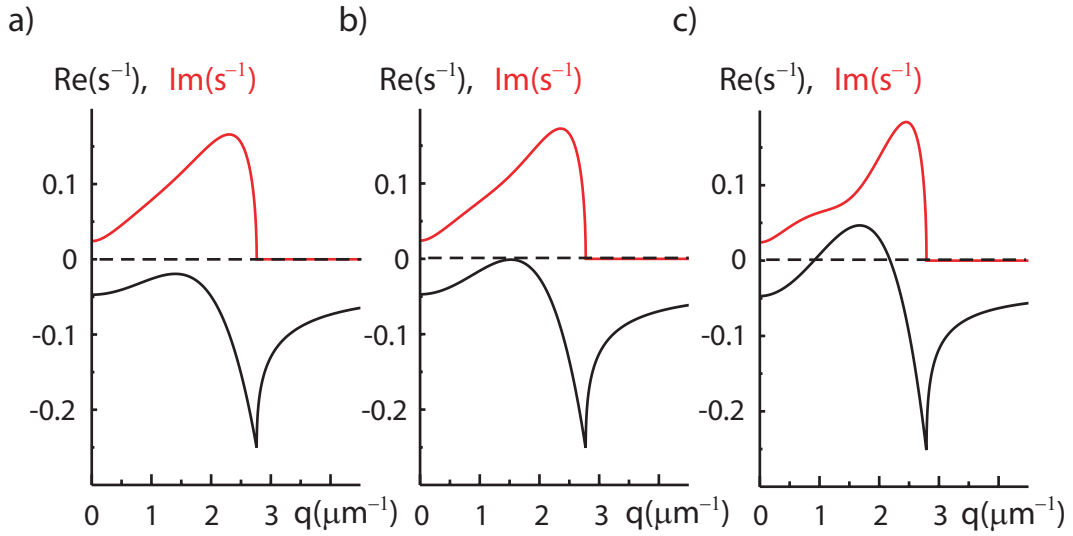
Figure D.2: Linear stability of the homogenous state. Real (Re, black line) and imaginary part (Im, red line) of the eigenvalues of the linear operator describing the dynamics of small perturbations around the homogenous state as a function of the wave number $q = k/l_d$. In (c) modes with wave numbers between $1\mu\text{m}^{-1}$ and $2.2\mu\text{m}^{-1}$ are oscillatory and unstable. The values of the parameters are $\alpha = 0.13$, $\beta = 0.13$, $\eta_d = 0.78$, $\eta_{de} = 0.05$. The interaction strength g_d take the values (a) 15, (b) 18, and (c) 25. Notice that the wavelength calculated from the value of q corresponding to the maximum for Re weakly depends on g_d and in all three cases takes the value $\Lambda \simeq 4\mu m$.

behavior: k_c increases with g_d and l_d (*i.e.* decreases when ω_E increases and increases with D_d) and decreases when r_d increases. When all other parameters are fixed the period T_H is especially sensitive to variation of β, *i.e.* ω_{de}, T_H decreases when ω_{de} increases.

In absence of the current j_d, it is easy to show that $\lambda \leq 0$. In fact, in this case

$$\lambda = \frac{1}{2}\left[- (\alpha C_D + C_E + \beta) + \sqrt{(\alpha C_D + C_E + \beta)^2 - 4C_E\beta} \right] \leq$$

$$\leq -(\alpha C_D + C_E + \beta) + \sqrt{(\alpha C_D + C_E + \beta)^2} = 0 \quad .$$

(D.0.18)

This continues to be valid for small enough values of the interaction strength g_d. In figure D.2(a) this is shown by $g_d = 15$. Figure D.2(c) shows the case when the real and imaginary parts of λ are different from zero, $g_d = 25$, implying the existence of stable oscillatory solutions. Figure D.2(b), $g_d = 18$ shows the instability point ($R(\lambda) = 0$, $k = k_H$) at the Hopf bifurcation $k_H = 0.88$ ($q_H = 1.6\mu m^{-1}$) corresponding to the value $\Lambda_H = (2\pi/k_H)l_d \simeq 4\mu m$ for the wavelength of the pattern. If we increase further the
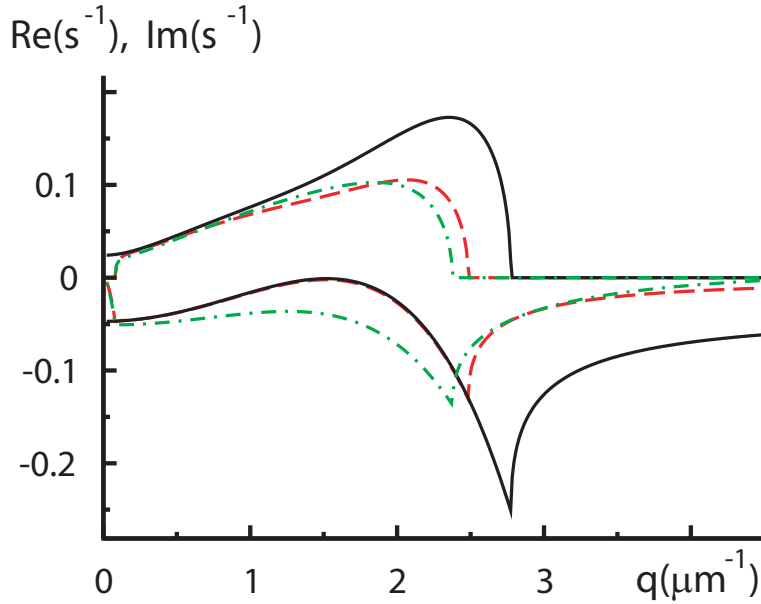
Figure D.3:   Graphs of the eigenvalue with the largest real part of the linearized time evolution operator versus the wave number $q = k/l_d$. The solid black line refers to homogenous cytosolic distributions with parameter values as in figure D.2. The red and green lines refer to a finite ATP exchange rate. Parameter values as in figure D.2 with $D_D = D_E = 15\mu m^2 s^{-1}$, $\omega_{ATP} = 0.5s^{-1}$ are depicted as red dashed lines and $\omega_{ATP} = 0.02s^{-1}$ with green dash-dot lines.

value of g_d, $\text{Im}(\lambda) \to 0$ in the range of values of k, for which $d\text{Re}(\lambda)/dk^2 = 0$, which corresponds to stationary patterns.

In regard to the interaction between Min proteins on the membrane, we consider only the two cases (i) $j_{d,d} \neq 0$, (ii) $j_{d,de} \neq 0$ and $j_{d,d} \neq 0$, with all other current terms equalling to zero. In particular, the case (i), corresponds to the assumption that when MinD attaches to the membrane and/or when MinE attaches to the membrane-bound MinD, its conformational changes neutralize the interaction between MinD and MinDE complexes. For the case (ii), the conformational changes of MinD make the interaction between complexes MinDE and MinD proteins on the membrane repulsive, *i.e.* $g_{de} < 0$. The term $j_{d,de}$ appears in the non-diagonal term of the linearized matrix $\mathbf{A}$ in a such way that it does not change the value of the critical wave number, *i.e.* the wavelength of the pattern, but only the imaginary part of the eigenvalues of $\mathbf{A}$, *i.e.* the temporal period of the oscillation. Other possible combinations, including for instance terms such as $j_{de,de}$, and/or different values for the sign of the interaction strength gs do not give rise to Hopf bifurcation.

Finally, we consider the general case of non-homogeneous cytosolic distribution and a finite rate ω_{ATP} for the rebinding of ATP to MinD after detachment from the membrane.

As figure D.3 shows, we find that for $\omega_{ATP} > 0.5s^{-1}$ the effect of a finite ATP exchange when compared with the homogeneous cytosolic distribution case, can be neglected, at least at the level of a stability study.

Appendix E

Numerical integration of PDE

Here, we recover the necessary condition for the numerical stability of our algorithm[1] used to integrate equations (3.2.3) and (3.2.4). Usually, PDE's are integrated according to one of two general schemes: finite difference methods or spectral methods. The first is usually preferred for its accuracy and stability and the second for the locality property. A combination of both was also considered [182]. The finite difference method is typically less efficient from the point of view of CPU time. This point becomes particularly important when noise terms are also considered. We chose the finite difference scheme.

The basis of finite difference methods is the discretization of the physical domain into a lattice or array of points at which the solution of the equation is computed for each time step. For the sake of simplicity we will consider only the current term associated with MinD-MinD interaction on the membrane, *i.e.* $\bar{k}_1 = \bar{k}_2 = 0$.

The discretization scheme introduces a time step Δt and a mesh size Δx. Some care has to be given to these parameters to avoid numerical instabilities. We refer to equations (D.0.3) which can be written in the general form

$$\partial_t c_d(x,t) = (\mathcal{T} + \mathcal{V}_{c_d})c_d(x,t) \quad ,$$

$$\partial_t c_{de}(x,t) = \mathcal{V}_{c_{de}}c_{de}(x,t) \quad ,$$

(E.0.1)

where $\mathcal{T}$ is one (non-linear) operator containing all the spatial derivatives and, where $\mathcal{V}_{c_d}$ and $\mathcal{V}_{c_{de}}$ are strictly (linear) local operators. The part associated with the operators $\mathcal{V}$s can be reduced to a simple ODEs and only the operator $\mathcal{T}$ has to be considered for studying numerical stability, *i.e.*

$$\partial_t c_d = \partial_x j_d \quad . \tag{E.0.2}$$

---

[1] The programs used to this end have been written in Fortran 77 language.

The discrete version of this equation, used in our numerical simulations, is

$$c_d^i(n) = c_d^i(n-1) + \frac{\Delta t}{(\Delta x)^2}\Big[j_d^{i+1}(n-1/2) - 2j_d^i(n-1/2) + j_d^{i-1} +$$

$$+ \frac{1}{(\Delta x)^2}\big(j_d^{i+2}(n-1/2) - 4j_d^{i+1}(n-1/2) + 6j_d^i(n-1/2) - \qquad \text{(E.0.3)}$$

$$-4j_d^{i-1}(n-1/2) + j_d^{i-2}(n-1/2) \big)\Big] \quad ,$$

where n is the temporal index, i the box lattice index and j_d is calculated at the mid-point $\Delta t/2$ with a Runge-Kutta algorithm. The expression for j_d^i depends on the value of $\Delta c_d^i = (c_d^{i+1} - c_d^i)$. If $\Delta c_d^i > 0$, proteins go from site $i+1$ to site i, the product $c_d(1 - c_d - c_{de})$ in the expression 3.1.5 for the current has to be written in the discrete case as $c_d^{i+1}(1 - c_d^i - c_{de}^i)$. In the opposite case, *i.e.* $\Delta c_d^i < 0$, proteins go from site i to site $i+1$, the expression $c_d^i(1 - c_d^{i+1} - c_{de}^{i+1})$ has to be considered. Finally, fictitious grid points were placed around the actual boundary of the system. The values of the concentration c^i in these points were taken to be equal to the values of c^i in the respective mirror-reflected grid points inside the lattice. Writing the equation (E.0.3) for the Fourier transform of the MinD concentration on the membrane in a lattice of size N,

$$\mathcal{C}_k = \frac{1}{N}\sum_x c_x e^{ikx} \quad , \qquad \text{(E.0.4)}$$

where the sum goes over the lattice sites, and linearizing around the steady state (c_d^0, c_{de}^0), we obtain, for the $1-$dimensional case, the following stability condition

$$1 + \Delta t\{ D_{\text{eff}}\,\Gamma(k) - G\,\Gamma^2(k) \} < -1 \quad , \qquad \text{(E.0.5)}$$

where

$$\Gamma(k) = \frac{2}{(\Delta x)^2}\big[cos(k\Delta x) - 1 \big] \qquad \text{(E.0.6)}$$

is the Fourier transform of the discrete Laplacian in a $1-$dimensional lattice, $k = 2\pi n/N\Delta x$ with $n \in [1, N]$ and

$$D_{\text{eff}} = D_d\big[1 - g_d c_d^0(1 - c_d^0 - c_{de}^0) \big] \quad ,$$

$$\qquad \text{(E.0.7)}$$

$$G = D_d g_d c_d^0(1 - c_d^0 - c_{de}^0)r_d^2 \quad .$$

The linearized version of the equation (E.0.3) is stable for all k modes when the following inequality is hold

$$\Delta t < \frac{(\Delta x)^4}{2 D_{\text{eff}} (\Delta x)^2 + 2G} \quad .$$

(E.0.8)

This is the criterion for the numerical stability of equation E.0.2. In the limit, where the interaction between MinD proteins on the membrane goes to zero, $G \rightarrow 0$ and $D_{\text{eff}} \rightarrow D_d$, the criterion for the numerical stability of the reaction-diffusion equations is recovered. From a practical point of view, it is important to take into account that the numerical stability, given the diffusion coefficient D_d and the mesh size Δx as fixed, still depends on the interaction strength g_d, on the interaction range r_d between the MinD proteins on the membrane, and on the steady state values (c_d^0, c_{de}^0). Of course, this criterion is valid near the steady state (c_d^0, c_{de}^0), thus is a condition necessary for numerical stability, nevertheless, it is not sufficient.

Appendix F

LE for homogenous cytosolic distributions

In this appendix we derive, through coarse graining of the microscopic master equation, the LEs (4.2.9) and (4.2.10) which describe the dynamics of the Min proteins for the case of large cytosolic diffusion. For the sake of the simplicity of notation the derivation is carried out in a one-dimensional system, but it can, in a direct way, be generalized in the three-dimensional case. The outline of the derivation follows [132, 159, 183] pointing out the physical meaning of the used approximations and the origin of the different terms.

The starting point is a 1-D microscopic lattice model with lattice length l_0, N total number of sites, and ε sites per unit length. Each site can either be empty or occupied by a single protein MinD or a complex MinDE, *i.e.* the multiple occupation of a site is not permitted. The probability $I(x \to x')$ in unit time Δt, that a protein MinD on the membrane jumps from a site x to a site x', is influenced by the interaction with other proteins. We assume the potential $V(x)$ experienced by the protein MinD at the site x to be composed of a superposition of pairwise interactions with the proteins nearby

$$V(x) = -\sum_{x'}^{N} \left[v_{dd}(x - x')n_d(x') + v_{dde}(x - x')n_{de}(x') \right] \quad , \tag{F.0.1}$$

where $n_d(x')$ and $n_{de}(x')$ are the occupation numbers at x' which can take the values 0 and 1. The functions $v_{dd}(x)$ and $v_{dde}(x)$ are binary potentials of the attractive interactions between MinD-MinD and MinD-MinDE, respectively. We assume that this potentials vanish over distances exceeding the characteristic respective interaction radius. We assume that it is determined according to the Metropolis dynamics, whose hopping probability

per unit time Δt depends on the difference $\Delta E = V(x') - V(x)$, *i.e.*

$$
I(x \rightarrow x') =
\begin{cases}
I_0 & \text{if } \Delta E < 0 \\
I_0 \, exp\left(\dfrac{-\Delta E}{k_B T}\right) & \text{if } \Delta E > 0,
\end{cases}
$$

where $I_0 = (D_d \Delta t / l_0^2)$ is the hopping probability of a protein MinD on the membrane in absence of interactions. We define the rates $\tilde{\omega}_{D,E} = \omega_{D,E} c_{\max}$, where $\omega_{D,E}$ are the parameters introduced in equations (3.2.3) and (3.2.4), and to simplify the notations, in the following the "tilde" will be dropped. For the protein MinD, the probability of attachment in a unit time at the site x is given by

$$
\Delta t \, \omega_D \left(\frac{N_D}{N}\right) (1 - n_d(x) - n_{de}(x)) \quad , \tag{F.0.2}
$$

for MinDE by

$$
\Delta t \omega_E \left(\frac{N_E}{N}\right) n_d(x) \quad , \tag{F.0.3}
$$

and for the detachment process of MinDE

$$
\Delta t \omega_{de} n_{de}(x) \quad . \tag{F.0.4}
$$

The parameters N_D and N_E are the total numbers of cytosolic MinD and MinE proteins, respectively. All statistical processes are assumed to be Markovian processes [184]. Using the above assumptions, we write the following microscopic master equation for the joint

probability distribution $P(\{n_d(x)\}, \{n_{de}(x)\}, t)$

$$\frac{dP}{dt} = \sum_x \omega_D \{ (\frac{N_D + 1}{N})(2 - n_d(x) - n_{de}(x))n_d(x)P(n_d(x) - 1, \{n_{de}(x)\})) \} -$$

$$- \sum_x \omega_D \{ \frac{N_D}{N}(1 - n_d(x) - n_{de}(x))[1 - n_d(x)]P \} +$$

$$+ \sum_x \omega_E \{ (\frac{N_E + 1}{N})(1 + n_d(x))n_{de}(x)P(n_d(x) + 1, n_{de}(x) - 1) - E_N n_d(x)[1 - n_{de}(x)]P \} +$$

$$+ \sum_x \omega_{de} \{ (1 + n_{de}(x))[1 - n_{de}(x)]P(n_d(x), n_{de} + 1) - n_{de}(x)P \} +$$

$$+ \sum_{x,x'} I(x' \to x) \{ (n_d(x') + 1)(2 - n_d(x) - n_{de}(x))n_d(x)P(n_d(x) - 1, n_d(x') + 1, \{n_{de}(x)\})) \} -$$

$$- \sum_{x,x'} I(x \to x') \{ (2 - n_d(x') - n_{de}(x'))[1 - n_d(x)]P \} \quad,$$

$$(F.0.5)$$

The summation over x' in the last term includes only sites that represent nearest neighbors of site x. The notations $P(n_d(x) - 1, \{n_{de}\})$, $P(\{n_d\}, n_{de}(x) + 1)$, mean that the set of occupation number $\{n_d(x)\}$, $\{n_{de}(x)\}$ differs from that in the distribution P, where $P \equiv P(\{n_d\}, \{n_{de}\}, t)$, only at location x, where n_d is and n_{de}, are respectively, decreased and increased by one. $P(n_d(x) + 1, n_{de}(x) - 1, t)$ denotes the probability distribution for the case in which $n_d(x)$ and $n_{de}(x)$ are increased respectively decreased by one. $P(n_d(x) - 1, n_d(x') + 1, \{n_{de}(x)\})$ is the probability distribution identical to P except for a MinD-protein shifted from x to x'.

Now, we introduce the coarse-grained description. The system is divided into m boxes, each containing a large number of sites $n_{\max}$, and with length l_b chosen to be smaller than the characteristic length of the spatial patterns which appear. This length characterizes the resolution of our system, complete diffusional mixing is assumed to take place in each box.

Because of the complete mixing, the size of the box should also be smaller than the interaction range r, i.e. that r must be relatively large. Nevertheless, it was shown [185] that the mesoscopic theory describes the concentration profiles in the steady state quantitatively well, also for potentials with relatively short interaction range. Therefore, although the mesoscopic theory is not fully justified in the case of few lattice length for the

interaction range, like was considered for the interaction range r_{de}, it can still be used in this case for qualitative insights.

For each box j the probability P of attachment in a time step Δt is given by

$$P_{D \to d} = \Delta t\, \omega_D \left(\frac{N_D}{m} \right) \left(1 - \frac{n_{d,j} + n_{de,j}}{n_{\max}} \right) \quad , \tag{F.0.6}$$

$$P_{E \to de} = \Delta t\, \omega_E \left(\frac{N_E}{m} \right) \frac{n_{d,j}}{n_{\max}} \quad , \tag{F.0.7}$$

for MinD and MinE respectively, and

$$P_{de \to E+D} = \Delta t\, \omega_{de} n_{de,j} \quad , \tag{F.0.8}$$

for the detachment process of MinDE. The variables $n_{d,j}$ and $n_{de,j}$, are, respectively the number of MinD and MinDE proteins in each box j.

The probabilities $P(j \to j \pm 1)$ at each time step, for a transition between the neighboring boxes for the MinD proteins are proportional to the number $n_{d,j}$ of proteins in the jth box and to the fraction $1 - (n_{d,j\pm1} + n_{de,j\pm1})/n_{\max}$ of empty sites in the neighboring box. Furthermore, it depends on the interaction between membrane-bound proteins, and we write:

$$P_{j \to j\pm1} = n_{d,j} \left(1 - \frac{n_{d,j\pm1} + n_{de,j\pm1}}{n_{\max}} \right) I_j^{\pm} \quad , \tag{F.0.9}$$

where

$$I_j^{\pm} = \begin{cases} I_0 & \text{if } \Delta E_j < 0 \\ I_0\, exp\!\left(\dfrac{-\Delta E_j}{k_B T} \right) & \text{if } \Delta E_j > 0 \end{cases} \quad , \tag{F.0.10}$$

where $I_0 = D_d\, \Delta t / l_b^2$, $\Delta E_j = V_{j\pm1} - V_j$, and we assume that the potential $V(x)$ does not change inside the box j, and therefore can be specified by a certain value V_j.

The master equation for the multidimensional distribution $p(\{n_{d,1}, \ldots, n_{d,m}\}, \{n_{de,1}, \ldots, n_{de,m}\}, t)$, which gives the probability of finding $n_{d,1}, \ldots, n_{d,m}$ and $n_{de,1}, \ldots, n_{de,m}$ proteins MinD or MinDE, respectively in the boxes positioned at

$x_1, \ldots, x_m$ at the time t, takes the following shape:

$$\frac{dp}{dt} = \sum_j \omega_D \left[\left(\frac{N_D + 1}{m} \right) (n_{\max} - n_{d,j} - n_{de,j} + 1) \, p_{d,j}^- \right] -$$

$$- \sum_j \omega_D \left[\left(\frac{N_D}{m} \right) (n_{\max} - n_{d,j} - n_{de,j}) \, p \right] +$$

$$+ \sum_j \omega_E \left[\left(\frac{N_E + 1}{m} \right) (n_{d,j} + 1) \, p_j^{\pm} - \left(\frac{N_E}{m} \right) n_{d,j} p \right] +$$

$$+ \sum_j \omega_{de} \left[(n_{de,j} + 1) \, p_{de,j}^+ - n_{de,j} p \right] +$$

$$+ \sum_j \left[I_{j-1}^+ (n_{d,j-1} + 1) \, \hat{p}_{j-1}^+ + I_{j+1}^- (n_{d,j+1} + 1) \, \hat{p}_{j+1}^- \right] \left(1 - \frac{n_{d,j} + n_{de,j} - 1}{n_{\max}} \right) -$$

$$- \sum_j \left[I_j^+ \left(1 - \frac{n_{d,j+1} + n_{de,j+1}}{n_{\max}} \right) + I_j^- \left(1 - \frac{n_{d,j-1} + n_{de,j-1}}{n_{\max}} \right) \right] n_{d,j} p \quad .$$

$$(\text{F.0.11})$$

Where the sum over j goes from 1 to m, and the following short notations were used:

$$p_{d,j}^- = p(n_{d,j} - 1, \{n_{de}\}, t) \quad ,$$

$$p_j^{\pm} = p(n_{d,j} + 1, n_{de} - 1, t) \quad ,$$

$$p_{de,j}^+ = p(\{n_{d,j}\}, n_{de} + 1, t) \quad , \qquad (\text{F.0.12})$$

$$\hat{p}_j^+ = p(n_{d,j} + 1, n_{d,j+1} - 1, \{n_{de}\}, t) \quad ,$$

$$\hat{p}_j^- = p(n_{d,j-1} - 1, n_{d,j} + 1, \{n_{de}\}, t) \quad .$$

To simplify the recognition of the last terms in equation (F.0.12), we schematically represent the probability fluxes for the jth box as follows

$$[j-1] \xrightarrow{I_{j-1}^+} [j] \xrightarrow{I_j^+} [j+1] \quad , \qquad (\text{F.0.13})$$

$$[j-1] \xleftarrow{I_j^-} [j] \xleftarrow{I_{j+1}^-} [j+1] \quad . \qquad (\text{F.0.14})$$

Now, we introduce the symmetric and antisymmetric probability fluxes

$$s_j = \frac{I_j^+ + I_j^-}{2} \quad , \tag{F.0.15}$$

and

$$a_j = \frac{I_j^+ - I_j^-}{2} \quad , \tag{F.0.16}$$

associated with the hopping rates. After shifting the summation index in the fifth sum, the

master equation (F.0.11) takes the form

$$
\frac{dp}{dt} = \sum_j \omega_D \left[\left(\frac{N_D + 1}{m} \right) (n_{\max} - n_{d,j} - n_{de,j} + 1) \, p_{d,j}^- \right]
$$

$$
- \sum_j \omega_D \left[\left(\frac{N_D}{m} \right) (n_{\max} - n_{d,j} - n_{de,j}) \, p \right]
$$

$$
+ \sum_j \omega_E \left[\left(\frac{N_E + 1}{m} \right) (n_{d,j} + 1) \, p_j^\pm - \left(\frac{N_E}{m} \right) n_{d,j} p \right]
$$

$$
+ \sum_j \omega_{de} \left[(n_{de,j} + 1) \, p_{de,j}^+ - n_{de,j} p \right]
$$

$$
+ \sum_j s_j (n_{d,j} + 1) \left[\left(1 - \frac{n_{d,j+1} + n_{de,j+1} - 1}{n_{\max}} \right) \hat{p}_j^+ \right]
$$

$$
+ \sum_j s_j (n_{d,j} + 1) \left[\left(\frac{n_{d,j-1} + n_{de,j-1} - 1}{n_{\max}} \right) \hat{p}_j^- \right] \tag{F.0.17}
$$

$$
- \sum_j s_j n_{d,j} \left(2 - \frac{n_{d,j+1} + n_{de,j+1} + n_{d,j-1} + n_{de,j-1}}{n_{\max}} \right) p
$$

$$
+ \sum_j a_j (n_{d,j} + 1) \left[\left(1 - \frac{n_{d,j+1} + n_{de,j+1} - 1}{n_{\max}} \right) \hat{p}_j^+ \right]
$$

$$
- \sum_j a_j (n_{d,j} + 1) \left[\left(1 - \frac{n_{d,j-1} + n_{de,j-1} - 1}{n_{\max}} \right) \hat{p}_j^- \right]
$$

$$
+ \sum_j a_j n_{d,j} \left(\frac{n_{d,j+1} + n_{de,j+1} + n_{d,j-1} + n_{de,j-1}}{n_{\max}} \right) p \quad .
$$

We assume that the number of lattice sites $n_{\max}$ in each box is much larger than one. Introducing the local quantities $c_{d,j} = n_{d,j}/n_{\max}$, and $c_{de,j} = n_{de,j}/n_{\max}$ and taking into account that their value changes only a little as a result of a single attachment, detachment, or hopping event, we can consider the following Taylor expansion in the parameter

$1/n_{\max}$

$$p_{d,j}^{-} \approx P - \frac{1}{n_{\max}}\frac{\partial P}{\partial c_{d,j}} + \frac{1}{2n_{\max}^2}\frac{\partial^2 P}{\partial c_{d,j}^2} \quad ,$$

$$p_j^{\pm} \approx P + \frac{1}{n_{\max}}\left(\frac{\partial P}{\partial c_{d,j}} - \frac{\partial P}{\partial c_{de,j}}\right) + \frac{1}{2n_{\max}^2}\left(\frac{\partial^2 P}{\partial c_{d,j}^2} + \frac{\partial^2 P}{\partial c_{de,j}^2}\right) +$$

$$+ \frac{1}{2n_{\max}^2}\left(2\frac{\partial^2 P}{\partial c_{d,j}\partial c_{de,j}}\right) \quad ,$$

$$p_{de,j}^{+} \approx P + \frac{1}{n_{\max}}\frac{\partial P}{\partial c_{de,j}} + \frac{1}{2n_{\max}^2}\frac{\partial^2 P}{\partial c_{de,j}^2} \quad ,$$

(F.0.18)

$$\hat{p}_j^{+} \approx P + \frac{1}{n_{\max}}\left(\frac{\partial P}{\partial c_{d,j}} - \frac{\partial P}{\partial c_{d,j+1}}\right) + \frac{1}{2n_{\max}^2}\left(\frac{\partial^2 P}{\partial c_{d,j}^2} + \frac{\partial^2 P}{\partial c_{d,j+1}^2}\right) +$$

$$+ \frac{1}{2n_{\max}^2}\left(2\frac{\partial^2 P}{\partial c_{d,j}\partial c_{d,j+1}}\right) \quad ,$$

$$\hat{p}_j^{-} \approx P + \frac{1}{n_{\max}}\left(\frac{\partial P}{\partial c_{d,j}} - \frac{\partial P}{\partial c_{d,j-1}}\right) + \frac{1}{2n_{\max}^2}\left(\frac{\partial^2 P}{\partial c_{d,j-1}^2} + \frac{\partial^2 P}{\partial c_{d,j}^2}\right) +$$

$$+ \frac{1}{2n_{\max}^2}\left(2\frac{\partial^2 P}{\partial c_{d,j-1}\partial c_{d,j}}\right) \quad ,$$

where P is the distribution function $P(c_{d,j}, c_{de,j}, t)$. Substituting these approximations into equation F.0.17 and keeping the terms up to the order $1/n_{\max}$, we get a multidimensional Fokker-Planck equation for the joint probability distribution P.

Since, the length of the box l_b is much smaller than the minimal characteristic scale of the spatial pattern, we can assume that the quantities $c_{d,j}$ and $c_{de,j}$ do not significantly change between the neighboring boxes and can be defined as continuous functions of the space: $c_d(x,t)$ and $c_{de}(x,t)$. Consequently, a continuous version of the multivariate Fokker-Planck equation can be introduced, and the joint probability distribution $P(c_{d,j}, c_{de,j}, t)$ converts to the functional $P([c_d(x)], [c_{de}(x)], t)$ that gives the probability density of different random realizations of the protein concentrations.

After the transformation to continuous coordinates, we can approximate the symmet-

ric and antisymmetric probability fluxes s_j and a_j as functions of the spatial coordinate x, which are given by the following expression

$$s(x) = \frac{I_0}{2}\left[1 + exp\left(-\frac{l_b}{k_BT}|\partial V/\partial x|\right)\right] \quad,$$

$$a(x) = -\frac{I_0}{2}\left[1 - exp\left(-\frac{l_b}{k_BT}|\partial V/\partial x|\right)\right] sign\left(\frac{\partial V}{\partial x}\right) \quad.$$

(F.0.19)

In the limit when $\nu \equiv l_b|\partial V/\partial x| \to 0$, we obtain

$$\lim_{\nu\to 0}\left(s(x)l_b^2\right) = D_d \quad,$$

(F.0.20)

where D_d is defined by

$$D_d = \lim_{l_b\to 0}\left(I_0 l_b^2\right)$$

(F.0.21)

and

$$\lim_{\nu\to 0}(a(x)l_b) = \lim_{\nu\to 0}\left(-\frac{I_0 l_b^2}{2k_BT}\frac{\partial V}{\partial x}\right) = -\frac{1}{2}\frac{D_d}{k_BT}\frac{\partial V}{\partial x}$$

(F.0.22)

Taking the evolution equation for the functional $P([c_d(x)], [c_{de}(x)], t)$ in the limit $\nu \equiv l_b|\partial V/\partial x| \to 0$ and performing certain transformations of the transport terms (cfr. refer-

ences [132, 159]), we obtain the functional Fokker-Planck equation

$$\frac{\partial P}{\partial t} = -\int dx \frac{\delta}{\delta c_d(x)} \left\{ [\omega_D C_D \left(1 - c_d(x) - c_{de}(x)\right) - \omega_E C_E c_d(x) + \right.$$

$$+ \left. \frac{D_d}{k_B T} \frac{\partial}{\partial x} \left(1 - c_d(x) - c_{de}(x) \frac{\partial V}{\partial x}\right) + \frac{\partial^2 c_d(x)}{\partial x^2} \right] P \right\} +$$

$$- \int dx \frac{\delta}{\delta c_{de}(x)} \left\{ [\omega_D C_D \left(1 - c_d(x) - c_{de}(x)\right) - \omega_{de} c_{de}(x)] P \right\} +$$

$$+ \frac{\Omega}{2} \int \int dx dx' \frac{\delta^2}{\delta c_d(x) \delta c_d(x')} \left\{ \left[\left(\omega_D C_D \left(1 - c_d(x) - c_{de}(x)\right) \right. \right. + \right. \tag{F.0.23}$$

$$+ \left. \omega_E C_E c_d(x)\right) \delta(x - x') + \frac{\partial^2}{\partial x \partial x'} \left(2D_d(1 - c_d(x) - c_{de}(x))\right) \delta(x - x') \right] P \right\} +$$

$$+ \frac{\Omega}{2} \int \int dx dx' \frac{\delta^2}{\delta c_{de}(x) \delta c_{de}(x')} \left\{ (\omega_{de} c_{de}(x) + \omega_E C_E c_d) \delta(x - x') P \right\} +$$

$$- \frac{\Omega}{2} \int \int dx dx' \left[\frac{\delta^2}{\delta c_d(x) \delta c_{de}(x')} + \frac{\delta^2}{\delta c_d(x') \delta c_{de}(x)} \right] (\omega_E C_E c_d \delta(x - x') P) \quad ,$$

where $\Omega = l_b/n_{\max} = L/N = 1/c_{\max}$.

As follows from the theory of random processes (cfr. references [152, 159]) this Fokker-Planck equation is equivalent to the SPDEs

$$\partial_t c_d = \omega_D C_D(1 - c_d - c_{de}) - \omega_E C_E c_d - \partial_x j_d$$
$$+ \xi_d(x, t) \quad , \tag{F.0.24}$$

$$\partial_t c_{de} = -\omega_{de} c_{de} + \omega_E C_E c_d + \xi_{de}(x, t) \quad , \tag{F.0.25}$$

The noise terms $\xi_d(r, t)$ and $\xi_{de}(r, t)$ take into account internal fluctuations of attach-

ment, detachment, and transport processes, and have the form

$$
\begin{aligned}
\xi_d(x,t) \;=\; & \Omega^{1/2}\sqrt{\omega_D C_D(1-c_d-c_{de})}\,\alpha_D(x,t) + \\[2mm]
& + \Omega^{1/2}\sqrt{\omega_{de} C_E c_d}\,\alpha_E(x,t) + \\[2mm]
& + \Omega^{1/2}\partial_x\!\left(\sqrt{2D_d c_d(1-c_d-c_{de})}\,\beta(x,t)\right) \quad,
\end{aligned}
\tag{F.0.26}
$$

$$
\xi_{de}(x,t) \;=\; \Omega^{1/2}\left(\sqrt{\omega_{de}c_{de}}\,\alpha_{de}(x,t) - \sqrt{\omega_E C_E c_d}\,\alpha_E(x,t)\right) \quad,
\tag{F.0.27}
$$

where $\alpha_D(x,t)$, $\alpha_E(x,t)$, $\alpha_{de}(x,t)$, associated with attachment and detachment processes, and $\beta(x,t)$ associated with transport processes, are independent white noises of unit intensity, and the Itô interpretation of the SPDE was chosen. The current j_d has the following form

$$
j_d = \left[\frac{D_d}{k_B T}c_d(1-c_d-c_{de})\frac{\partial V}{\partial x}\right] + D_d\frac{\partial c_d}{\partial x} \quad.
\tag{F.0.28}
$$

In the approximations considered in section 4.2.2 this current take the form (4.2.38) and the equations (F.0.24) and (F.0.25) correspond to the LEs (4.2.9) and (4.2.10).

Appendix G

LE for the 0-dimensional system

In this appendix, we will derive the LEs for the four protein concentrations c_d, c_{de}, c_D and c_E in the case of the 0-dimensional system and for the same attachment and detachment processes described by the probabilities (F.0.6), (F.0.7) and (F.0.8) given in appendix F, with the difference that now $m = 1$, i.e. there is only one box and no spatial degrees of freedom are taken into account and thus $n_{\max} = N$. These LEs will then be used in order to compare the relative fluctuations of the cytosolic protein concentrations with the relative fluctuations of the membrane-bound protein concentrations.

The microscopic master equation for the joint probability $P \equiv P(n_d, n_{de}, n_D, n_E, t)$ that gives the probability for finding n_d, n_{de}, n_D and n_E proteins at time t, in this case is

$$
\begin{aligned}
\frac{dP}{dt} = &-\left[\omega_D n_D\left(1 - \frac{n_d + n_{de}}{N}\right) + \omega_E n_E \frac{n_d}{N} + \omega_{de} n_{de}\right] P \\
&+ \omega_D\left(n_D + 1\right)\left(1 - \frac{n_d - 1 + n_{de}}{N}\right) P(n_d - 1, n_{de}, n_D + 1, n_E, t) + \\
&+ \omega_E(n_E + 1)\left(\frac{n_d + 1}{N}\right) P(n_d + 1, n_{de} - 1, n_D, n_E + 1, t) + \\
&+ \omega_{de}\left(n_{de} + 1\right) P(n_d, n_{de} + 1, n_D - 1, n_E - 1, t) \quad .
\end{aligned}
\tag{G.0.1}
$$

The notation $P(n_d - 1, n_{de}, n_D + 1, n_E, t)$ means that the set numbers n_D, n_d, differ from those in the distribution P, because they are increased and decreased by one, respectively. $P(n_d + 1, n_{de} - 1, n_D, n_E + 1, t)$ denotes the probability distribution for the case when n_E and n_d are increased by one and n_{de} is decreased by one. Finally, $P(n_d, n_{de} + 1, n_D - 1, n_E - 1, t)$ denotes the probability distribution for the case in which n_D and n_E are decreased by one and n_{de} is increased by one. The following short nota-

tions are introduced

$$P_d^D = P(n_D + 1, n_E, n_d - 1, n_{de}, t) \quad ,$$

$$P_{de}^{E,d} = P(n_D, n_E + 1, n_d + 1, n_{de} - 1, t) \quad , \tag{G.0.2}$$

$$P_{D,E}^{de} = P(n_D - 1, n_E - 1, n_d, n_{de} + 1, t) \quad .$$

Similar to the two variables model, the following variables are introduced, $c_d = n_d/N$, $c_{de} = n_{de}/N$, $\tilde{c}_D = n_D/N_{\text{cyt}} = n_D/N\theta$ and $\tilde{c}_E = n_E/N_{\text{cyt}} = n_E/N\theta$, where we assumed that the number of available sites in the cytosol, N_{cyt}, is the same for MinD and MinE proteins, and θ is a geometrical factor of proportionality between the number of sites on the membrane and in the cytosol. In this way, the values of the four concentrations go from 0 to 1, allowing for a comparison between their relative fluctuations.

Taking into account that the value of these variables changes only a little as a result of an attachment event [1], we can write the following expansion in the parameters $1/N$

$$P_d^D \approx P + N^{-1}\left\{\frac{1}{\theta}\frac{\partial P}{\partial c_D} - \frac{\partial P}{\partial c_d}\right\} + \frac{1}{2}N^{-2}\left\{\frac{1}{\theta^2}\frac{\partial^2 P}{\partial c_D^2} + \frac{\partial^2 P}{\partial c_d^2} - \frac{2}{\theta}\frac{\partial^2 P}{\partial c_d\partial c_D}\right\}$$

$$P_{de}^{E,d} \approx P + N^{-1}\left\{\frac{1}{\theta}\frac{\partial P}{\partial c_E} + \frac{\partial P}{\partial c_d} - \frac{\partial P}{\partial c_{de}}\right\} + \frac{1}{2}N^{-2}\left\{\frac{1}{\theta^2}\frac{\partial^2 P}{\partial c_E^2} + \frac{\partial^2 P}{\partial c_d^2} + \right.$$

$$\left. +\frac{2}{\theta}\frac{\partial^2 P}{\partial c_d\partial c_E} - \frac{2}{\theta}\frac{\partial^2 P}{\partial c_E\partial c_{de}} - 2\frac{\partial^2 P}{\partial c_d\partial c_{de}} + \frac{\partial^2 P}{\partial c_{de}^2}\right\} \tag{G.0.3}$$

$$P_{D,E}^{de} \approx P + N^{-1}\left\{\frac{\partial P}{\partial c_{de}} - \frac{1}{\theta}\frac{\partial P}{\partial c_D} - \frac{1}{\theta}\frac{\partial P}{\partial c_E}\right\} + \frac{1}{2}N^{-2}\left\{\frac{1}{\theta^2}\frac{\partial^2 P}{\partial c_D^2} + \frac{1}{\theta^2}\frac{\partial^2 P}{\partial c_E^2} + \right.$$

$$\left. +\frac{2}{\theta^2}\frac{\partial^2 P}{\partial c_D\partial c_E} - \frac{2}{\theta}\frac{\partial^2 P}{\partial c_E\partial c_{de}} - \frac{2}{\theta}\frac{\partial^2 P}{\partial c_D\partial c_{de}} + \frac{\partial^2 P}{\partial c_{de}^2}\right\} \quad .$$

Substituting these approximations into (G.0.1) and retaining there the terms up to the order $1/N$, we obtain the following Fokker-Planck equation

$$\partial_t P(\vec{c}, t) = -\partial_\nu F^\nu(\vec{c}, t)P(\vec{c}, t) + \frac{1}{2N}\partial_\nu\partial_\mu D^{\nu\mu}(\vec{c}, t)P(\vec{c}, t) \quad , \tag{G.0.4}$$

---

[1] In the coarse graining procedure this hypotesis is applied on the length scale of the box length l_b and is still valid because we consider $n_{\max} \gg 1$ in each box.

where we introduced $\vec{c} = (c_d, c_{de}, c_D, c_E)$ to simplify the notation, $\nu = d, de, D, E$ and $\mu = d, de, D, E$, F^ν is a $\nu-$component of a vector

$$|\mathbf{F}\rangle = \begin{pmatrix} \theta(f_D - f_E) \\ \theta f_E - f_{de} \\ -f_D + f_{de}/\theta \\ -f_E + f_{de}/\theta \end{pmatrix} \quad ,$$

and $\boldsymbol{D}$ is a matrix 4×4

$$\mathbf{D} = \begin{pmatrix} \theta(f_D + f_E) & -\theta f_E & -f_D & -f_E \\ -\theta f_E & \theta f_E + f_{de} & -f_{de}/\theta & f_E - f_{de}/\theta \\ -f_D & -f_{de}/\theta & f_D/\theta + f_{de}/\theta^2 & f_{de}/\theta^2 \\ -f_E & f_E - f_{de}/\theta & f_{de}/\theta^2 & f_E/\theta + f_{de}/\theta^2 \end{pmatrix} \quad ,$$

with

$$\begin{aligned} f_D &= \omega_D \tilde{c}_D (1 - c_d - c_{de}) \quad , \\ f_E &= \omega_E c_d \tilde{c}_E \quad , \\ f_{de} &= \omega_{de} c_{de} \quad . \end{aligned} \tag{G.0.5}$$

Where for the sake of simplicity we did not write $\tilde{f}_D$ and $\tilde{f}_E$ we have just to remember that they scale like $1/N_{\text{cyt}}$. Now, let us consider the following LEs

$$\partial_t c_d = \theta(f_D - f_E) + \sqrt{\frac{\theta}{N}}\left(\sqrt{f_D}\alpha_D(t) + \sqrt{f_E}\alpha_E(t)\right) \quad , \tag{G.0.6}$$

$$\partial_t c_{de} = \theta f_E - f_{de} + \frac{1}{\sqrt{N}}\sqrt{f_{de}}\alpha_{de}(t) - \sqrt{\frac{\theta}{N}}\sqrt{f_E}\alpha_E(t) \quad , \tag{G.0.7}$$

$$\partial_t \tilde{c}_D = -f_D + \frac{f_{de}}{\theta} - \frac{1}{\sqrt{\theta N}}\sqrt{f_D}\alpha_D(t) - \frac{1}{\theta\sqrt{N}}\sqrt{f_{de}}\alpha_{de}(t) \quad , \tag{G.0.8}$$

$$\partial_t \tilde{c}_E = -f_E + \frac{f_{de}}{\theta} - \frac{1}{\sqrt{\theta N}}\sqrt{f_E}\alpha_E(t) - \frac{1}{\theta\sqrt{N}}\sqrt{f_{de}}\alpha_{de}(t) \quad . \tag{G.0.9}$$

First we observe that the first two of these equations correspond to the LEs derived in section 4.2.1 once we take into account that there $C_D \sim (1/N)$ and here $c_D \sim (1/N_{\text{cyt}})$. Second we will now show that they correspond to the FPE (G.0.4). Let us write the four LEs (G.0.6), (G.0.7), (G.0.8) and (G.0.9) in the following compact form

$$\frac{dc^\nu}{dt} = f^\nu(\vec{c}) + \frac{1}{\sqrt{N}}b_i^\nu(\vec{c}, t)\alpha_i(t) \quad , \tag{G.0.10}$$

where $(\nu = d, de, D, E)$, and $(i = D, E, de)$, *i.e.* four equations with three independent sources of white Gaussian noise. The notation $\vec{c} = (c_d, c_{de}, c_D, c_E)$ is introduced, f^ν is a $\nu-$component of the vector

$$|\mathbf{f}\rangle = \begin{pmatrix} \theta(f_D - f_E) \\ \theta f_E - f_{de} \\ -f_D + f_{de}/\theta \\ -f_E + f_{de}/\theta \end{pmatrix} \quad ,$$

and b_i are the following vectors

$$|\mathbf{b_D}\rangle = \sqrt{\frac{f_D}{\theta}} \begin{pmatrix} \theta \\ 0 \\ -1 \\ 0 \end{pmatrix} \quad , \quad |\mathbf{b_E}\rangle = \sqrt{\frac{f_E}{\theta}} \begin{pmatrix} \theta \\ -\theta \\ 0 \\ -1 \end{pmatrix} \quad , \quad |\mathbf{b_{de}}\rangle = \frac{\sqrt{f_{de}}}{\theta} \begin{pmatrix} 0 \\ \theta \\ -1 \\ -1 \end{pmatrix} .$$

If we interpret the equation (G.0.10) in the Itô sense, a process described by the equation (G.0.10) can be equivalentely described by the FPE for the probability density of $\vec{c}$

$$\partial_t P(\vec{c}, t) = -\partial_\nu \widetilde{F}^\nu(\vec{c}, t) P(\vec{c}, t) + \frac{1}{2N} \partial_\nu \partial_\mu \widetilde{D}^{\nu\mu}(\vec{c}, t) P(\vec{c}, t) \quad , \tag{G.0.11}$$

a priori different from (G.0.4). The diffusion matrix $\widetilde{D}$ is related to the noise coefficients b_i^ν by

$$\widetilde{D} = |b_i\rangle\langle b_i| \quad , \tag{G.0.12}$$

and the drift components F^ν are related to the deterministic terms f^ν by

$$\widetilde{F}^\nu = f^\nu \quad . \tag{G.0.13}$$

Therefore, $\widetilde{F}^\nu = f^\nu \Rightarrow |\widetilde{\mathbf{F}}\rangle = |\mathbf{F}\rangle$, and it is easy to control that $\widetilde{D}$ correspond exactly to D.

Remark

In the previous derivation, we used the hypothesis that the noise has a Gaussian distribution, which is a good approximation when a high number of proteins is considered. In our specific case, especially when the spatial extension of the system is taken into

account, a more suitable description of the noise associated with the attachment and detachment process is achieved through a Poisson distribution.

Let us go back to the equations (G.0.6), (G.0.7), (G.0.8) and (G.0.9). We just showed that they are the LEs for the cytosolic and membrane-bound protein concentrations in the 0-dimensional case. They show that the cytosolic relative fluctuations are suppressed when the parameter $\theta \gg 1$, i.e. when $N_{\text{cyt}} \gg N$. In other words, the bigger 'volume' available to the cytosolic protein when compared with the 'one' available to the membrane-bound proteins lower the cytosolic relative fluctuations when compared with the membrane-bound relative fluctuations. Here, the word volume means the maximum possible number of proteins in the two possible states, namely the cytosolic and the membrane-bound one. When space is taken into account, this word assumes its own actual meaning. Concerning the absolute values of the fluctuations they are exactly the same, in the cytosol and on the membrane, for each one of the attachment-detachment process by formulation.

Finally, we notice that, if all four protein concentrations scale in the same way, for example like $1/N$, the LEs take the following simple form

$$\partial_t c_d = f_D - f_E + \frac{1}{\sqrt{N}}\left(\sqrt{f_D}\alpha_D(t) + \sqrt{f_E}\alpha_E(t)\right) \quad, \tag{G.0.14}$$

$$\partial_t c_{de} = f_E - f_{de} + \frac{1}{\sqrt{N}}\sqrt{f_{de}}\alpha_{de}(t) - \frac{1}{\sqrt{N}}\sqrt{f_E}\alpha_E(t) \quad, \tag{G.0.15}$$

$$\partial_t c_D = -f_D + f_{de} - \frac{1}{\sqrt{N}}\sqrt{f_D}\alpha_D(t) - \frac{1}{\sqrt{N}}\sqrt{f_{de}}\alpha_{de}(t) \quad, \tag{G.0.16}$$

$$\partial_t c_E = -f_E + f_{de} - \frac{1}{\sqrt{N}}\sqrt{f_E}\alpha_E(t) - \frac{1}{\sqrt{N}}\sqrt{f_{de}}\alpha_{de}(t) \quad. \tag{G.0.17}$$

From these equations, the equations (4.2.9) and (4.2.10), and assuming that each one of the reaction and diffusion processes make an independent contribution to the noise terms, the LEs for the one-dimensional non-homogenous cytosolic distributions case can be obtained directly.

Appendix H

Estimation of parameter values

Here, we give an estimation of some of the parameters used in the theoretical description, and which values are not available experimentally. In particular, we consider the maximum density $c_{\max}$ and the interaction strengths Us and range rs. Even if N_D and N_E were approximately evaluated experimentally [110], until now there are no experimental values for N. Depending on the actual scenario, such a measurement can be very difficult or very simple. If the Min-proteins can attach everywhere on the membrane, then N can be estimated straightforward from the area of the membrane surface. If the MinD-proteins really make helices and these helices are a fixed framework on the membrane, N can be estimated from an evaluation of the lenght of such helices, for instance from the pictures in [68]. This was our choice. Other situations are possible as, for example, the possibility that MinD can attach only to some specific receptor on the membrane and they can have, as we know so far, different distributions. Making the assumption that only one protein can attach on each site of the spiral structure, we can estimate the parameter N

$$N = L/l_0 \approx [2\pi a \times (\text{winding rounds number}) + L_C]/l_0 \quad , \tag{H.0.1}$$

where a is the cell radius, L_C the cell length, l_p the proteins size and L is the effective length of our system. From the experimental values [66, 186]

$$
\begin{aligned}
L_{\mathrm{C}} &\approx 2\mu\mathrm{m} \quad , \\
a &\approx 0.5\mu\mathrm{m} \quad , \\
l_0 &\approx l_{\mathrm{p}} \sim (3.5 - 5.7) n\mathrm{m} \quad , \\
\text{winding rounds number} &\approx 5 - 6 \quad ,
\end{aligned}
\tag{H.0.2}
$$

we can estimate $N = (1500 - 15000)$. The bigger value comes from the hypothesis that there are two helices and the proteins can attach to the membrane one next to other. The smaller value results from considering only one helical and only the half length available

to the attachment process[1]. In our simulations, we always use $N = 2000$ for a cell long 2μm, which corresponds to $c_{\max} = L/N = 1000\mu$m^{-1}. The order of magnitude for the value of the interaction strenght U is (see for example [190]).

$$U \approx 10 k_B T \quad . \tag{H.0.3}$$

For the interaction ranges, assuming electrostatic interaction we can consider

$$r \approx 10 n\text{m} \quad . \tag{H.0.4}$$

As was discussed in section 4.3, the value used in our simulation for the MinD-MinD interaction range was much larger than this.

---

[1]Another point to be taken into account is that adsorbed proteins can be in several different states of different surface sizes. This is supported by experimental evidence that adsorbed proteins undergo surface-induced conformational changes [187–189] characterized by a substantial growth of the surface contact area.

Bibliography

[1] E. Warburg, M. von Laue, A. Sommerfeld, and A. Einstein. *Zu Max Plancks sechzistem Geburtstag. Ansprachen gehalten am 26. April 1918 in der Duetschen Physikalischen Gesellschft von E. Warburg, M. von Laue, A. Sommerfeld und A. Einstein.* **C. F. Müllersch Hofbuchhandlung**, Karlsruhe, (1918).

[2] F. Jacob. **Ann. Microbiol. (Inst. Pasteur)**, **125B**:133–134, (1971).

[3] J. Monod. *Il caso e la necessità.* **Mondadori**, Milano, (2001).

[4] L. Rothfield, A. Taghbalout, and Y.-L. Shih. *Spatial control of bacterial division-site placement.* **Nature Reviews Microbiology**, **3**:959, (2005).

[5] A. Seshan and A. Amon. *Linked for life: temporal and spatial coordination of late mitotic events.* **Curr. Opin. Cell Biol.**, **16**:41–48, (2004).

[6] X. Ma, D.W. Ehrhardtdagger, and W. Margolin. *Colocalization of cell division proteins FtsZ and FtsA to cytoskeletal structures in living Escherichia coli cells by using green fluorescent protein.* **Proc. Natl. Acad. Sci. USA**, **93**:12998–13003, (1996).

[7] B. Alberts, A. Johnson, J. Lewis, M. Raff, K. Roberts, and P. Walter. *Molecular Biology of the Cell.* **Garland** , New York, 4 edition, (2002).

[8] D. Bray. *Cell Movements: From Molecules to Motility.* **Garland** , New York, 2nd edition, (2002).

[9] Z. Gitai. *The New Bacterial Cell Biology: Moving Parts and Subcellular Architecture.* **Cell**, **120**:577–586, (2005).

[10] P.L. Graumann. *Cytoskeletal elements in bacteria.* **Curr. Opin. Microbiol.**, **7**:565–571, (2004).

[11] R. Carballido-Lòpez and J. Errington. *A dynamic bacterial cytoskeleton.* **Trends Cell Biol.**, **13**:577–583, (2005).

[12] Z. Gitai. *Plasmid segregation: a new class of cytoskeletal proteins emerges.* **Curr. Biol.**, **16**:R133–136, (2006).

[13] N.A. Dye, Z. Pincus, J.A. Theriot, L. Shapiro, and Z. Gitai. *Two independent spiral structures control cell shape in Caulobacter.* **Proc. Natl. Acad. Sci. USA**, **102**:18608–18613, (2005).

[14] Z. Gitai, N. Dye, and L. Shapiro. *An actin-like gene can determine cell polarity in bacteria.* **Proc. Natl. Acad. Sci. USA**, **101**:8643–8648, (2004).

[15] Z. Gitai and L. Shapiro. *Bacterial cell division spirals into control.* **Proc. Natl. Acad. Sci. USA**, **100**:7423, (2003).

[16] L. J.F. Jones, R. Carbadillo-López, and J. Errington. *Control of Cell Shape in Bacteria: Helical, Actin-like Filaments in Bacillus subtilis.* **Cell**, **104**:913–922, (2001).

[17] N. Ausmees, J.R. Kuhn, and C. Jacobs-Wagner. *The bacterial cytoskeleton: an intermediate filament-like function in cell shape.* **Cell**, **115**:705–713, (2003).

[18] J. Moller-Jensen, J. Borch, M. Dam, R.B. Jensen, P. Roepstorff, and K. Gerdes. *Bacterial mitosis: ParM of plasmid R1 moves plasmid DNA by an actin-like insertional polymerization mechanism.* **Mol. Cell**, **12**:1477–1487, (2003).

[19] R.A. Daniel and J. Errington. *Control of cell morphogenesis in bacteria: two distinct way to make a rod-shaped cell.* **Cell**, **113**:767–776, (2003).

[20] E. Bi and J. Lutkenhaus. *FtsZ-ring structure associated with division in Escherichia coli.* **Nature**, **354**:161–164, (1991).

[21] J. Löwe and L. Amos. *Crystal structure of the bacterial cell-division protein FtsZ.* **Nature**, **391**:203–206, (1998).

[22] J. Lutkenhaus and M. Sundaramoorthy. *MinD and role of the deviant Walker A motif, dimerization and membrane binding in oscillation.* **Mol. Microbiol.**, **48**:295–303, (2003).

[23] Z. Hu and J. Lutkenhaus. *A conserved sequence at the C-terminus of MinD is required for binding to the membrane and targeting MinC to the septum.* **Mol. Microbiol.**, **47**:345–355, (2003).

[24] E.V. Koonin. *A superfamily of ATPases with diverse functions containing either classical or deviant ATP-binding motif.* **J. Mol. Biol.**, **229**:1165–1174, (1993).

[25] K.A. Michie and J. Löwe. *Dynamic filaments of the bacterial cytoskeleton*. **Annual Review of Biochemistry**, **75**:467–492, (2006).

[26] F. van den Ent, L. A. Amos, and J. Löwe. *Prokaryotic origin of the actin cytoskeleton*. **Nature**, **413**:39–44, (2001).

[27] C. Aldridge, J. Maple, and S. Moller. *The molecular biology of plastid division in higer plants*. **J. Exp. Bot.**, **56**:1061–1077, (2005).

[28] K. S. Colletti, E. A. Tattersall, K. A. Pyke, J. E. Froelich, K. D. Stokes, and K. W. Osteryoung. *A homologue of the bacterial cell division site-determining factor MinD mediates placement of the chloroplast division apparatus*. **Curr. Biol.**, **10**:507–516, (2000).

[29] M. Howard and K. Kruse. *Cellular organization by self-organization: mechanisms and model for Min protein dynamics*. **J. Cell Biol.**, **168**:533–536, (2005).

[30] A.Hunding, G.Ebersbach, and K. Gerdes. *A Mechanism for ParB-dependent Waves of ParA, a Protein Related to DNA Segregation during Cell Division in Prokaryotes*. **J. Mol. Biol.**, **329**:35, (2003).

[31] T. Mignot, J.P. Merlie, and D.R. Zusman. *Regulate Pole-to-Pole Oscillations of a Bacterial Gliding Mobility Protein*. **Science**, **310**:855–857, (2005).

[32] A. Goldbeter. *Biochemical oscillations and cellular rhythms*. **Cambridge University Press**, Cambridge, (1996).

[33] L. Glass and M. Mackey. *The rhytms of life*. **Princeton University Press**, Princeton, (1988).

[34] A. Deutsch, J. Howard, M. Falke, and W. Zimmerman Eds. *Function and regulation of cellular system*. **Birkhäuser Verlag**, Basel-Boston-Berlin, (2004).

[35] K. Kruse and F. Jülicher. *Oscillations in Cell Biology*. **Curr. Opin. Cell Biol.**, **17**:20, (2005).

[36] S. Dans, P.B. Sorensen, and F. Hynne. *Sustained oscillations in living cells*. **Nature**, **402**:320–322, (1999).

[37] A.J. Koch and H. Meinhardt. *Biological pattern formation: from basic mechanisms to complex structures*. **Rev. Mod. Phys.**, **66**:1481–1506, (1994).

[38] A.M. Turing. *The chemical basis of morphogenesis*. **Philos. Trans. R. Soc. London**, **B237**:37–72, (1952).

[39] B.O. Kuppers. *Information and origin of life*. **The MIT Press**, Cambridge, Mass., (1990).

[40] E. Mayr. *The growth of biological thought. Diversity, evolution and inheritance*. **The Belknap Press of Harvard University Press**, Cambridge, Mass., (1982).

[41] C. Bustamante, Z. Bryant, and S.B. Smith. *Ten years of tension: single-molecule DNA mechanics*. **Nature**, **421**:423–427, (2003).

[42] S. R. de Groot and P. Mazur. Non-equilibrium thermodynamics. **Dover edition**, New York, (1983).

[43] C. Bustamante, J. Liphardt, and F. Ritort. *The Nonequilibrium Thermodynamics of Small Systems* . **Physics Today**, **58**:43–48, (2005).

[44] J. Paulsson. *Summing up the noise in gene networks*. **Nature**, **427**:415–418, (2004).

[45] U. Alon. *An Introduction to System Biology: Design Principles of Biological Circuits*. **CRC Press, Taylor & Francis Group**, London, (2007).

[46] E.J. Stewart, R. Madden, G. Paul, and F. Taddei. *Aging and Death in an Organism that Reproduces by Morphologically Symmetric Division*. **PLoS Bilogy**, **3**:0295–0300, (2005).

[47] J. Lutkenhaus and S.G. Addinall. *Bacterial cell division and the Z ring*. **Annu. Rev. Biochem.**, **66**:93–116, (1997).

[48] J. Lutkenhaus. *Dynamic proteins in bacteria*. **Curr. Opin. Microbiol.**, **5**:548–552, (2002).

[49] J. Stricker, P. Maddox, E.D. Salmon, and H.P. Erickson. *Rapid assembly dynamics of the Escherichia coli FtsZ-ring demonstrated by fluorescence recovery after photobleaching*. **Proc. Natl. Acad. Sci. USA**, **99**:3171–3175, (2002).

[50] D.E. Anderson, F.J. Gueiros-Filho, and H.P. Erickson. *Assembly Dynamics of FtsZ Rings in Bacillus subtilis and Escherichia coli and Effects of FtsZ-Regulating Proteins*. **J Bacteriol.**, **186**:5775–5781, (2004).

[51] Y. Chen and H.P. Erickson. *Rapid in Vitro Assembly Dynamics and Subunit Turnover of FtsZ Demonstrated by Fluorescence Resonance Energy Transfer*. **J. Biol. Chem.**, **280**:22549–22554, (2005).

[52] X.-C. Yu and W. Margolin. *FtsZ ring clusters in min and partition mutants: role of both the Min system and the nucleoid in regulating FtsZ ring localization.* **Mol. Microbiol.**, **32**:315–326, (1999).

[53] L.J. Wu and J. Errington. *Coordination of Cell Division and Chromosome segregation by Nucleoid Occlusion Protein in Bacillus subtilis*. **Cell**, **117**:915, (2004).

[54] T.G. Bernhardt and Piet A.J. de Boer. *SlmA, a Nucleoid-Associated, FtsZ Binding Protein Required for Blocking Septal Ring Assembly over Chromosomes in E. coli*. **Mol. Cell**, **18**:555–564, (2005).

[55] S. Elmorea, M.Müllera, N. Vischera, T. Odijkb, and C.L. Woldringha. *Single-particle tracking of oriC-GFP fluorescent spots during chromosome segregation in Escherichia coli*. **J. Struct. Biol.**, **151**:275–287, (2005).

[56] S. Jun and B. Mulder. *Entropy-driven spatial organization of highly confined polymers: Lessons for the bacterial chromosome*. **Proc. Natl. Acad. Sci. USA**, **103**:12388–12393, (2006).

[57] P.A.J. de Boer, R.E. Crossley, and L.I. Rothfield. *A division inhibitor and a topological specificity factor coded for by the minicell locus determine proper placement of the division septum in E. coli*. **Cell**, **56**:641–649, (1989).

[58] E. Bi and J. Lutkenhaus. *Cell Division Inhibitors SulA and MinCD Prevent Formation of the FtsZ Ring*. **J. Bacteriol.**, **175**:1118–1125, (1993).

[59] H.I. Adler, W.D. Fisher, A. Cohen, and A.A. Hardigree. *Miniature Escherichia Coli Cells Deficient in DNA*. **Proc. Natl. Acad. Sci. USA**, **57**:321, (1967).

[60] Z. Hu, A. Mukherjee, S. Pichoff, and J. Lutkenhaus. *The MinC component of the division site selection system in Escherichia coli interacts with FtsZ to prevent polymerization*. **Proc. Natl. Acad. Sci. USA**, **96**:14819, (1999).

[61] Z. Hu and J. Lutkenhaus. *Topological regulation of cell division in Escherichia coli involves rapid pole to pole oscillation of the division inhibitor MinC under the control of MinD and MinE*. **Mol. Microbiol.**, **34**:82–90, (1999).

[62] D.M. Raskin and P.A.J. deBoer. *MinDE-Dependent Pole-to-Pole Oscillation of Division Inhibitor MinC in Escherichia coli*. **J. Bacteriol.**, **181**:6419, (1999).

[63] D.M. Raskin and P.A.J. deBoer. *Rapid pole-to-pole oscillation of a protein required for directing division to the middle of Escherichia coli*. **Proc. Natl. Acad. Sci. USA**, **96**:4971–4976, (1999).

[64] C.A. Hale, H. Meinhardt, and P.A.J. deBoer. *Dynamic localization cycle of the cell division regulator MinE in Escherichia coli*. **EMBO J.**, **20**:1563, (2001).

[65] J. Huang, C. Cao, and J. Lutkenhaus. *Interaction between FtsZ and inhibitors of cell division*. **J. Bacteriol.**, **178**:5080, (1996).

[66] Z. Hu, E.P. Gogol, and J. Lutkenhaus. *Dynamical assembly of MinD on phospholipid vescicles regulated by ATP and MinE*. **Proc. Natl. Acad. Sci. USA**, **99**:6761–6766, (2002).

[67] K. Suefuji, R. Valluzzi, and D. RayChaudhuri. *Dynamic assembly of MinD into filament bundles modulated by ATP, phospholipids, and MinE*. **Proc. Natl. Acad. Sci. USA**, **99**:16776, (2002).

[68] Y. Shih, T. Le, and L. Rothfield. *Division site in Eschrichia coli involves dynamic redistribution of Min proteins whthin coiled structures that extend between the two cell poles*. **Proc. Natl. Acad. Sci. USA**, **100**:7865–7870, (2003).

[69] H. Meinhard and P.A.J. de Boer. *Pattern formation in Escherichia coli: A model foe the pole-to-pole oscillations of Min proteins and the localization of the divison site*. **Proc. Natl. Acad. Sci. USA**, **98**:14202–14207, (2001).

[70] M. Howard, A.D. Rutenberg, and S. Vet. *Dynamic Compartmentalization of Bacteria: Accurate Division in E. coli*. **Phys. Rev. Lett.**, **87**:278102–1–4, (2001).

[71] K.C. Huang, Y. Meir, and N.S. Wingreen. *Dynamic structures in Escherichia coli: Spontaneous formation of MinE rings and polar zones*. **Proc. Natl. Acad. Sci. USA**, **100**:12724–12728, (2003).

[72] D. Drew, M. Osborn, and L. Rothfield. *A polymerization-depolymerization model that accurately generates the self-sustained oscillatory system involved in bacterial division site placement*. **Proc. Natl. Acad. Sci. USA**, **102**:6114–6118, (2005).

[73] N. Pavin, H.C. Paljetak, and V. Krstić. *Min-protein oscillations in Escherichia coli with spontaneous formation of two-stranded filaments in a three-dimensional stochastic reaction-diffusion model*. **Phys. Rev. E**, **73**:021904, (2006).

[74] F. Tostevin and M. Howard. *A stochastic model of Min oscillations in Escherichia coli and Min protein segregation during cell division*. **Phys. Biol.**, **3**:1–12, (2006).

[75] R.A. Kerr, H. Levine, T.J.Sejnowski, and W-J. Rappel. *Division accuracy in a stochastic model of Min oscillations in Escherichia coli*. **Proc. Natl. Acad. Sci. USA**, **103**:347–352, (2006).

[76] K. Kruse. *A Dynamic Model for Determining the Middle of Escherichia coli*. **Biophys. J.**, **82**:618–627, (2002).

[77] G. Meacci & K. Kruse. *Min-oscillations in Escherichia coli induced by interaction of membrane-bound proteins*. **Phys. Biol.**, **2**:89–97, (2005).

[78] A. Taghbalout, L. Ma, and L. Rothfield. *Role Of MinD-Membrane Association in Min Protein Interactions*. **J. Bacteriol.**, **188**:2993–3001, (2006).

[79] L.L. Lackner, D.M. Raskin, and P.A.J. de Boer. *ATP-Dependent Interactions between Escherichia coli Min Proteins and the Phospholipid Membrane In Vitro*. **J Bacteriol.**, **185**:735749, (2003).

[80] E. Mileykovskaya, I. Fishov, X. Fu, B.D. Corbin, W. Margolin, and W. Dowhan. *Effects of phospholipid composition on MinD-membrane interactions in vitro and in vivo*. **J. Biol. Chem.**, **1**:22193–22198, (2003).

[81] D.M. Raskin and P.A.J. deBoer. *The MinE ring: an FtsZ-independent cell structure required for selection of the correct division site in E. coli*. **Cell**, **91**:685, (1997).

[82] S.L. Rowland, X. Fu, M.A. Sayed, Y. Zhang, W.R. Cook, and L.I. Rothfield. *Membrane redistribution of the Escherichia coli MinD protein induced by MinE*. **J. Bacteriol.**, **182**:613, (2000).

[83] H.H. McAdams and A. Arkin. *Its a noisy business! Genetic regulation at the nanomolar scale*. **Trends Genet.**, **15**:65, (1999).

[84] M. Kaern, T.C. Elston, W.J. Blake, and J.J. Collins. *Stochasticity in gene expression: From theories to phenotypes*. **Nature Rev. Gen.**, **6**:451–464, (2005).

[85] J. Lippincott-Schwartz, E. Snapp, and Kenworthy A. *Studying protein dynamics in living cells*. **Nature Rev. Mol. Cell Biol.**, **2**, (2001).

[86] J. Lippincott-Schwartz, E. Snapp, and A. Kenworthy. *Studying protein dynamics in living cells*. **Nat. Rev. Mol. Cell Biol**, **2**:444456, (2001).

[87] J. Deich, E. M. Judd, H. H. McAdams, and E. Moerner. *Visualization of the movement of single histidine kinase molecules in live Caulobacter cells*. **Proc. Natl. Acad. Sci. USA**, **101**:15921–15926, (2004).

[88] M.B. Elowitz, M.G. Surette, P. Wolf, J.B. Stock, and S. Leibler. *Protein Mobility in the Cytoplasm of Escherichia coli*. **J. Bacteriol.**, **181**:197–203, (1999).

[89] O. Krichevsky and G. Bonnet. *Fluorescence correlation spectroscopy: the technique and its applications*. **Rep. Prog. Phys.**, **65**:251–297, (2002).

[90] P. Cluzel, M. Surette, and S. Liebler. *An ultrasensitive Bacterila Motor Revealed by Monitoring Signaling Proteins in Single Cells*. **Science**, **287**:1652–1655, (2000).

[91] T.T. Le, S. Harlepp, C.C. Guet, K. Dittmar, T. Emonet, T.Pan, and P. Cluzel. *Real-time RNA profiling within a single bacterium*. **Proc. Natl. Acad. Sci. USA**, **102**:9160–9164, (2005).

[92] T.T. Le, T. Emonet, S. Harlepp, C.C. Guet, and P. Cluzel. *Dynamical Determinants of Drug-Inducible Gene Expression in a Single Bacterium*. **Biophys J.**, **90**:3315–3321, (2006).

[93] P. Schwille, J. Korlach, and W.W. Webb. *Fluorescence correlation spectroscopy with single molecule sensitivity on cell and model membranes*. **Cytometry**, **36**:176182, (1999).

[94] P. Schwille, U. Haupts, S. Maiti, and W.W. Webb. *Molecular dynamics in living cells observed by fluorescence correlation spectroscopy with one- and two-photon excitation*. **Biophys. J.**, **77**:2251–2265, (1999).

[95] M. Weiss, H. Hashimoto, and T. Nilsson. *Anomalous Protein Diffusion in Living Cells as Seen by Fluorescence Correlation Spectroscopy*. **Biophys. J.**, **84**:4043–4052, (2003).

[96] M. Weiss, M. Elsner, F. Kartberg, and T.Nilsson. *Anomalous Subdiffusion Is a Measure for Cytoplasmic Crowding in Living Cells*. **Biophys J.**, **87**:3518–3524, (2004).

[97] D.S. Banks and C. Fradin. *Anomalous Diffusion of Proteins Due to Molecular Crowding*. **Biophys J.**, **89**:2960–2971, (2005).

[98] K. Jacobson, A. Ishihara, and R. Inman. *Lateral diffusion of proteins in membrane*. **Annu. Rev. Physiol.**, **49**:163175, (1987).

[99] P. Almeida and W. Vaz. *Lateral diffusion in membranes. In Handbook of Biological Physics. R. Lipowsky and E. Sackmann, editors.* **Elsevier**, New York, 1995.

[100] T.J. Feder, I. Brust-Mascher, J.P. Slattery, B. Baird, and W.W. Webb. *Constrained diffusion or immobile fraction on cell surfaces: a new interpretation.* **Biophys. J.**, **70**:27672773, (1996).

[101] E. Limpert, W.A. Stahel, and M. Abbt. *Log-normal Distributions across the Sciences: Keys and Clues.* **BioScience**, **51**:341–352, (2001).

[102] C.W. Mullineaux, A. Nenninger, N. Ray, and C. Robinson. *Diffusion of Green Fluorescent Protein in Three Cell Environments in Escherichia Coli.* **J. Bacteriol.**, **188**:3442–3448, (2006).

[103] M. Howard. *A Mechanism for Polar Protein Localization in Bacteria.* **J. Mol. Biol.**, **335**:655–663, (2004).

[104] K.C. Huang and N. Wingreen. *Min-protein oscillation in round bacteria.* **Phys. Biol.**, **1**:229, (2004).

[105] G. F. King. *The dimerization and topological specificity functions of MinE reside in a structurally autonomous C-terminal domain.* **Mol. Microbiol.**, **31**:1161, (1999).

[106] A. Desai, S. Verma, T.J. Mitchison, and C.E. Walczak. *Kin I kinesins are microtubule-destabilizing enzymes.* **Cell**, **96**:69–78, (1999).

[107] A.W. Hunter, M. Caplow, D.L. Coy, W.O. Hancock, S. Diez, L. Wordeman, and J. Howard J. *The kinesin-related protein MCAK is a microtubule depolymerase that forms an ATP-hydrolyzing complex at microtubule ends.* **Mol. Cell**, **11**:445, (2003).

[108] G. A. Klein, K. Kruse, G. Cuniberti, and F. Jülicher. *Filament Depolymerization by Motor Molecules.* **Phys. Rev. Lett.**, **94**:108102, (2005).

[109] C. Zhao, P.A.J. de Boer, and L.I. Rothfield. *Proper Placement of the Escherichia coli Division Site Requires Two Functions that are Associated with Different Domains of the MinE Protein.* **Proc. Natl. Acad. Sci. USA**, **92**:4313–4317, (1995).

[110] Y-L. Shih, X. Fu, G.F. King, T. Le, and L. Rothfield. *Division site placement in E.coli: mutations that prevent formation of the MinE ring lead to loss of the normal midcell arrest of growth of polar MinD membrane domains.* **EMBO J.**, **21**:33473357, (2002).

[111] W. Bialek. in *Advances in Neural Information Processing 13*. **MIT press**, Cambridge, (2001).

[112] D.A. Kessler and H. Levine. *Fluctuation-induced diffusive instabilities*. **Nature**, **394**:556, (1998).

[113] M. Falcke, L. Tsimring, and H. Levine. *Stochastic spreading of intracellular Ca2+ release*. **Phys. Rev. E**, **62**:26362643, (2000).

[114] J.M.G. Vilar and J.M. Rubí. *Spatiotemporal Stochastic Resonance in the Swift-Hohenberg Equation*. **Phys. Rev. Lett.**, **78**:28862889, (1997).

[115] J.M.G. Vilar and J.M. Rubí. *Ordering periodic spatial structures by non-equilibrium fluctuations*. **Physica A**, **277**:327–334, (2000).

[116] J. García-Ojalvo and J.M. Sancho. *Noise in Spatially Extended Systems*. **Springer-Verlag**, New York, (1999).

[117] J. Paulsson, G. Otto, and M. Ehrenberg. *Stochastic focusing: Fluctuation-enhanced sensitivity of intracellular regulation*. **Proc. Natl. Acad. Sci. USA**, **97**:7148–7153, (2000).

[118] J.M.G. Vilar, H.Y. Kueh, N. Barkai, and S. Leibler. *Mechanisms of noise-resistance in genetic oscillators*. **Proc. Natl. Acad. Sci. USA**, **99**:5988–5992, (2002).

[119] H. Qian, S. Saffarian, and L. Elson. *Concentration fluactuations in a mesoscopic oscillating chemical reaction system*. **Proc. Natl. Acad. Sci. USA**, **99**:10376–10381, (2002).

[120] M. Howard and A. D. Rutenberg. *Pattern Formation inside Bacteria: Fluctuations due to the Low Copy Number of Proteins*. **Phys. Rev. Lett.**, **90**:128102, (2003).

[121] R. Kulkarni, K. C. Huang, M. Kloster, and N. S. Wingreen. *Pattern Formation within Escherichia coli: Diffusion, Membrane Attachment, and Self-Interaction of MinD Molecules*. **Phys. Rev. Lett.**, **93**:228103, (2004).

[122] D. Fange and J. Elf. *Noise-Induced Min Phenotypes in E. coli*. **PLoS**, **2**:0637–0648, (2006).

[123] K. Doubrovinski and M. Howard. *Stochastic model for Soj relocation dynamics in Bacillus subtilis*. **Proc. Natl. Acad. Sci. USA**, **102**:9808–9813, (2005).

[124] J.R. Stiles and T.M. Bartol. in *Computational Neurobiology: Realistic Modelling for Experimentalists,* ed. E. de Schutter. **CRC Press**, Boca Raton, FL, (2001).

[125] R.F. Fox and J. Keizer. *Amplification of intrinsic fluactuations by chaotic dynamics in physical systems* . **Phys. Rev. E**, **43**:1709–1720, (1991).

[126] N.G. van Kampen. *Stochastic Processes in Physics and Chemistry*. **North-Holland**, Amsterdam, (1981, 1992).

[127] A.B. Bortz, M. Kalos, and J.L. Lebowitz. *A new algorithm for Monte Carlo simulation of Ising spin systems*. **J. Comput. Phys.**, **17**:10–18, (1975).

[128] D.T. Gillespie. *Exact Stochastic Simulation of Coupled Chemical Reactions*. **J. Phys. Chem.**, **81**:2340–2361, (1977).

[129] G. Giacomin and J.L. Lebowitz. *Exact Macroscopic Description of Phase Segregation in Model Alloy with Long Range Interactions*. **Phys. Rev. Lett.**, **76**:1094, (1996).

[130] A.S. Mikhailov. *Selected Topics in Fluctuational Kinetic of Reactions*. **Phys. Rep.**, **184**:307, (1989).

[131] M. Bertram, C. Beta, M. Pollman, A.S. Mikhailov, H.H. Rotermund, and G. Ertl. *Pattern formation on the edge of chaos: Experiments with Co oxidation on a Pt(110) surface under global delayed feedback*. **Phys. Rev. E**, **67**:036208, (2003).

[132] M. Hildebrand and A.S. Mikhailov. *Mesoscopic Modeling in the Kinetic Theory of Adsorbates*. **J. Phys. Chem.**, **100**:19089, (1996).

[133] A. Mikhailov and G. Ertl. *Pattern formation by adsorbates with attractive lateral interactions*. **Chem. Phys. Lett.**, **238**:104, (1996).

[134] D. Battogtokh, M. Hildebrand, K. Krischer, and A.S. Mikhailov. *Nucleation kinetic and global coupling in reaction-diffusion systems*. **Phys. Rep.**, **288**:435, (1997).

[135] M. Hildebrand, A.S. Mikhailov, and G. Ertl. *Nonequilibrium stationary microstructures in surface chemical reactions*. **Phys. Rev. E**, **58**:5483, (1998).

[136] M. Hildebrand A.S. Mikhailov and G. Ertl. *Traveling Nanoscale Structures in Reactive Adsorbates with Attractive Lateral Interactions*. **Phys. Rev. Lett.**, **81**:2602, (1998).

[137] M. Hildebrand A.S. Mikhailov. *Nanoscale Wave Patterns in Reactive Adsorbates with Attractive Lateral Interactions*. **J. Stat. Phys.**, **101**:599, (2000).

[138] C. Sachs, M. Hildebrand, S. Völkening, and J. Wintterlin G. Ertl. *Spatiotemporal Sel-Organization in a Surface Reaction: From the Atomic to the Mesoscopic Scale*. **Science**, **293**:1635, (2001).

[139] M. Hildebrand. *Self-organized nanostructures in surface chemical reactions: Mechanisms and mesoscopic modeling*. **Chaos**, **12**:144, (2002).

[140] C. Sachs, M. Hildebrand, S. Völkening, J. Wintterlin, and G. Ertl. *Reaction fronts in the oxidation of hydrogen on Pt(111): Scanning tunneling microscopy experiments and reaction-diffusion modeling*. **J. Chem. Phys.**, **116**:5759, (2002).

[141] R. Reigada, F.Sagués, and A.S. Mikhailov. *Traveling Wave and Nonequilibrium Stationary Patterns in Two-Component Reactive Langmuir Monolayer*. **Phys. Rev. Lett.**, **89**:038301, (2002).

[142] R. Friedrich, J. Peinke, and Ch. Renner. *How to Quantify Deterministic and Random Influences on the Statistics of the Foreign Exchange Market*. **Phys. Rev. Lett.**, **84**:5224, (2000).

[143] R. Friedrich and J. Peinke. *Description of a Turbulent Cascade by a Fokker-Planck Equation*. **Phys. Rev. Lett.**, **78**:863, (1997).

[144] M.B. Elowitz, A.J. Levine, E.D. Siggia, and P.P. Swain. *Stochastic Gene Expression in a Single Cell*. **Science**, **297**:1183–1186, (2002).

[145] E.M. Ozbudak, M. Thattai, I. Kurtser, A.D. Grossman, and A. van Oudenaarden. *Regulation of noise in the expression of a single gene*. **Nature Genet.**, **31**:69–73, (2002).

[146] W.J. Blake, M.Kaern, C.R. Cantor, and J.J. Collins. *Noise in eukaryotic gene expression*. **Nature**, **422**:633–637, (2003).

[147] J.M. Raser and E.K. O'Shea. *Control of Stochasticity in Eukaryotic Gene Expression*. **Science**, **304**:1811–1814, (2004).

[148] D.K.C. MacDonald. . **Phil. Mag.**, **45**:63 and 345, (1954).

[149] D.K.C. MacDonald. *Brownian Movement*. **Phys. Rev.**, **108**:541, (1957).

[150] N.G. van Kampen. *A New Approach to Noise in Quantum Mechanics*. **J. Stat. Phys.**, **115**:1057, (2004).

[151] M. San Miguel and R. Toral. *Stochastic Effects in Physical Systems. Instabilities and Nonequilibrium Structures VI,* E. Tirapegui and J. Martínez and R. Tiemann editors. **Kluwer Academic**, (2000).

[152] G.W. Gardiner. *Handbook of Stochastic Methods*. **Springer**, Berlin, Heidelberg, (1985).

[153] W. Paul and J. Baschnagel. *Stochastic Processes. From Physics to Finance*. **Springer-Verlag**, Berlin, Heidelberg, (1999).

[154] L. Arnold. *Stochastic Differential Equations: Theory and Applications*. **Krieger**, Malabar, Florida, (1992).

[155] O. Carrillo, M. Ibañes, J. García-Ojalvo, J. Casademunt, and L.M. Sancho. *Intrinsic noise-induced phase tranitions: Beyond the noise interpretation*. **Phys. Rev. E**, **67**:046110, (2003).

[156] I. Dornic, H. Chaté, and M.A. Muñoz. *Integration of Langevin Equations with Multiplicative Noise and the Viability of Field Theories for Absorbing Phase Transitions*. **Phys. Rev. Lett.**, **94**:100601, (2005).

[157] E. Moro. *Numerical schemes for continuum models of reaction-diffusion systems subject to internal noise*. **Phys. Rev. E**, **70**:045102, (2004).

[158] L. Pechenik and H. Levine. *Interfacial velocity corrections due to multiplicative noise*. **Phys. Rev. E**, **59**:3893, (1999).

[159] A.S. Mikhailov. *Foundations of Synergetic II. Chaos and Noise*. **Springer**, Berlin, Heidelberg, (1996).

[160] A.D. Fokker. *Die mittlere Energie rotierender elektrischer Dipole im Strahlungsfeld*. **Ann. Physik**, **43**:810, (1914).

[161] M. Planck. *Über einen satz der statistischen Dynamik and seine Erweiterung in der Quantetheorie*. **Sitzber. Preuss. Akad. Wiss.**, **45**:324, (1917).

[162] R. Brent. *Genomic biology*. **Cell**, **100**:169–183, (2000).

[163] J. Wu and D. Pollard. *Counting Cytokinesis Proteins Globally and Locally in Fission Yeast*. **Science**, **310**:310–314, (2005).

[164] N. Rosenfeld, T.J. Perkins, U. Alon M.B. Elowitz, and P.S. Swain. *A Fluctuation Method to Quantify In Vivo Fluorescence Data*. **Biophys J.**, **91**:759–766, (2006).

[165] V. Noireaux, R. Bar-Ziv, J. Godefroy, H. Salman, and A. Libchaber. *Toward an artificial cell based on gene expression in vesicles*. **Phys. Biol.**, **2**:P1–P8, (2005).

[166] B.P. Cormack, R.H. Valdivia, and S. Falkow. *FACS-optimized mutants of the green fluorescent protein (GFP)*. **Gene**, **173**:33–38, (1996).

[167] B.D. Corbin, X-C. Yu, and W. Margolin. *Exploring intracellular space: function of the Min system in round-shaped Escherichia coli*. **EMBO J.**, **21**:1998–2008, (2002).

[168] S. Thanedar and W. Margolin. *FtsZ Exibiths Rapid Movement and Oscillation Waves in Helix-like Patterns in Escherichia coli*. **Curr. Biol.**, **14**:1167–1173, (2004).

[169] S. Pichoff, B. Vollrath, C. Touriol, and J.-P. Bouché. *Deletion analysis of gene minE which encodes the topological specificity factor of cell division in Escherichia coli*. **Mol. Microbiol.**, **18**:321, (1995).

[170] A. Gennerich and D. Schild. *Fluorescence Correlation Spectroscopy in Small Cytosolic Compartments Depends Critically on the Diffusion Model Used*. **Biophys J.**, **79**:3294–3306, (2000).

[171] E.L. Elson and D. Magde. *Fluorescence correlation spectroscopy. I. Conceptual basis and theory*. **Biopolymers**, **13**:1–27, (1974).

[172] E. Padan, D. Zilberstein, and H. Rottenberg. *The proton electrochemical gradient in Escherichia coli cells*. **Eur. J. Biochem.**, **63**:533–541, (1976).

[173] U. Haupts, S. Maiti, P. Schwille, and W.W. Webb. *Dynamics of fluorescence fluctuations in green fluorescent protein observed by fluorescence correlation spectroscopy*. **Proc. Natl. Acad. Sci. USA**, **95**:13573–13578, (1998).

[174] J. Nelson, B. Trina, A. Kristien, J. Zaal, and J. Lippincott-Schwartz. *ER-to-Golgi transport visualized in living cells*. **Nature**, **389**:81–85, (1997).

[175] D.E. Wolf. *Design, building and use of a flourescence recovery after photobleaching instrument; in "Fluorescence Microscopy of Living Cells in Culture", Part B. Quantitative Fluorescence Microscopy: Imaging and Spectroscopy, Vol. 30*. **Academic Press**, San Diego, (1989).

[176] D. Magde, E. Elson, and W.W. Webb. *Fluorescence correlation spectroscopy. II. Experimental realization.* **Biopolymers**, **13**:29–61, (1974).

[177] P. Schwille. *Fluorescence Correlation Spectroscopy and Its Potential for Intracellular Applications.* **Cell Biochem. Biophys.**, **34**:383–408, (2001).

[178] P. Schwille and E. Haustein. *Fluorescence Correlation Spectroscopy.* Biophysics Textbook Online; **http://www.biophysics.org/education/techniques.htm**.

[179] J.R. Lakowicz. *Principles of Fluorescence Spectroscopy.* **Springer-Verlag**, New York, (2006).

[180] D. Madge, E. Elson, and W. W. Webb. *Thermodynamic Fluctuations in a Reacting SystemMeasurement by Fluorescence Correlation Spectroscopy.* **Phys. Rev. Lett.**, **29**:705–708, (1972).

[181] R. Rigler, Ü. Mets, J. Widengreen, and P. Kask. *Fluorescence correlation spectroscopy with high count rate and low background: analysis of translational diffusion.* **Eur. J. Biophys.**, **22**:169–75, (1993).

[182] A. Torcini, H. Frauenkron, and P. Grassberger. *A Novel Integration Scheme for Partial Differential Equations: an Application to the Complex Ginzburg-Landau Equation.* **Physica D**, **103**:605, (1997).

[183] M. Hildebrand. *Selbstorganisierte Nanostrukturen in katalytischen Oberflächenreaktionen.* **Dissertation**, Humboldt-Universität, Berlin, (1999).

[184] H. Risken. *The Fokker-Planck Equation.* **Springer**, Berlin, Heidelberg, (1989).

[185] D.G. Vlachos and M.A. Katsoulakis. *Derivation and validation of Mesoscopic Theories for Diffusing of Interacting Molecules.* **Phys. Rev. Lett.**, **85**:3898, (2000).

[186] I. Hayashi, T. Oyama, and K. Morikava. *Structural and functional studies of MinD ATPase: implications for the molecular recognition of the bacterial cell division apparatus.* **EMBO J.**, **20**:1819, (2001).

[187] W. Norde. *Adsorption of Proteins at Solid-Liquid Interfaces.* **Cell and Material**, **5**:97–112, (1995).

[188] J. Bujis, W. Norde, and J.W.T.Lichtenbelt. *Changes in the Secondary Structure of Adsorbed IgG and F(ab')$_2$ Studied by FTIR Spectroscopy.* **Langumir**, **12**:1605–1613, (1996).

[189] C.F. Wertz and M.M. Santore. *Adsorption and Relaxation Kinetics of Albumin and Fibrinogen on Hydrophobic Surfaces: Single-Species and Competitive Behavior*. **Langumir**, **15**:8884–8894, (1999).

[190] A. Finkelstein. *Protein Physics*. **Academic Press**, New York, (2002).

Erklärung

Hiermit versichere ich, dass ich die vorliegende Arbeit ohne unzulässige Hilfe Dritter und ohne Benutzung anderer als der angegebenen Hilfsmittel angefertigt habe; die aus fremden Quellen direkt oder indirekt übernommenen Gedanken sind als solche kenntlich gemacht. Die Arbeit wurde bisher weder im Inland noch im Ausland in gleicher oder ähnlicher Form einer anderen Prüfungsbehörde vorgelegt. Die vorliegende Dissertation wurde am Max-Planck-Institut für Physik komplexer Systeme in Dresden unter der wissenschaftlichen Betreuung von Prof. Dr. Karsten Kruse angefertigt. Es haben keine früheren erfolglosen Promotionsverfahren von mir stattgefunden. Hiermit erkenne ich die Promotionsordnung der Mathematik-Naturwissenschaften Fakultät der TU Dresden an.